T2R2 東京科学大学 リサーチリポジトリ
Science Tokyo Research Repository

# 論文 / 著書情報
# Article / Book Information

| | |
|---|---|
| 題目(和文) | |
| Title(English) | Extracorporeal Centrifugal Blood Pump Employing a Bearingless Slice Motor with a PM-free Rotor |
| 著者(和文) | YangRen |
| Author(English) | Ren Yang |
| 出典(和文) | 学位:博士(工学),<br>学位授与機関:東京工業大学,<br>報告番号:甲第12685号,<br>授与年月日:2024年3月26日,<br>学位の種別:課程博士,<br>審査員:進士 忠彦,吉田 和弘,西迫 貴志,菅原 雄介,土方 亘 |
| Citation(English) | Degree:Doctor (Engineering),<br>Conferring organization: Tokyo Institute of Technology,<br>Report number:甲第12685号,<br>Conferred date:2024/3/26,<br>Degree Type:Course doctor,<br>Examiner:,,,, |
| 学位種別(和文) | 博士論文 |
| Type(English) | Doctoral Thesis |

Powered by T2R2 (Science Tokyo Research Repository)

# Extracorporeal Centrifugal Blood Pump Employing a Bearingless Slice Motor with a PM-free Rotor

Supervised by

Professor Tadahiko SHINSHI

Department of Mechanical Engineering

Tokyo Institute of Technology

Ren YANG

January 2024

## Table of Contents

# Chapter 1 Introduction

## 1.1 Blood circulatory system

### 1.1.1 Heart disease

Deaths from heart disease are increasing globally. According to the cause of death report from Our World in Data (OWID) [1], heart disease emerged as the primary cause of death, claiming 18.5 million lives in 2019, up from 17.1 million in 2015. In Japan, heart disease ranked as the second leading cause of death in 2022, resulting in 232,964 deaths, constituting 14.8% of total deaths, as reported by the Ministry of Health, Labour and Welfare [2]. Coronary artery disease leads to the accumulation of plaque in coronary arteries, potentially culminating in a heart attack. During a heart attack, the heart muscle can sustain damage, setting the stage for heart failure. Heart failure ultimately causes the heart to lack sufficient blood flow to support circulation throughout the human body.

### 1.1.2 Treatment of heart failure

Heart failure treatment encompasses pharmaceutical and surgical treatment to assist the circulatory system. Surgical treatment includes heart valve surgery, coronary angioplasty, and stent, heart implantation, and treatment with circulatory machines.

Pharmaceutical treatment [3-5], often considered the primary approach in managing heart conditions, involves using medications such as angiotensin-converting enzyme (ACE) inhibitors and beta-blockers to enhance cardiac function and alleviate symptoms associated with heart failure. The circulatory machines for surgical treatment have four primary types: Intra-Aortic Balloon Pump (IABP), Extracorporeal Membrane Oxygenation (ECMO), Total Artificial Heart (TAH), and Ventricular Assist Device (VAD). IABP involves inserting a balloon into the aorta, which can enhance coronary blood flow and reduce the workload on the heart by controlling its construction. Typically employed in emergencies, such as heart attacks, IABP [6-7] is mainly for temporary support and cannot perform the blood pumping function on its own. ECMO [8-9] is a comprehensive system that supports blood pumping and oxygen exchange outside the body. It serves to assist both the cardiac and cardiopulmonary systems. ECMO is commonly used in heart or respiratory failure cases and has been widely used in treating COVID-19. TAH [10-11] is a device implanted in the chest to replace damaged ventricles and valves in end-stage treatment, which is typically used for patients with

concurrent biventricular dysfunction or several other structural abnormalities in ventricular and valves.

VAD functions as an auxiliary artificial heart, which utilizes a blood pump to facilitate blood circulation and alleviate cardiac strain. VADs are categorized into implantable and extracorporeal types based on the placement of the blood pump. The implantable VADs are primarily utilized for end-stage heart failure when heart transplantation is unattainable, which can serve as a form of Destination Therapy (DT) [12-13]. This long-term implantation over several years necessitates a compact design with enhanced durability, employing materials like biocompatible titanium alloy [14-15]. On the other hand, extracorporeal VADs demonstrate a broader range of applications, catering to diverse clinical scenarios and diseases.

### 1.1.3 Extracorporeal VAD

Extracorporeal VAD can be categorized into left ventricular assist device (LVAD), right ventricular assist (RVAD), and biventricular assist device (BiVAD) based on the different ventricles they support. The extracorporeal LVAD, as illustrated in Fig. 1.1, entails connecting an outflow cannula to the aorta and linking it to the outlet of the blood pump. Following this, the inflow cannula is connected from the left ventricle or left atrium to the inlet of the blood pump. The blood pump is positioned externally to the human body.

The blood pump in extracorporeal VAD, not requiring implantation with the human body, opens up a broad spectrum of application scenarios and extends beyond the end-stage heart failure. Figure 1.2 shows the timelines of the extracorporeal VAD applications. In terms of short-term application, it serves as an immediate treatment within a few hours, finding utility in ambulances for emergencies and providing mechanical circulation support during surgeries. In the medium term, over a few days, it offers auxiliary rehabilitation as the heart recuperates post-surgery and alleviates the cardiac load. Moreover, medical professionals must diagnose and determine the appropriateness of implanting the heart in the body. The two usages are termed “Bridge to Recovery” (BTR) [16-17] and “Bridge to Decision” (BTD) [18-19], respectively. Over a few months, in long-term use, especially for patients with advanced heart failure, heart transplantation emerges as the sole treatment. The application of an extracorporeal VAD while awaiting heart transplantation is referred to as a “Bridge to Transplantation” (BTT) [20-21]. Given the scarcity of donors in Japan compared to other countries, the possibility of going overseas for heart transplantation has been limited since the Istanbul Declaration in 2008 [22-23]. The organ transplant law underwent reform in July 2010 in Japan [24]. Post-reform,

even in cases where one's donation intention is unknown, obtaining the consent of one's family is sufficient for donation. Despite the increases in heart donations following the reform, evidenced by 79 heart transplants in 2022, the waiting list still encompasses 867 patients in Japan as of the current year [25]. Transitioning from extracorporeal VAD to implantable VAD is essential to enhance durability and improve the quality of life (QOL). This approach is known as "Bridge to Bridge"(BTB) [26-27].

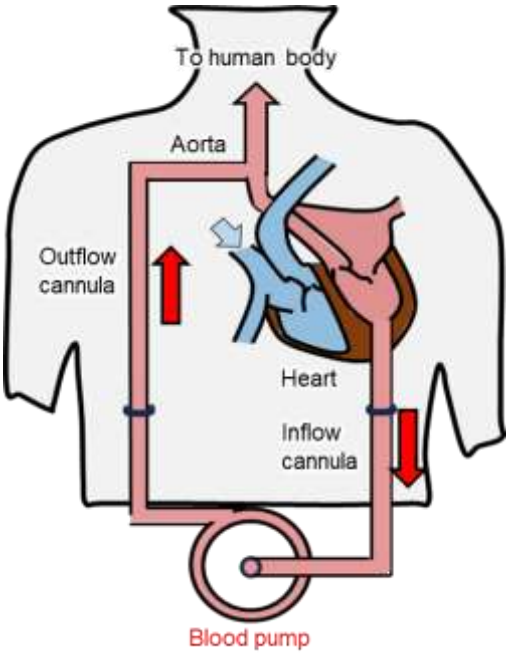


Figure 1.1 Schematic diagram of extracorporeal LVAD.

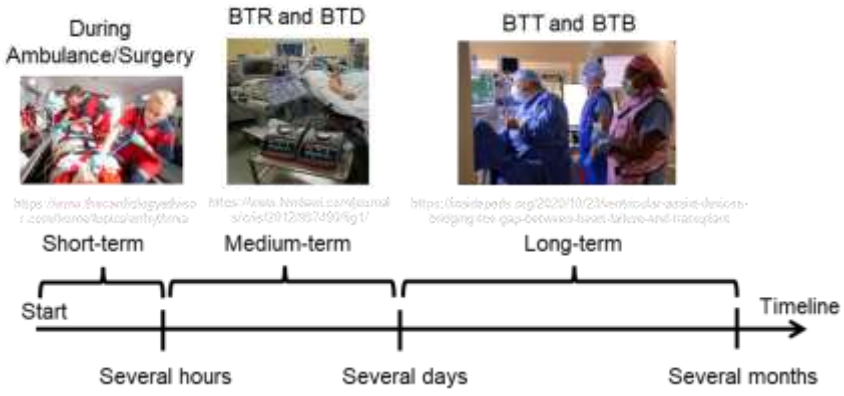


Figure 1.2 Timelines of extracorporeal VAD application.

### 1.1.4 Requirements of blood pump for extracorporeal circulation support

To fulfill the requirements of diverse treatment scenarios, the specific requirements for blood pumps for extracorporeal circulatory support are listed below:

(1) High durability (several months):

Durability [28-29] is the foremost requirement for a blood pump in extracorporeal circulation support. Unlike blood pumps used for short-term applications such as intraoperative assistance, blood pumps that meet the specifications of BTB and BTT scenarios need to be durable and highly biocompatible to function reliably over the long term. The blood pump is composed of moving mechanical parts. To enhance durability and reliability, it is necessary to prevent mechanical failures of mechanical parts during long-term operation, such as wear of valves or contact bearings, thereby avoiding medical accidents.

(2) High biocompatibility:

Biocompatibility ensures that a medical device interacts harmoniously with biological systems and minimizes adverse effects. This study addresses compatibility regarding hemolysis and thrombosis.

Hemolysis [30-31] involves rupturing or destroying red blood cells, releasing hemoglobin into the surrounding plasma. Mechanical stress within the blood pump, caused by turbulence and contact support, can induce red blood cell destruction, reducing oxygen-carrying capacity and leading to hemolytic anemia. Moreover, free hemoglobin can result in various complications, including inflammatory issues.

Thrombosis [32-33] refers to the formation of blood clots within blood vessels, occurring between procoagulant (clot-promoting) and anticoagulant (clot-inhibiting) factors that are disrupted. Materials and surface properties in blood pumps can activate procoagulant factors, while narrow spaces within the pump, prone to stagnation or recirculation, can foster clot formation.

Loose thrombosis may enter the bloodstream, causing stroke or pulmonary embolism. The typical preventive measure against blood clots involves anticoagulant use, whose dosage, however, is challenging to control [34-35]. Using little anticoagulant is ineffective, while utilizing excessive amounts may lead to internal and uncontrollable bleeding or side effects like thrombocytopenia.

(3) Compactness

Firstly, the overall size of the blood pump system must be reduced to facilitate its application in various clinical settings and to optimize patient mobility during support. Furthermore, a small initial priming volume of the pump head is necessary [36-38], which provides advantages for patient use: 1) it reduces the contact area between the pump housing and the blood, thereby reducing the risk of thrombosis; 2) it avoids overuse of donor blood or blood products to minimize risks during and after transfusion. Using too much donor blood

increases the risk of infection; conversely, using blood products mixed with saline and glucose as prefill fluids can cause complications related to hemodilution. This is particularly crucial in pediatric patients because they are susceptible to blood volume and composition changes. To ensure safety, the initial priming volume of the pump head needs to be reduced.

(4) Low disposable cost

Extracorporeal blood pumps have two components: the reusable part and the disposable pump head. The reusable part consists of the actuator and sensors, while the disposable pump head, filled with blood, needs replacement after each patient use. The aim is to minimize the costs, thereby reducing the financial burden on patients and lowering overall medical expenses [39-40].

## 1.2 Disposable extracorporeal blood pump

Different blood pump types and support methods have led to the classification of VAD into three distinct generations [41-43]. The first-generation VAD, introduced in Section 1.2.1, is referred to as a positive displacement pump. It emulates the natural beating of the Heart, generating pulsatile flow through pump action. The second-generation VAD, detained in Section 1.2.2, adopts a rotary pump with contact bearings. Unlike its predecessor, this generation produces continuous flow. The third-generation VAD also employs a rotary pump with non-contact bearings, elaborated in Section 1.2.3.

### 1.2.1 Positive displacement blood pump

One of the earliest cardiac assist devices utilizing the positive displacement pump is IABP, innovated by Moulopoulos et al. in 1962 [44]. In the 1960s, Dr. Michael Debakey's group endeavored to create a device for more extended extracorporeal circulation assistance, evolving into the LVAD. In 1966, a paracorporeal VAD design [45] partially implanted in the human body was invented, with the pump inside the patient's chest and a driving device outside. However, economic viability hampered its clinical adoption. Demand for positive displacement pumps surged in the early 1980s, as improved immunosuppressants led to more heart transplant surgeries. By the late 1980s, the first-generation commercial LVADs, exemplified by ZEON VAD [46] (ZEON Co. Ltd, Tokyo, Japan) and NIPRO-VAD [47] (Nipro Corp., Osaka, Japan), gained clinical use in Japan. Table 1.1 lists some first-generation extracorporeal VADs [46-51].

Fig. 1.3 (a) depicts ZEON VAPD, Japan's earliest in vitro extracorporeal VADs. Fig. 1.3 (b) illustrates its basic principle: the chamber is divided into an air and a blood compartment.

Regulating air pressure generates an external force, inducing reciprocal movement of the diaphragm. This process facilitates the periodic filling and emptying of the chamber containing the blood, resulting in a pulsatile flow. Simultaneously, it is essential to position two one-way valves at the inlet and outlet to ensure the flow direction.

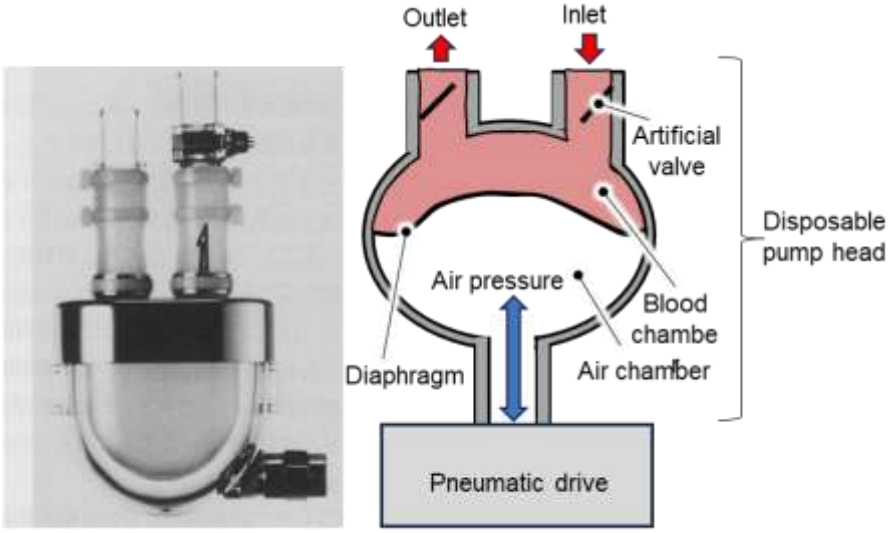


Figure 1.3 Positive displacement blood pump: (a) Photograph of the ZEON VAD (ZEON Co.Ltd Tokyo, Japan); (b) Basic principle of a pulsatile pump in positive displacement pump.

Compared to the subsequent two generations, the first-generation VAD operates as a pulsatile pump, closely mimicking the behavior of a natural ventricle. Clinical experiments have revealed its potential to reduce complications such as aortic valve issues [52-53] and gastrointestinal bleeding [54]. However, the large pump heads and drivelines increase the risk of bleeding and infection due to the large blood contact area and bacteria easily entering the wound through the driveline [55]. The substantial drive console, particularly in pneumatic systems, can impact the patient's QOL. Additionally, the positive displacement pump's reliance on numerous moving mechanical components and valves may compromise reliability and durability [56-57], making it prone to thrombosis and noise.

Table 1.1 Lists of some first-generation extracorporeal VADs

| Device | Manufacture | Drive | Dimensions |
|---|---|---|---|
| Thoratec PVAD [48] | Thoratec Crop., Pleasanton, USA | Pneumatic | 65 mL |
| Abiomed BVS5000 [49] | Abiomed Inc., Danvers, USA | Pneumatic | 80 mL |
| Berlin Heart EXCOR [50] | Berlin heart, Berlin, Germany | Pneumatic | 50-80 mL |
| NIPRO-VAD [47] | Nipro Corp., Osaka, Japan | Pneumatic | 20-60 mL |
| Novacor LVAS [51] | WorldHeart, California, USA | Electric | 25-70 mL |
| ZEON VAD [46] | ZEON Co. Ltd Tokyo, Japan | Pneumatic | 40-60 mL |

### 1.2.2 Centrifugal blood pump with contact bearing

Second-generation VAD utilizes rotary pumps. According to different working principles, second-generation VAD can be primarily categorized into centrifugal and axial flow pumps. The clinically used extracorporeal VADs employ centrifugal pumps because a large-diameter impeller/rotor enables high flow rates and high output pressures at low rotational speed.

The first VAD classified as second generation was Biomedicus Bio-pump (Medtronic Inc., Minnesota, USA), utilized since the 1980s [58]. In 1999, another widely used extracorporeal VAD -Rotaflow (Maquet, Hirrlingen, Germany) [59], gained approval in Europe for ventricular and pulmonary support. Table 1.2 lists some second-generation extracorporeal VADs [58-60].

Figure 1.4 (a) displays a photograph of Rotaflow, and Fig. 1.4 (b) typically illustrates the basic principle of a centrifugal blood pump with contact bearings. The blood is aspirated through the inlet cannula and tubing, entering the pump chamber axially. The impeller directs the fluid radially and circumferentially, and the fluid exits the pump housing through the tangential outlet. The impeller incorporates magnetic material and can function as a component of a magnetically coupled system. The position of the impeller is supported with contact bearings.

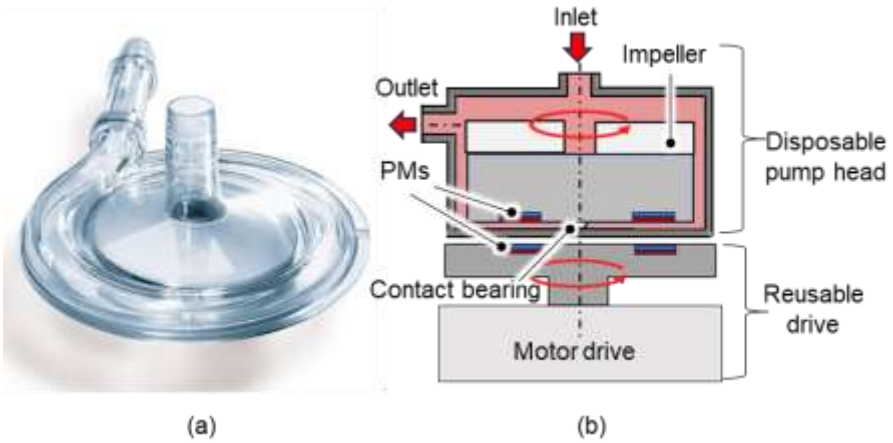


Figure 1.4 Centrifugal blood pump with contact bearings: (a) Photograph of the Rotaflow (Maquet, Hirrlingen, Germany); (b) Basic principle of a centrifugal blood pump with contact bearings.

Compared with the first-generation VAD, the second-generation type is characterized by a compact structure. The elimination of valves and other mechanical components not only diminishes noise but also augments equipment durability. Nevertheless, contact bearings increase the likelihood of thrombus deposition near the bearing. Simultaneously, mechanical wear resulting from friction may still pose durability challenges. Furthermore, the shear stress and heat generated at the contact parts can lead to significant hemolysis problems [61-63]. The disposable cost is also not very affordable, typically tens of thousands of yen each.

Table 1.2 Lists of some second-generation extracorporeal VADs

| Device | Manufacture | Contact bearing | Priming volume |
|---|---|---|---|
| BPX-80 Bio-pump [58] | Medtronic Inc., Minnesota, USA | Ball bearing | 86 mL |
| Rotaflow [59] | Maquet, Hirrlingen, Germany | Single contact pinheaded sapphire bearing | 32 mL |
| MERA HCF-MP23 [60] | Senki Medical Instrument Manufacturing Co. Ltd., Tokyo, Japan | Single pivot bearing | 22 mL |

### 1.2.3 Centrifugal pump with non-contact bearing

Compared with the second-generation VAD, the primary distinction of the third-generation VADs lies in the complete noncontact suspension of the impeller/rotor, eliminating mechanical contact between the rotating and stationary parts during operation. The primary levitation technologies involve hydrodynamic bearings [64-65], magnetic bearings [66-67], or a combination of both [68-69]. The lift force generated by the hydrodynamic bearing is

inversely proportional to the square of the air gap and directly proportional to the rotational speed. The hydrodynamic bearing needs a large circumferential speed of the rotor and maintains a small fluid gap to generate sufficient non-contact suspension force. Commercial Centrifugal blood pumps (CBPs) use full magnetic levitation to obtain a wide fluid gap and achieve non-contact rotation from low to high-speed ranges. Therefore, this section discusses the magnetic technology for achieving impeller/rotor non-contact support.

Olsen and Bramm patented the first fully magnetic levitation blood pump in 1986 [70] and Moise in 1987 [71]. In 1991, Akamasu's group successfully developed the first magnetic levitation centrifugal blood pump [72]. Later, CentriMag (Abbott Laboratories, Illinois, USA) [73-74], presented in Fig. 1.5, was developed and commercialized by Levitronix in 1995. It was the first clinically used fully magnetic levitation third-generation VAD. Essential products of the fully magnetic levitation, focusing on implantable type, include Berlin Heart INCOR [75] and HeartMate III [76].

Figure 1.5 Photograph of the CentriMag (Abbott laboratories, Illinois, USA).

Figure 1.6 illustrates two structures of CBP employing magnetic levitation technology. In Fig. 1.6 (a), magnetic bearings are situated externally to position the rotor in the radial direction and achieve passive stabilization in the tilt and axial directions without contact [77]. The magnetic coupling system is internally designed to rotate the impeller/rotor by the motor drive. Nevertheless, the complex mechanics of levitation and rotation increase the device size and impact the flexibility of the pump head design.

In Fig. 1.6 (b), a bearingless slice motor (BELSM) [78] is depicted for CBP application, incorporating suspension and motor coils into a unified stator. This design eliminates the need for an internal torque transmission device, resulting in a more compact and simplified structure. However, the intricate magnetic flux flows make the structure and control design of BELSM challenging.

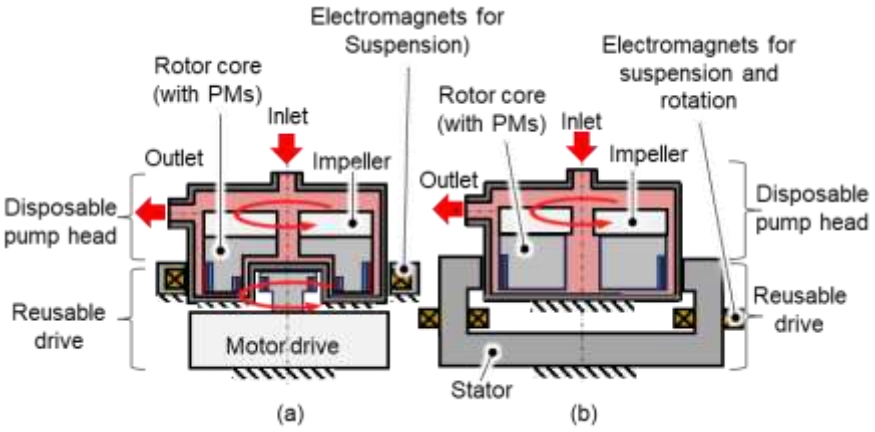


Figure 1.6 Centrifugal blood pumps with magnetic levitation technology: (a) Centrifugal blood pumps with magnetic bearings; (2) Centrifugal blood pumps with bearingless slice motor.

In contrast to the second generation of VADs, the third generation, utilizing magnetic levitation technology, achieves contactless support. This approach effectively addresses the mechanical wear induced by bearing friction, mitigating issues like thrombosis formation near the contact bearing and hemolysis caused by excessive shear stress and heat from the contact bearing.

## 1.3 Extracorporeal centrifugal blood pump employing BELSM

### 1.3.1 Principle of BELSM

Due to its compact and simpler structure, along with the characteristics of being lubrication-free and non-polluting, BELSM finds extensive use in the medical field, particularly in CBP. The BELSM concept was introduced to simplify system complexity and reduce the number of displacement sensors and electromagnets[78-79]. This concept is characterized by a slice rotor with a significantly larger diameter than its height, as shown in Fig. 1.7. The slice rotor can achieve passive support in tilt and axial directions through magnetic coupling in the radial air gap, as depicted in Figs. 1.8 (a) and (b), respectively. The electromagnet actively controls only two degrees of freedom (DOF) in the radial direction by measuring the radial displacements and constructing displacement feedback control, presenting a straightforward structure suitable for CBP application [80]. This design delivers sufficient torque for generating the necessary flow and head pressure while utilizing non-contact support to improve biocompatibility and durability. With sufficient passive stiffness in the tilt and axial directions to resist external disturbance and the hydrodynamic force on the impeller/rotor, it can avoid collision between the rotor and the pump housing. Additionally, this design enables

a thin slice rotor, reducing the pump head's size and minimizing the initial filling volume in CBP. Consequently, it addresses concerns related to transfusion infection and hemodilution mentioned in Section 1.1.3.

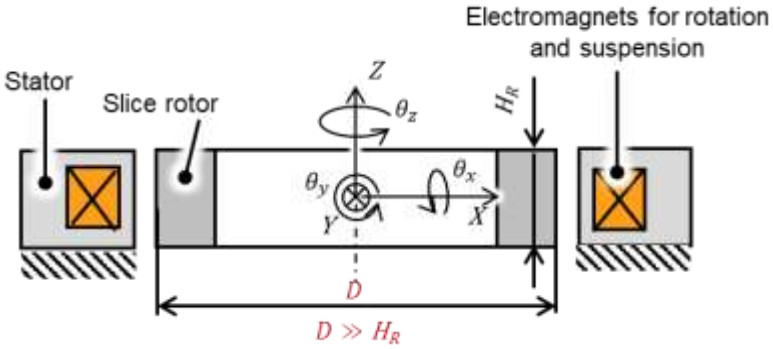


Figure 1.7 Schematic diagram of the BELSM structure.

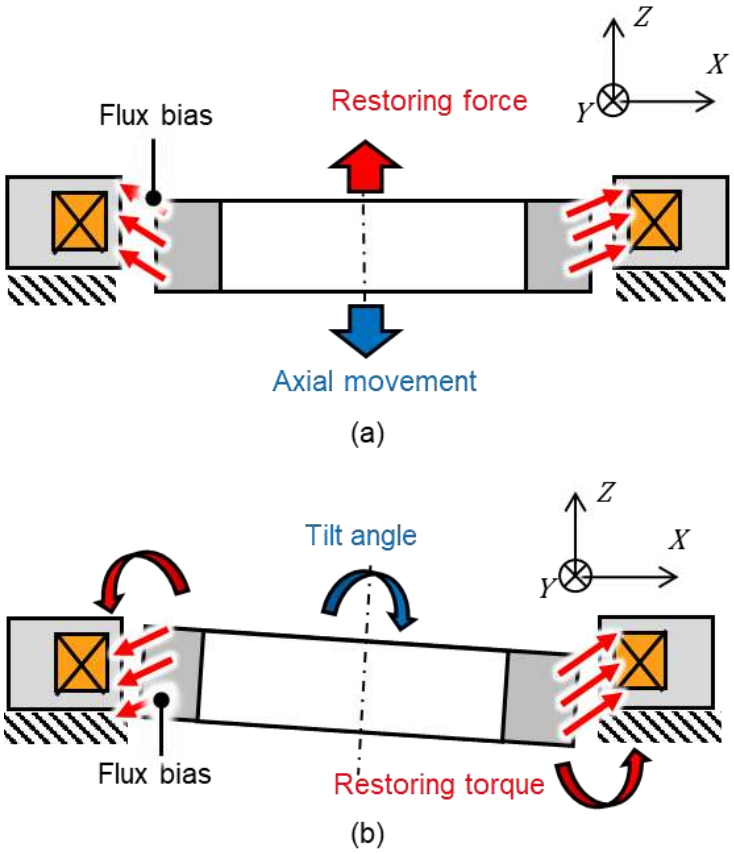


Figure 1.8 Principle of passive stiffness of BELSM: (a) Axial direction; (b) Tilt directions.

### 1.3.2 Requirements of BELSM for extracorporeal CBP application

As introduced in the preceding section, one of the most notable examples of in vitro CBP utilizing a BELSM is CentriMag. It has demonstrated good hemocompatibility and low tendency for thrombogenicity in clinical trials [81]. The CentriMag finds extensive application

in LVAD, RVAD, or BiVAD and is also employed as a blood pump in the ECMO circuit. However, the current significant challenge lies in its disposable cost.

The cost of a CentriMag encompasses capital equipment(console), CBP, canulae, additional components (tubes and probes), and maintenance. After converting the overall cost per patient for disposable use, it amounts to approximately 700,000 yen [82]. Notably, the incorporation of expensive rare-earth permanent magnets (PMs) on the impeller/rotor increases the disposable cost of the pump head.

Figure 1. 9 illustrates the historical prince changes of neodymium, a key element in rare-earth PMs. The price remains relatively high. Furthermore, the stable and long-term supply of rare earth elements is subject to influences from international relations. Moreover, excessive metal mining can also cause environmental pollution and damage the ecological environment.

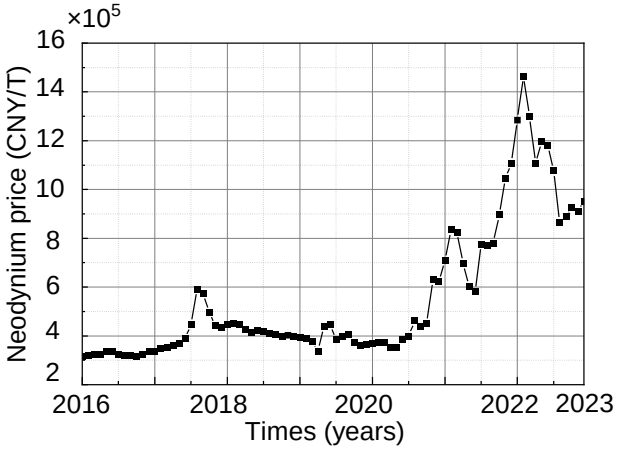


Figure 1.9 Historical prince changes of neodymium.

To mitigate disposable costs due to expensive PM embedded into the rotor and reduce the environmental issues caused by mining, BELSMs with reluctance rotor are considered the most mainstream choice, devoid of a rare-earth PM on the rotor. Reluctance rotors are essentially divided into two categories: a rotor with salient poles and a rotor with flux barriers [83-84]. The BELSM with a salient rotor operates as a double salient pole motor featuring salient poles on the stator and rotor core. On the other hand, the BELSM with a flux barrier rotor comprises a nonsalient stator and a round rotor. It incorporates magnetic paths with different reluctance symmetrically distributed around the rotor. Based on the structure of the reluctance rotor, the passive support and active magnetic levitation can be achieved by introducing PMs or additional windings on the stator to generate flux bias in the radial direction of the air gap. A BELSM with a PM-free rotor must satisfy the following requirements for CBP applications:

(1) Sufficient rotational torque and passive stiffness

For CBP application, an adequate air gap between the rotor and stator is required to ensure a sufficient fluid gap with the walls of the pump housing. The adequate thickness of the pump housing wall is guaranteed for the required mechanical strength of the pump head. Simultaneously, the fluid gap needs to be expansive enough to minimize shear stress and blood stagnation, thereby reducing the risks of hemolysis and thrombolysis.

Furthermore, given the rotor without embedding PMs, the magnetic flux density in the air gap becomes lower. If the volume of PMs is almost the same, due to the magnetic flux leakage, the PM placed on the stator produces a weaker magnetic field in the air gap than the PM placed on the rotor. The BELSM with a PM-free rotor must possess the capability to generate sufficient rotational torque and passive stiffness even with a relatively large air gap. This is essential to ensure that the CBP can achieve the required flow rate and head pressure for mechanical circulation while maintaining stable passive support.

(2) Suspension force and passive stiffness independent of rotor angle

Due to the structure of the rotor, the magnetic flux in the air gap varies in the circumferential direction during its rotation. On the one hand, the suspension force generation is, to some extent, coupled with the rotor angle, necessitating adjustments in the amplitude or even polarity of the current to stabilize the levitation. This increases the complexity of suspension control and demands higher accuracy in rotor angle measurement. On the other hand, the non-uniformity in passive stiffness at different rotor angles during the rotation can lead to unstable passive support and even failure, resulting in impacts between the rotor and pump housing.

(3) Small power consumption

Minimizing power consumption is crucial for energy efficiency, especially in applications where the BELSM operates continuously. Lower power consumption, including rotation and levitation, translates to reduced energy loss, such as heat generation, improving overall system efficiency, and increasing the usage time when running on a battery.

(4) Simple structure

The simple structure contributes to cost-effectiveness in terms of both materials and assembly. Additionally, the simplicity of the structure facilitates streamlined manufacturing and maintenance.

(5) Hollow design inside of the BELSM

Since the BELSM system is structurally crowded in the radial direction, consideration needs to be given to the placement of sensors, coil windings, and stators, which tend to occupy the space inside the rotor. If the internal structure of the BELSM lacks a hollow design, it will constrain the design flexibility of the pump head structure in space. This limitation can reduce the CBP performance, such as increasing the initial priming volume of the pump head and the complexity of the secondary flow path.

### 1.3.3 Prior-art of bearingless slice motor with a PM-free rotor

Section 1.3.2 discussed the design of a novel BELSM with a PM-free rotor to achieve magnetic levitation and passive stabilization. According to the method of generating flux bias, BELSM with a PM-free rotor is categorized into two types: stator-PM type BELSM and entirely PM-free type BELSM. Table 1.3 summarizes these two types of BELSMs [85-89].

#### *1.3.3.1 Stator-PM type BELSM with a PM-free rotor*

A heteropolar 12/10 flux-switching type BELSM [81] was proposed. This design incorporates alternately tangentially magnetized PMs within the stator poles, as shown in Fig. 1.10. The alternate flux bias is generated by these PMs for magnetic levitation and a high torque density. Despite these advantages, utilizing multiple magnets can result in a structurally complex motor and substantial flux leakage. Additionally, radial stiffness and current-force coefficient are dependent on the rotor angle, making the suspension control complicated.

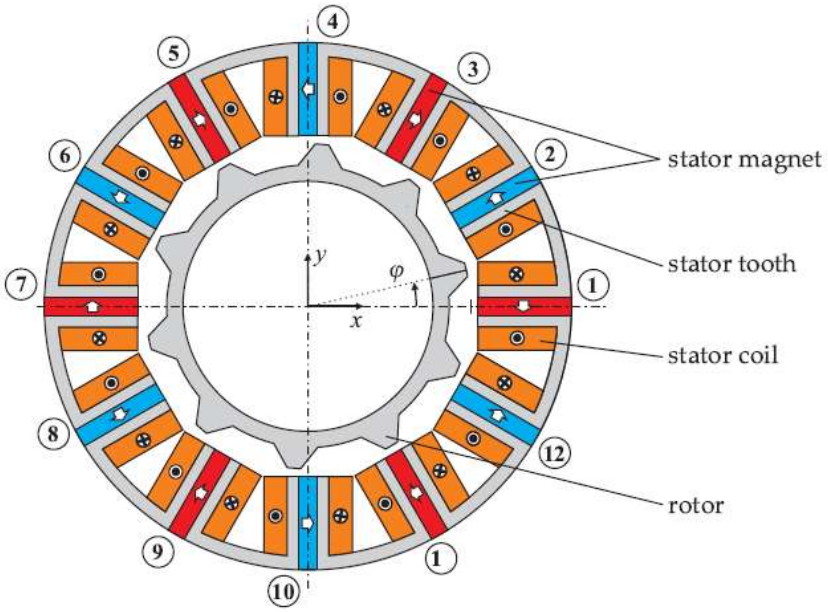


Figure 1.10 Stator PM type heteropolar flux-switching type BELSM in [81].

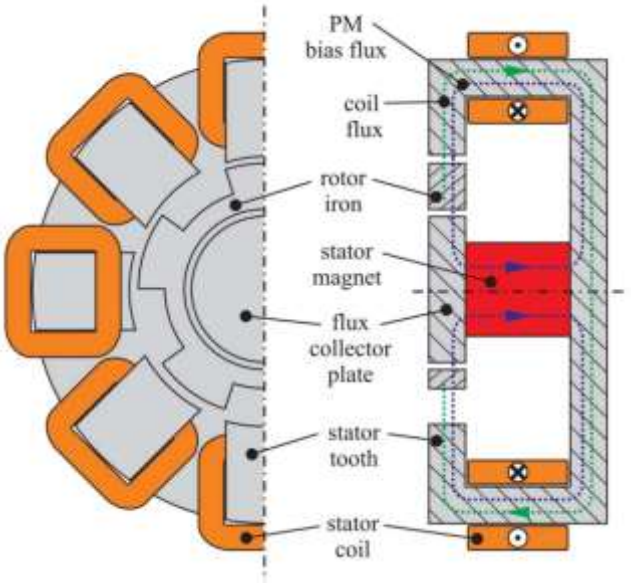


Figure 1.11 Stator PM type homopolar BELSM in [82].

A homopolar 6/4 BELSM [82] with a reluctance rotor was proposed, as illustrated in Fig. 1.11. The cylindrical stator PM is axially magnetized and positioned between the back yoke and flux collector plate. The flux bias generated by cylindrical stator PM travels from the flux collector plate, inner and outer sides of the rotor, stator teeth, and back yoke to form the homopolar vertical magnetic circuit. This BELSM structure is straightforward, and most of the magnetic flux generated by the current will not pass through the PM, reducing the risk of demagnetization of the permanent magnet. The suspension force generation is independent of the rotor angle. However, the cylindrical PM and the flux collect plate will occupy the internal space of the rotor, which is not conducive to the design of the pump head.

In [83], the author proposed a homopolar BELSM with flux-biasing Halbach arrays, as depicted in Fig. 1.12. This design incorporates PM Halbach rings symmetrically on the top and bottom of the stator tips and the rotor with top and bottom flange. Two PM rings with radial and axial magnetization are stacked to create a vertical homopolar triple-layer flux bias, reducing the leakage and reinforcing the passive stiffness. Eddy current displacement (ECD) sensors are installed inside the rotor to measure the radial displacement. This configuration ensures that magnetic flux generated by current will not pass through the PM to prevent demagnetization. However, the PM Halbach rings are overly complex and challenging to process and manufacture. Each PM Halbach ring comprises 36 arc-shaped magnets stacked using adhesive in three layers. Furthermore, large torque ripple and lower tilt stiffness are observed in the results.

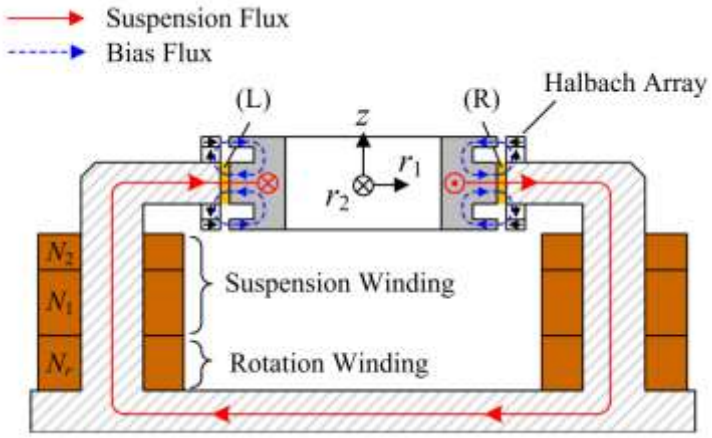


Figure 1.12 Stator PM type homopolar BELSM with flux-biasing halbach arrays in [83].

*1.3.3.2 Entirely PM-free type BELSM with a PM-free rotor*

To further reduce manufacturing costs and simplify the pump housing disassembly, entirely PM-free type BELSMs were proposed [84]. Thomas Holenstein *et al.* proposed a synchronous BELSM in a temple design, as illustrated in Fig. 1.13. Compared with a reluctance rotor with rotor teeth, this design employs a two-pole rotor with multiple parallel flux barriers to achieve a more consistent generation of suspension force and rotational torque with minimal fluctuations over the rotor angle. The bias flux is generated by maintaining a constant magnetization current in coil windings. Due to the weak magnetizing field in coil windings, passive stiffness and rotational torque are relatively lower than stator-PM type BELSM. Furthermore, the passive stiffness of this BELSM is dependent on the rotor angle. Simultaneously, using the current to maintain a constant magnetic flux bias for generating adequate passive stiffness leads to significant energy consumption and heat generation during long-term use, restricting operational time when powered by a battery.

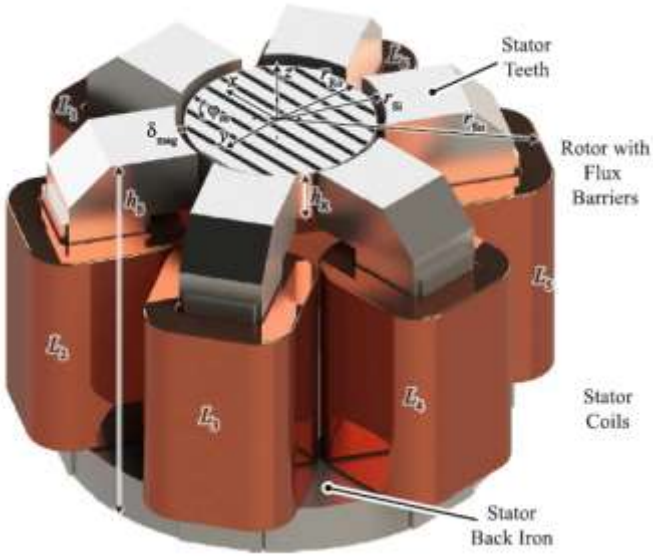


Figure 1.13 Entirely PM-free type synchronous BELSM in [84].

Table 1.3 Summary of the stator-PM type and entirely PM-free type BELSMs

| Motor authors reference | Flux bias generation | Suspension force | Passive stiffness | Others |
|---|---|---|---|---|
| Gruber [85] | Stator-PM | Dependent | Dependent | 1. Complex structure<br>2. Large flux leakage |
| Gruber [86] | Stator-PM | Independent | Independent | 1. Lower passive stiffness<br>2. Limited rotor inner space |
| Noh [87] | Stator-PM | Independent | Independent | 1. Complex structure<br>2. Lower tilt stiffness |
| Holenstein [88] | Entirely PM-free | Dependent | Dependent | 1. Large power consumption |
| Rao [89] | Entirely PM-free | Independent | Independent | 1. Large power consumption<br>2. Lower passive stiffness |

Our laboratory previously developed a 12/8 entirely PM-free type homopolar BELSM [85], as shown in Fig. 1.14. This configuration employs combined windings to generate rotational torque and suspension force simultaneously. Additionally, it corporates additional circular support coil windings, concentric with the rotor, utilized for generating the flux bias. The flux bias generated by the circular support coil traverses the rotor with two rotor teeth to form a homopolar double-layer magnetic circuit, following the same magnetic path as the suspension flux. This circular support coil winding allows real-time adjustment of passive

stiffness by controlling the amplitude of the current to diverse application scenarios. Despite these advantages, entirely PM-free type BELSMs still face the problems of excessive power consumption and heat generation.

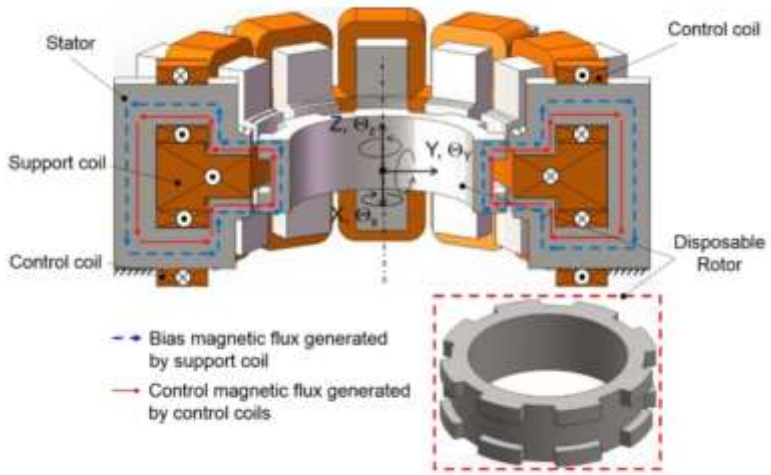


Figure 1.14 Entirely PM-free type BELSM in [85].

## 1.4 Research objective and motivation

As indicated in Table 1.4, current commercialized extracorporeal VAD products fail to meet the comprehensive requirements for high durability, high biocompatibility, compactness, and low disposable costs. Even the notably successful CentriMag may confront the challenge of high disposable costs. One contributing reason to the high disposable cost is the incorporation of expensive PMs in the disposable pump head. Furthermore, the excessive mining of metals utilized in PMs also contributes to environmental problems. Consequently, removing PMs from the disposable rotor is an urgent concern. This initiative aims not only to alleviate the economic burden on society but also to foster the environmentally friendly, widespread adoption of CBP in various applications, providing comprehensive support to the mechanical circulatory system of the human body.

Utilizing BELSM with a PM-free rotor for CBP is the predominant solution among researchers. To fulfill the operational demands of CBP and enhance CBP performance, the utilized BELSM must generate adequate rotational torque and passive stiffness, exhibit angle-independent magnetic suspension, entail small power consumption when running a battery, possess a simple structure, and incorporate an internal hollow design. However, previously proposed BELSMs by researchers have been unable to satisfy all these requirements simultaneously.

The objective of this thesis is to develop a cost-effective and highly biocompatible extracorporeal CBP with a small initial priming volume of disposable pump heads, which satisfies all the previously mentioned CBP needs. To achieve this, a disposable CBP employing a novel homopolar BELSM with a PM-free slice rotor is proposed, reducing the disposal cost, minimizing hemolysis and thrombus formation, and decreasing the pump head's size. Furthermore, the proposed BELSM can satisfy the requirements of sufficient rotational torque and passive stiffness, angle-independent magnetic suspension, small power consumption when running a battery, and simple structure.

Table 1.4 Characteristics of the blood pump for extracorporeal VAD

| | Positive displacement blood pump | Centrifugal blood pump | | | |
|---|---|---|---|---|---|
| | | Contact bearing | Magnetic bearing | BELSM (CentriMag) | BELSM (Research objective) |
| Durability | Low | Low | High | High | High |
| Biocompatibility | Low | Low | High | High | High |
| Size | Large | Large | Large | Small | Small |
| Disposable cost | High | Medium | High | High | low |

Besides, for BELSM rotors characterized by complex and salient pole structures, a novel approach to measure radial displacement by installing the ECD sensors below the rotor is proposed. This method achieves the requirements of hollow design inside of the BELSM, which enhances flexibility in rotor design and pump housing configuration to improve CBP performance.

## 1.5 Thesis outline

The rest of this doctorate thesis is organized as follows:

In Chapter 2, "Principle and design," the objective is to design a BELSM capable of generating sufficient rotational torque and passive stiffness for blood circulation with artificial lung (Flow rate: 5 L/min, Head pressure: 250 mmHg), featuring a simple structure, low power consumption, and rotor angle-independent suspension control. To fulfill this objective, a 12/8 homopolar BELSM with a PM-free rotor is proposed. This BELSM design incorporated two PM rings and iron rings positioned at the ends of the stator teeth, which can reduce the power

consumption for generating flux bias. The two PM rings and sandwiched motor form a multi-layer homopolar flux bias with a triple-layer rotor structure, which helps achieve passive support in the axial and tilt directions. The twelve coil windings are divided into four groups, each comprising three phases: U, V, and W. Two opposing groups achieve radial suspension control in the x- and y-directions Through finite element method (FEM) simulations, the proposed BELSM with a PM-free rotor have shown the capability to produce a sufficient average rotational torque and significant passive stiffness for blood circulation and magnetic suspension stability, while also achieve rotor angle-independent suspension control and passive stabilization.

In Chapter 3, “Prototype fabrication,” the proposed BELSM of the above design and a disposable pump head were fabricated, and then were assembled the two components. Concurrently, the radial displacement and rotor angle sensors were chosen and discussed, considering their type, model, and placement location. Moreover, two types of power amplifiers to transfer energy were also considered and discussed. Furthermore, suspension and rotation feedback systems tailored to the chosen hardware components were established.

In Chapter 4, “Performance evaluation, ” a mock circulatory loop filled with 40 wt% glycerol water was constructed. Suspension and rotation performance of the proposed BELSM were first assessed. Subsequently, the CBP performance was evaluated, achieving a maximum pressure of 214.5 mmHg and a flow rate of 4.59 L/min, falling short of the goal. The limitation reasons and solution were also discussed in this chapter.

In Chapter 5, “Radial displacement measurement using ECD sensors below the rotor, ” a novel approach to measure radial displacement by installing the ECD sensors beneath the inner edge of the rotor is proposed. Compared to the conventional placement of locating it on the rotor’s inner side, this placement enhances the design flexibility of the disposable pump head. A seven-sensors arrangement method is proposed to address nonlinearity and multiple degree-of-freedom (DOF) displacement interference. A polynomial fitting method and a neural network (NN) method were employed to calibrate numerous sensors during motion across multiple DOFs. However, the polynomial fitting method results in large unacceptable measurement errors, while the NN method can precisely fit the relationship between the output of sensors and radial displacement. The radial feedback control for the rotor during startup and rotation was successfully achieved using the NN method. The influence of the dataset for NN training and the number of sensors on the measurement accuracy were also discussed.

Chapter 6, “Conclusion,” summarizes the results of each chapter and lists possible future plans.

# Chapter 2 Principle and design

## 2.1 Introduction

Extracorporeal VADs play a crucial role in providing mechanical circulatory support for the human body to treat heart failure, requiring high durability, biocompatibility, compactness, and low disposable cost. Leveraging BELSM technology in extracorporeal VAD, the CentriMag stands out for its use of magnetic levitation, enabling contactless support and achieving a compact design by eliminating torque transmission mechanisms. However, incorporating PMs in the impeller/rotor raises the cost of disposable pump heads and causes environmental issues.

To address these challenges, an extracorporeal CBP utilizing a BELSM with a PM-free rotor is needed. However, current research on BELSM with a PM-free rotor cannot simultaneously satisfy the demand for sufficient rotational torque and passive stiffness, angle-independent magnetic levitation, small power consumption when running a battery, and simple structure.

Therefore, the objective of this chapter is to propose a novel configuration of the BELSM with a PM-free rotor that can meet all of the requirements mentioned above. The principles of tilt and axial passive stiffness, radial suspension force generation, and rotational torque generation of the proposed BELSM will be introduced. Besides, the design target and FEM simulation results based on the numerical model will also be discussed.

## 2.2 Configuration of proposed BELSM with a PM-free rotor

To facilitate the BELSM design, two fundamental aspects must be considered:

- The rotor structure and coil windings design;
- The flux bias generation and magnetic circuit.

As mentioned in Section 1.3.2, the reluctance rotors of BELSM are primarily categorized into a rotor with salient poles and a rotor with flux barrier types, and the coil windings are also divided into concentrated and distributed windings [90]. Compared to the rotor with flux barriers, the rotor with salient poles structure is more straightforward, eliminating the need for intricate flux barrier designs of the rotor's inner structure and resulting in a more cost-effective solution [91-92]. Compared to distributed windings, coil windings wound around the stator

poles can provide enhanced compactness, improved coil manufacturability, and reduced copper loss [90]. However, the BELSM with a rotor with salient poles has a large torque ripple due to a large difference when the rotor and stator salient poles are aligned and unaligned [93]. The large torque ripple is reduced by modifying the phase current commutation method, which will be elaborated in Section 2.5.4.

Section 1.3.2 categorized BELSM into stator-PM and entirely PM-free types regarding flux bias generation. As discussed in Section 1.3.3, the entirely PM-free types have a significant drawback: a substantially constant current input is required to generate flux bias to ensure the continuous generation of passive stiffness for mid and long-term VAD use. This drawback results in excessive energy consumption, posing challenges for battery-powered applications. The Stator-PM type BELSM will be chosen to address this energy consumption issue.

Additionally, these motors can be classified into homopolar and heteropolar type BELSM [94] based on whether the direction of the magnetic field in the air gap changes along the circumference, such as homopolar BELSM in Fig. 1.11 [86] and heteropolar flux-switching type BELSM in Fig. 1.10 [85]. In homopolar types BELSM, the flux bias maintains a consistent polarity around the circumference, requiring a vertical magnetic circuit (as in entirely PM-free type BELSM in Fig. 1.14 [89]) or passing through both inner and outer air gaps (as in homopolar BELSM in Fig. 1.11 [86]). This configuration forms a multi-layer sliced unipolar magnetic field in the vertical or horizontal directions, enhancing passive stiffness.

### 2.2.1 12/8 double salient structure of the proposed BELSM

The proposed 12/8 double salient BELSM structure with a PM-free rotor is depicted in vertical and horizontal cross-sectional views in Figs. 2.1 and 2.2. The configuration of the BELSM closely resembles that of a conventional 12/8 switched reluctance motor. The rotor, which is only constructed from soft iron, adopts a triple-layer slice structure. The top and bottom layers are doubly flanged and opposed by iron rings. The middle layer features eight rotor teeth opposing the stator poles.

Twelve-pole stators are composed of laminated steel with evenly distributed poles. Every stator pole is linked to a sizable stator ring along its periphery through designated slots. Each stator pole is wound with a concentrated winding. The current in each concentrated winding encompasses rotation and suspension current, enabling the simultaneous generation of rotational torque and radial suspension force. Such coil winding is later called combined winding

The twelve coil windings are divided into four groups: $X_n$, $X_p$, $Y_n$, and $Y_p$, with each group having three phases U, V, and W, as illustrated in Fig. 2.2. Opposing groups, such as $X_n$ and $X_p$, serve to generate the suspension flux for the radial displacement positioning in one direction. The U, V, and W phase windings are utilized in rotational control for phase current commutation.

The adaption of a 12/8 BELSM structure is a tradeoff between easy angle-independent magnetic levitation, simple structure, and the demands of high-frequency equipment. The twelve stator teeth wounded the concentrated winding can be well arranged in the orthogonal radial direction and each six stator coil windings control the radial displacement in one direction. The eight rotor teeth can avoid excessive changes in the magnetic reluctance with the rotor angle around the circumference. Therefore, the angle-independent active magnetic levitation and passive magnetic levitation can be realized, which will be verified by the simulation in Section 2.5. Besides, avoiding the use of additional rotor teeth simplifies the structure and alleviates the need for high-frequency equipment to handle excessive electrical frequencies.

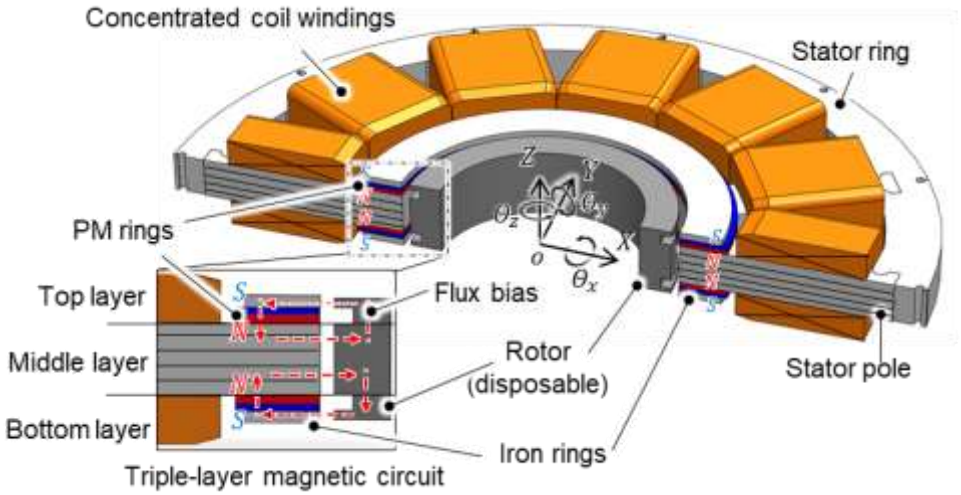


Figure 2.1 Vertical cross-sectional view of the proposed BELSM.

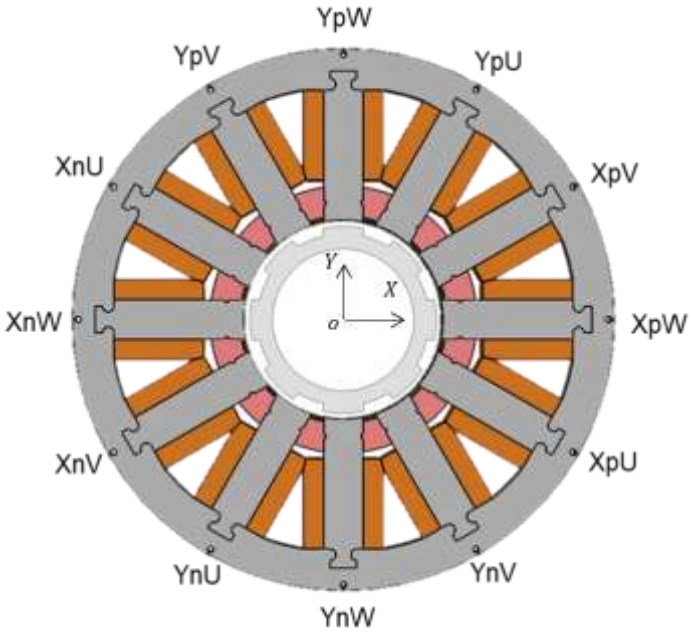


Figure 2.2 Horizontal cross-sectional view of the proposed BELSM.

### 2.2.2 Homopolar triple-layer magnetic field

Two axially magnetized PM rings are symmetrically positioned above and below the tips of the stator poles near the rotor. This arrangement avoids flux leakage and intensifies the magnetic field strength within the air gap between the stator and rotor. Two iron rings are affixed externally to the PM rings to focus the magnetic flux bias, enabling magnetic levitation, passive stabilization, and rotation. The magnetic flux bias travels through the stator pole, rotor teeth, two rotor flange, and the two iron rings, forming two enclosed vertical homopolar magnetic circuits.

The proposed BELSM utilizes a triple-layer slice structure rotor to create a triple-layer slice homopolar magnetic field, as depicted in Fig. 2.1. The flux bias generated by PM rings pass through the air gap from the rotor flange to the iron rings in the top and bottom layers, while the middle layer's magnetic field combines the flux bias from the PM rings with the magnetic flux generated by the coil windings. Compared with the typical two-layer homopolar magnetic field structure, this triple-layer homopolar magnetic field structure increases the magnetic flux in the air gap by adding layers, thereby enhancing passive stiffness in the axial and tilt direction to improve magnetic suspension stability against disturbances.

## 2.3 Working principle

The BELSM must exhibit sufficient passive stiffness for stable levitation against the fluid forces generated within the CBP and rotational torque for blood circulation. In BELSM, the restoring force and torque are generated by the flux bias in the air gap based on the least reluctance principle. Only radial direction is actively controlled by the displacement feedback system. This section will describe the principles of magnetic suspension and rotation of the proposed BELSM. Simultaneously, the advantages of our proposed structural design will be introduced.

### 2.3.1 Passive stiffness principle

Due to the triple-layer slice structure, the rotor is passively stabilized in the axial and tilt directions, simplifying the control system and reducing power consumption, as depicted in Fig. 2.3. If the rotor experiences axial movement or tilt, the triple-layer homopolar magnetic field will generate restoring reluctance forces and torque in line with the principle of least reluctance. The restoring reluctance force and torque are proportional to the axial displacement and tilt angle over small deviation ranges, respectively. Owing to the increased slice fringing flux by the triple-layer field, the proposed BELSM achieves enhanced passive stiffness.

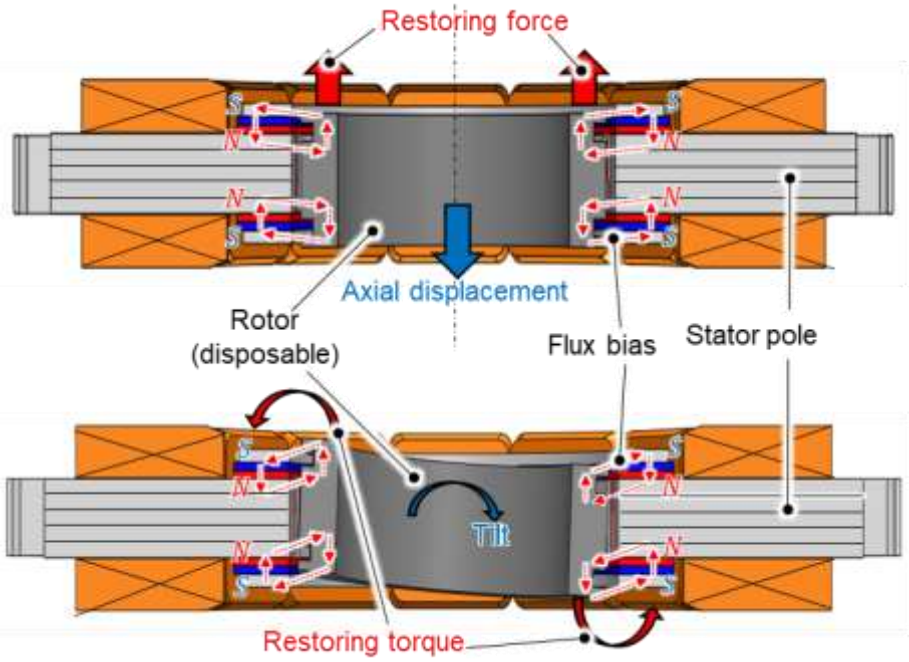


Figure 2.3 Principle of passive stiffness in the axial and tilt directions by flux bias generated by PM rings.

2.3.2 Suspension force generation principle

Due to the negative stiffness in the radial direction, feedback control for radial positioning in the X- and Y-directions is essential to produce a radial restoring force and prevent contact between the stator and the rotor. Figure 2.4 depicts the principle of radial force generation. The two groups of coil windings $X_n$ and $X_p$ are energized with negative and positive current, respectively, generating a suspension flux in the X-direction, as shown by the yellow lines in Fig. 2.4. The magnetic flux density in the air gaps varies due to the superposition of the flux bias generated by the PM rings and suspension flux. This variation weakens the magnetic flux density in the air gap toward the rotor's displacement and strengthens it in the opposite direction. Consequently, a restoring force arises due to the differences in magnetic flux density, pushing the rotor back to the equilibrium point. Furthermore, the suspension flux generated by the current is theoretically directed away from passing through the PM ring by designing an appropriate PM ring thickness. This design prevents the demagnetization of the PM and reduces magnetic reluctance, thereby enhancing the radial position force.

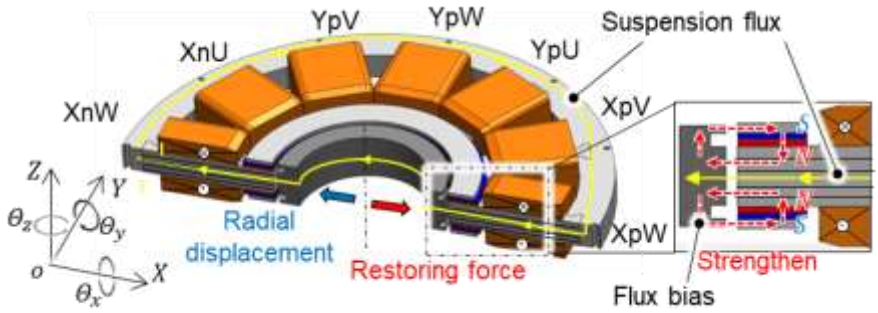


Figure 2.4 Principle of suspension force generation.

2.3.3 Torque generation principle

The torque generation in the proposed BELSM motor differs from traditional switched reluctance motors due to the flux bias from the stator to the rotor in the air gaps. In this design, the magnetic flux generated by each group of coil windings in one phase must also be directed from the stator to the rotor to enhance the magnetic flux. Figure 2.5 illustrates the principle of rotational torque generation. The magnetic flux in the air gap comprises the flux bias from the PM rings and the magnetic flux generated by the coil windings. Consequently, the BELSM's torque includes both reluctance and permanent magnet torque. The twelve coil windings are grouped into four groups, each containing U, V, and W phase windings, as depicted in Fig. 2.5. The coil windings of U, V, and W phases are injected with current in sequence. The magnetic flux generated by the energized U phase winding, shown in Fig. 2.5 as the green line, enters

the rotor along with the flux bias, increasing the local magnetic flux density in the air gap. The magnetic flux passing through the rotor exits from the V and W stator poles, creating two closed circuits and reducing the magnetic density at corresponding locations. The variation in magnetic flux density in the air gap generates an attractive tangential force to align the rotor teeth with the stator poles of the energized phases. Continuous rotation of the rotor occurs based on the commutation of three-phase windings.

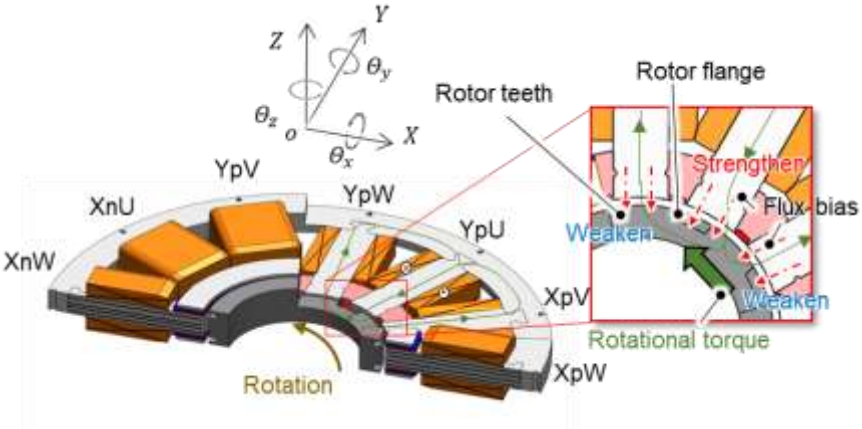


Figure 2.5 Principle of rotational torque generation.

## 2.4 Design target

The extracorporeal CBP must fulfill specific performance requirements to pump blood effectively in L-VAD, R-VAD, and ECMO [95-97]. For left ventricular assist, a mean pressure rise of 100 mmHg is necessary, while right ventricular assist requires a mean pressure rise of 20 mmH. Additionally, a mean flow rate of at least 5 L/min is essential to support adult circulation adequately. CBP used for ECMO should ideally achieve a flow rate of 5 L/min against a pressure head of 250 mmHg, accounting for pressure losses in the artificial lungs.

To begin with, the choice of rotor dimension is a crucial step. From prior research [67], the rotor diameter has been determined as 50 mm, striking a trade-off between achieving a small priming volume of the pump head and meeting the required rotational speed and pump efficiency. The rotor's height has been set at approximately 14 mm to ensure adequate passive stiffness and also reduce the initial priming volume of the pump head. For miniaturization, the outer diameter of the motor is kept under 150 mm when utilizing a planar stator.

The air gap between the rotor and the stator has also been designated 1.5 mm. This thickness includes the 0.4 mm thickness of the rotor's biological waterproof coating to prevent contact between the rotor and blood. Moreover, it also includes a 0.2 mm fluid gap to mitigate the risk of severe local hemolysis and thrombosis. The side wall thickness of the bottom pump

housing is set to be 0.9 mm to ensure the required mechanical strength to withstand the impact of the rotor.

Building upon earlier investigations [67], based on the above rotor dimensions, the required rotational speed of the rotor is 3000 rpm, generating an average rotational torque of 0.060 Nm, which can meet blood circulation needs, specifically up to 5 L/min against 250 mmHg. Beyond torque generation, it has been investigated from prior research that the passive stiffness must surpass 9.7 N/mm in the axial direction, accompanied by a 2.3 Nm/rad in the tilt direction [98]. Table 2.1 summarizes the design targets of dimensions and performance in BELSM.

Figure 2.6 summarizes the design targets of rotational torque and passive stiffness alongside the corresponding values from the other BELSM with a PM-free rotor from previous research. The rotor diameter of these previous BELSMs is approximately 50 mm. However, these BELSMs cannot meet the requirements of rotational torque and passive stiffness. In the next section, the numerical simulation model of the proposed BELSM will be introduced. The results of the FEM simulation will be shown and compared with the design target.

Table 2.1 Summary of the design target of dimensions and performance in BELSM

| Dimensions | | Performance | |
|---|---|---|---|
| Rotor diameter | 50 mm | Average rotational torque | 0.060 Nm |
| Rotor height | 14 mm | Axial stiffness | 9.7 N/mm |
| Magnetic air gap | 1.5 mm | Tilt stiffness | 2.3 Nm/rad |

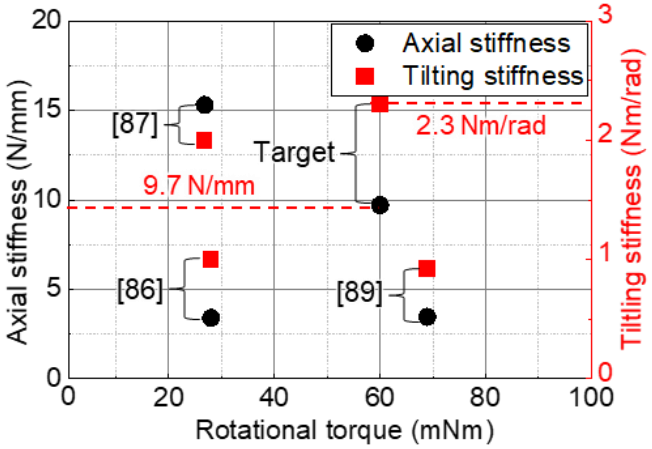


Figure 2.6 Design targets of rotational torque and passive stiffness alongside the corresponding values from the previous BELSM with a PM-free rotor.

## 2.5 Finite element model simulation

### 2.5.1 Numerical simulation model

In this section, the simulations are performed using the 3-D model via the finite element analysis (FEA) software (Ansys, Maxwell 19.0) to estimate the suspension stiffness, current-force coefficient in the radial direction, and motor torque of the proposed BELSM. Figure 2.7 illustrates the numerical simulation model with the rotor at the geometrical center of the BELSM and the initial rotor angle set as the W phase stators aligned with the teeth. Table 2.2 provides a summary of the dimensions of the 3D model of the proposed BELSM. Table 2.3 details the material properties and winding configurations of the simulation model. The number of turns of concentrated coil winding is 386. The total number of mesh elements in the 3D FEA electromagnetic static simulation reached 1384492.

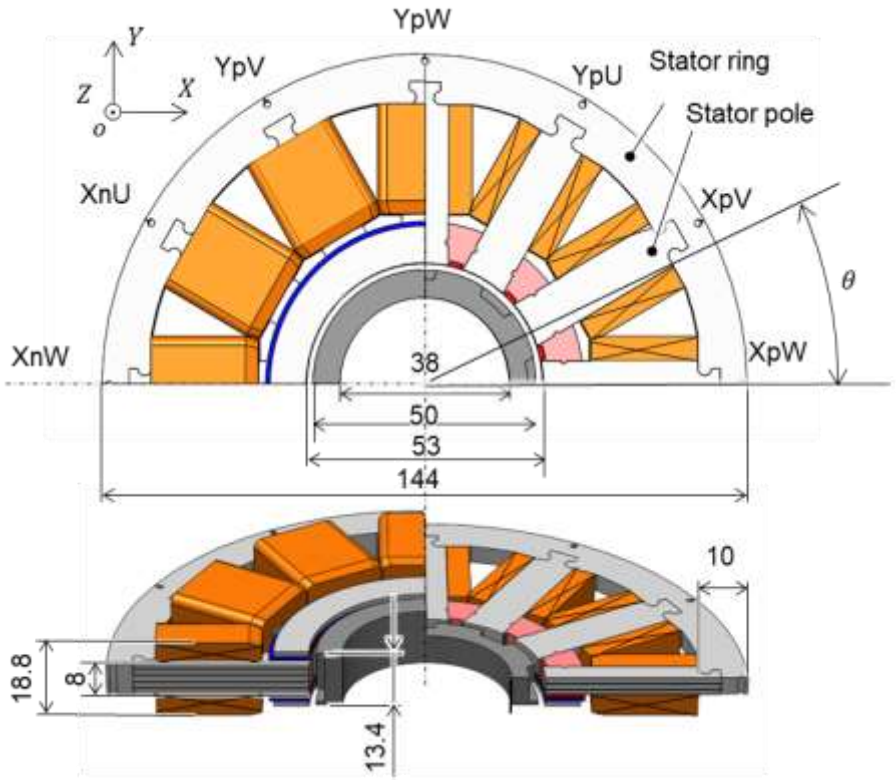


Figure 2.7 3D simulation model of the proposed BELSM.

Several structural parameters were examined to generate the required rotational torque by enhancing the magnetic flux bias in the air gap and the cross-sectional area of the coil for sufficient magnetomotive force. Firstly, the thickness of the PM rings and the iron ring's outer diameter was changed, respectively, to increase the magnetic flux bias in the air gap and enhance the rotational torque. Subsequently, the outer diameter of the stator rings was assessed to boost the cross-sectional area of the coil.

The angular position $\theta$ is defined as 0° where the W phase stator pole aligns with the rotor teeth. The mechanical angle for an entire electrical cycle is 45 degrees due to the symmetric arrangement of twelve stator poles and eight rotor teeth. Fig. 2.8 (a) exhibits the side cross-sectional view of the magnetic field distribution at the angular position of 0°, showing a homopolar magnetic coupling generated by the PM rings. Furthermore, Fig. 2.8 (b) illustrates the top cross-sectional view of the magnetic field distribution at the angular position of 0°. The magnetic field around the air gap varies due to the rotor teeth and stator poles.

Table 2.2 Simulation dimensions of the 3D model of the proposed BELSM

| Component | Dimensions (mm) | | Component | Dimension (mm) | |
|---|---|---|---|---|---|
| Rotor | Height | 13.4 | Stator | Outer diameter | 144 |
| | Outer diameter | 50 | | Inner diameter | 53 |
| | Inner diameter | 38 | | Thickness | 8 |
| | Flange thickness | 1 | PM ring | Thickness | 1.8 |
| | Groove depth | 2 | | Inner diameter | 53.1 |
| | Teeth thickness | 7.8 | | Outer diameter | 71 |
| Iron ring | Thickness | 1.3 | | | |
| | Inner diameter | 53 | | | |
| | Outer diameter | 69 | | | |

Table 2.3 Simulation material properties and winding configurations of the simulation model of the proposed BELSM

| Component | | Conditions | Component | | Conditions |
|---|---|---|---|---|---|
| Coil | Total cross-section area [$mm^2$] | 124.8 | PM ring | Type | NdFe35 |
| | Turns | 386 | | Coercive force [kA/m] | 890 |
| Rotor | | Soft iron | | Remanence [T] | 1.20 |
| Stator | | Lamination steel | Iron ring | | Soft iron |

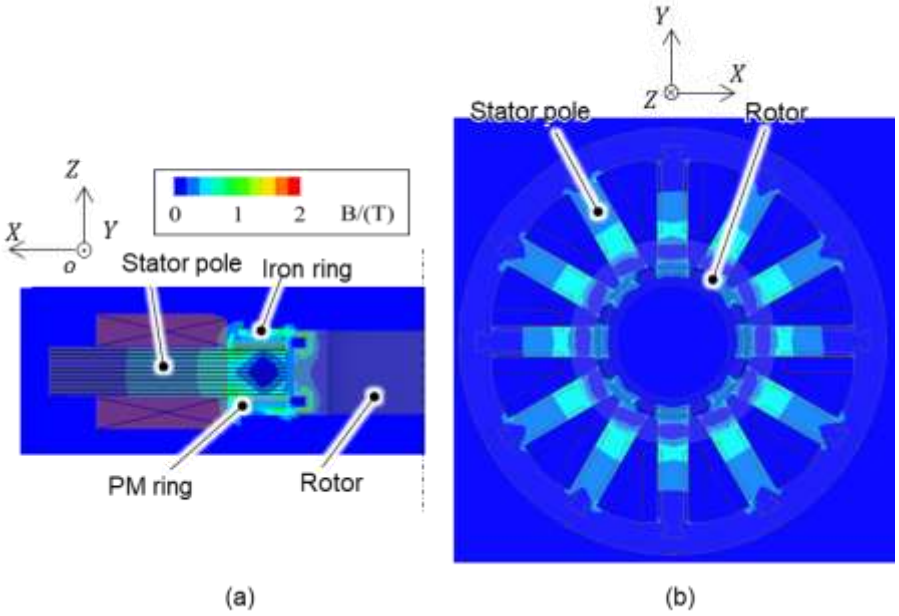


Figure 2.8 Magnetic field distribution at the angular position of 0°: (a) Side cross-sectional view; (b) Top cross-sectional view.

### 2.5.2 Passive stiffness simulation

In the FEM simulation, the axial and tilt stiffness $K_z$ and $K_\theta$ were calculated by recording the slopes of restoring force concerning axial displacement (ranging from 0 to 0.3 mm) and the slopes of restoring torque versus tilt angle (ranging from 0 to 30 mrad), respectively. Figures 2.9 (a) and (b) depict the simulation results for restoring force and torque at different rotor positions, considering rotor mechanical angles of 0° and 22.5° degrees. Linearization curves were plotted to calculate passive axial and tilt stiffnesses.

When the mechanical angle is 0° or 22.5°, the simulated $K_z$ is 18.5 N/mm or 18.0 N/mm, respectively, and the simulated $K_\theta$ is 5.9 Nm/rad or 5.3 Nm/rad, respectively, which demonstrates the proposed BELSM is characterized by angle-independent passive stiffness.

Moreover, the simulated passive stiffness values in the axial and tilt directions surpass the target values. This enhancement is attributed to the air gap's triple-layer sliced homopolar magnetic field, increasing fringing flux compared to prior single-layer or double-layer structures. Table 2.4 summarizes the values of $K_\theta$ and $K_z$ with mechanical angles of 0° and 22.5° and compares them with the target values.

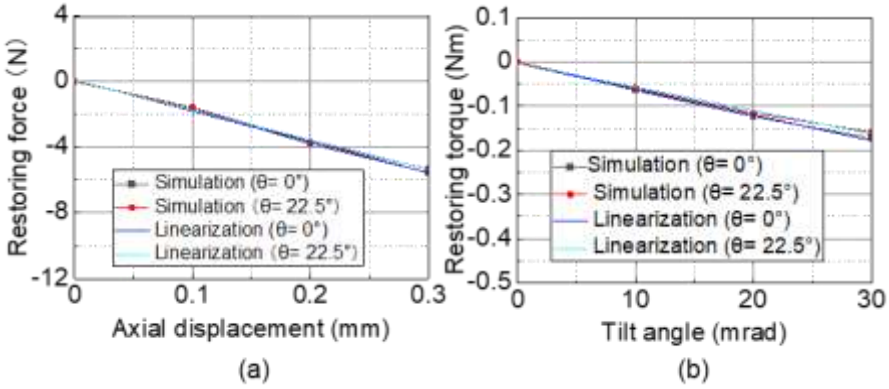


Figure 2.9 Passive stiffness with mechanical angles of 0° and 22.5°: (a) Axial direction; (b) Tilt direction.

### 2.5.3 Radial negative stiffness and current-force coefficient simulation

The radial negative stiffness and current-force coefficient, $K_c$ and $K_s$, are determined via linear fitting involving radial forces. This was achieved by varying the input current of the coil windings from 0 to 1 A and the rotor position in the radial direction from 0 to 0.3 mm. In Fig. 2.10 (a), the simulation results illustrate the attractive force at varying radial displacements, considering mechanical angles of 0° and 22.5°. Figure 2.10 (b) displays the positioning force with different input currents at mechanical angles of 0° and 22.5°. Linearizations were employed to determine the radial negative stiffness and current-force radial coefficient.

When the mechanical angle is 0° or 22.5°, the simulated $K_c$ is 19.3 N/A or 16.1 N/A, respectively, and the simulated $K_s$ is -60.4 N/mm or -56.3 N/mm, respectively, which demonstrates the proposed BELSM can achieve angle-independent radial suspension control, allowing for straightforward direct current (DC) control. Table 2.4 summarizes the values of $K_c$ and $K_s$ with mechanical angles of 0° and 22.5° and compares them with the target values.

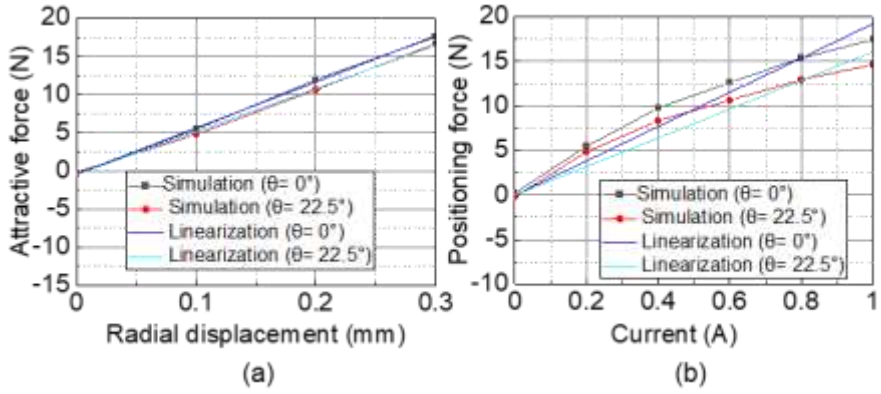


Figure 2.10 (a) Negative stiffness with mechanical angles of 0° and 22.5°; (b) Current-force coefficient with mechanical angles of 0° and 22.5°.

2.5.4 Rotational torque simulation

The simulation of rotational roque involved the exploration of different phase excitation methods dependent on the mechanical angle of the rotor. Both single-phase and dual-phase excitation methods were assessed to understand their impact on the torque ripple and to calculate the average torque over one electrical cycle.

The conventional single-phase excitation method was employed, where each of the U, V, and W phases was alternately energized during rotation over a mechanical angle of 45°, as depicted in Fig. 2.11. In contrast, the dual-phase excitation method energized each phase during rotation through a mechanical angle of 19° for each phase. The excitation period of each phase overlapped with that of another phase, as shown in Fig. 2.11.

The rotational torque was calculated with a square commend current of 1.2 A. Figure 2.12 illustrates the rotational torque versus rotor angle with the two different phase excitation methods. Notably, there's a significant drop in rotational torque with the conventional single-phase excitation method due to current switching between the two phases at the end of the 15° mechanical angle rotation, as shown in Fig. 2.12. In this position, where rotor teeth align with the energized stator pole, the rotational torque cannot be produced due to the minimal change in magnetic resistance between the rotor teeth and the stator pole. The dual-phase excitation method was implemented to address this, ensuring that the next energized winding of the stator pole is energized earlier and attracts the corresponding rotor teeth in advance. This helps nullify the absence of torque generation at 15°, reducing torque ripple and increasing average torque. The calculation results of the average torque $T_d$ using the dual-phase excitation method are also presented in Table 2.4, along with the target value.

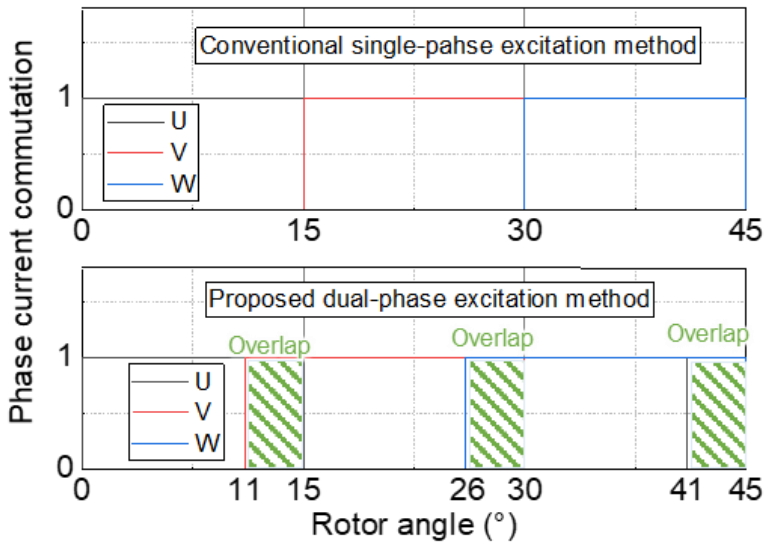


Figure 2.11 Dual-phase and single-phase current excitation methods.

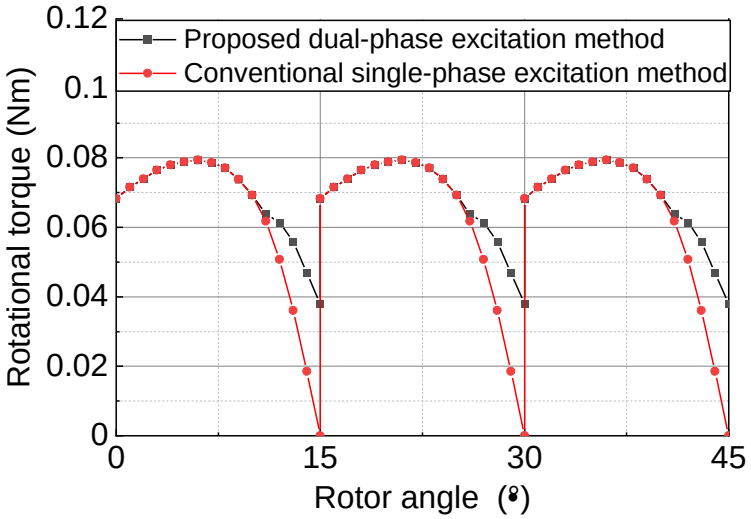


Figure 2.12 Rotational torque using the dual-phase and single-phase excitation methods.

Table 2.4 Target values and FEM simulation results for the proposed BELSM

| Parameters | Target values | Simulated results | |
|---|---|---|---|
| | | Rotor angle = 0° | Rotor angle = 22.5° |
| Negative stiffness $K_s$ [N/mm] | - | -60.4 | -56.3 |
| Current-force coefficient $K_c$ [N/A] | - | 19.3 | 16.1 |
| Axial stiffness $K_z$ [N/mm] | 9.7 | 18.5 | 18.0 |
| Tilt stiffness $K_\theta$ [Nm/rad] | 2.3 | 5.9 | 5.3 |
| Average torque $T_d$ [Nm] | 0.060 | 0.068 | |

## 2.6 Summary

This chapter presents the 12/8 BELSM structure and working principle, highlighting its key innovations. Placing two PM rings and two iron rings above and below the stator pole tip is a significant structural enhancement, providing a vertical and uniform homopolar magnetic field in the air gap. The benefits of this proposed design include:

- **Cost-effectiveness flux bias generation**: The magnetic field in the air gap generated by the two PM rings eliminated the large power consumption associated with continuous current-induced flux linkage for sufficient passive stiffness.
- **Enhanced passive stiffness**: The flux bias generated by PM rings, combined with the triple-layer rotor structure, forms a triple-layer magnetic circuit in the air gap, significantly boosting passive stiffness beyond the target value.
- **PM demagnetization prevention**: The structure avoids current flux generated by the coil winding passing through the PM rings, preventing PM from demagnetization and increasing the suspension force of the BELSM.
- **Angle-independent passive stiffness**: Passive stiffness remains independent of rotor angle due to a uniform distribution of the flux bias in the air gap
- **Angle-independent radial suspension force**: The radial suspension force, controlled by six-coil windings in a single direction, remains independent of the rotor angle.
- **Torque generation from flux bias**: The flux bias also generates the permanent magnet torque to improve the rotational torque using the proposed dual-phase current excitation.

3-D FEM simulations were conducted to assess the motor's performance, and simulation results of the parameters aligned well with the target value. The motor achieves independent passive support and active suspension control regardless of the rotor angle. The passive stiffness values in the axial and tilt directions surpass the target, reaching 18.5 N/mm and 5.9 Nm/rad, while the average torque of 0.068 Nm with a reduced torque ripple is achieved through the proposed dual-phase current excitation method.

In the next chapter, based on the principle and design of the simulation model, the proposed BELSM will be fabricated. Moreover, the other related components of the CBP system, such as electrical components and control systems, will also be introduced.

# Chapter 3 Prototype fabrication

## 3.1 Introduction

Chapter 2 introduced the design and working principles of the proposed BELSM with a PM-free rotor. This design has the advantages of sufficient rotational torque and passive stiffness, cost-effective flux bias generation, angle-independent magnetic levitation, and simple structure. The prototype of the CBP utilizing the proposed BELSM is fabricated in Chapter 3 based on the design model.

The objective of this chapter is to conduct a trial fabrication of the CBP utilizing the proposed BELSM, including the manufacturing and assembly of the BELSM and pump head mechanical structures, the selection and design of the electrical system, and the construction of the suspension and rotation control system.

Figure 3.1 (a) shows a photograph of the CBP prototype with a digital signal processor (DSP) and linear power amplifiers. Figure 3.1(b) shows the detailed CBP utilizing the proposed BELSM structure.

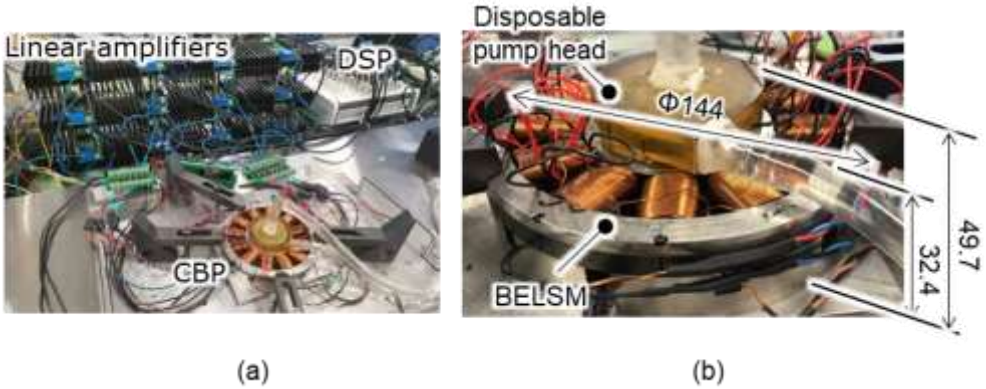


Figure 3.1 Photograph of the CBP system: (a) Entire system; (b) CBP utilizing the proposed BELSM.

## 3.2 Mechanical structure of the entire system

The proposed BELSM was fabricated based on the dimensions obtained from the numerical simulation model. A schematic of the mechanical structure of the CBP utilizing the proposed BELSM is presented in Fig. 3.2. The disposable pump head is vertically inserted into the BELSM stator until the bottom housing contacts the upper iron rings on the stator. Compared with the CentriMag shown in Fig. 1.5 the overall size is slightly larger.

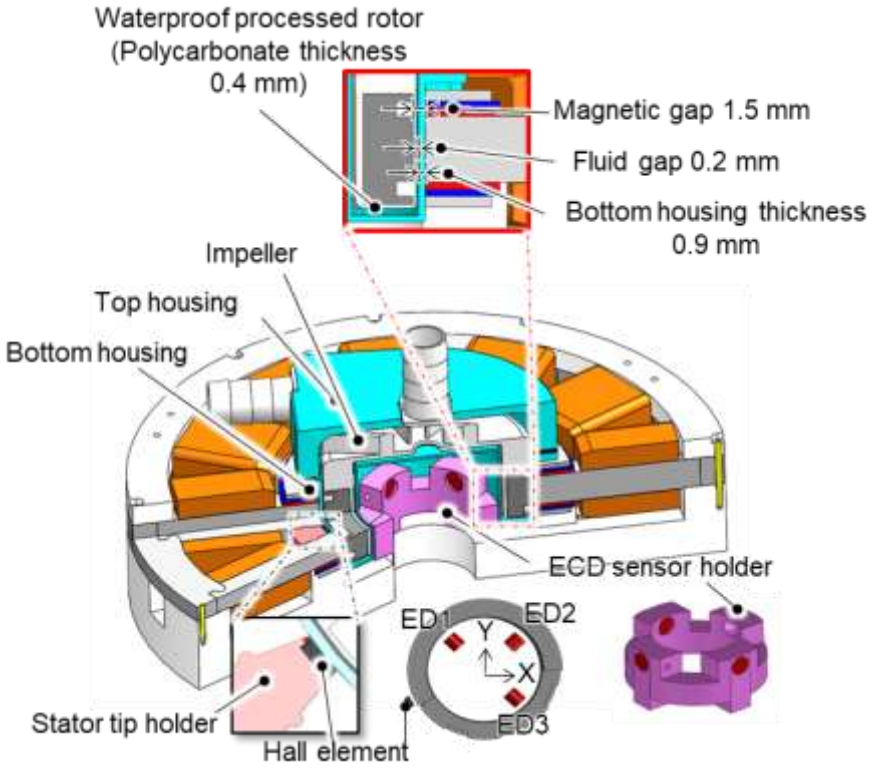


Figure 3.2 Schematic depiction of the mechanical structure of the CBP utilizing the proposed BELSM.

To measure the radial displacement of the rotor, three eddy current displacement (ECD) sensors are used. The ECD sensors are installed inside the rotor and the rotor is not required to add the additional sensor target. The sensor holder is made of polyetherimide to prevent interference with the sensor output and to avoid affecting the magnetic circuit in the BELSM. To facilitate the arrangement of the concentrated winding coils, twelve teeth of the stator are split with the back yoke. Polyetherimide holders are placed between the teeth to align the tips of the teeth. A Hall element (HE) is affixed in the groove of the stator tip holder, with its center aligned with the center of the rotor teeth. Its function is to detect variations in magnetic flux density across the HE caused by passing the rotor teeth, enabling the measurement of rotational speed and rotor angle. The overall height of the BELSM, with the disposable pump head, is 49.7 mm and the outer diameter of the BELSM is 144 mm, as shown in Fig. 3.1 (b).

## 3.3 Disposable pump head

Figures 3.3 (a) and (b) display a photograph and a cross-sectional view of the disposable pump head. This component consists of a top housing, a bottom housing, and an integrated impeller/rotor. The top and bottom housing, made from polyetherimide, are jointed using screws and sealed with a 1mm thickness rubber shim. The top housing is drilled to establish

connections for the inlet and outlet, each with inner diameters of 9 mm. The bottom housing is recessed in the middle from the bottom surface to accommodate the installation of the ECD sensor holder, as shown in Fig. 3.2, for radial displacement measurements.

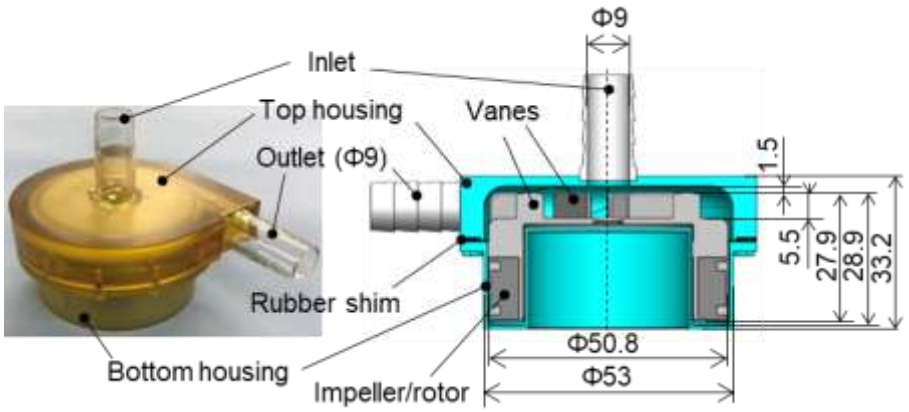


Figure 3.3 Disposable pump head: (a) Photograph; (b) Cross-section view.

The integrated impeller/rotor combines an iron rotor and a polycarbonate impeller. To prevent fluid resistance and rust, the surface and the slots of the rotor are molded with resin. A mixture of epoxy resin and curing agent (Z-1 low viscosity epoxy resin, NISSIN RESIN Co., Ltd, Japan) is prepared at a mass ratio of 2:1. The mixed liquid undergoes degassing in a vacuum chamber connected to a rotary vacuum pump (G-505, ULVAC). The rotor, previously degreased with ethanol, is immersed in the mixture and then inserted into a grooved polycarbonate base material, as depicted in Fig. 3.4 (a). Then, the defoamed mixture is poured into the base material, as illustrated in Fig. 3.4 (b), followed by another round of degassing. After exposing it to the atmosphere and leaving it for at least 36 hours to ensure complete hardening, the waterproof integrated impeller/rotor is machined to its final structure, as shown in Fig. 3.4 (c). Figures 3.5 (a) and (b) show the photograph of the iron rotor and integrated waterproof impeller/rotor, respectively.

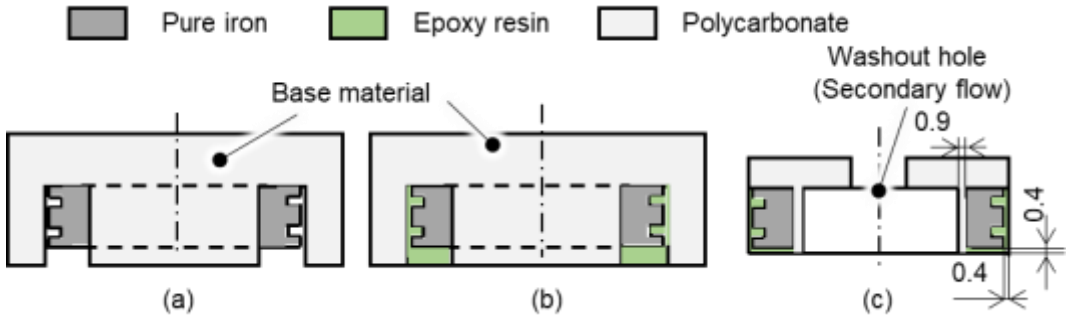


Figure 3.4 Fabrication process of the waterproof impeller/rotor: (1) Insertion of the rotor into base material; (2) Pour of the mixture into the base material; (c) Processing of impeller/rotor for the final shape.

To reduce the height of the impeller vanes and the contact area between vanes and blood, a flat semi-open impeller design with six straight blades of 5.5 mm is employed. This design can improve the pump efficiency compared with the open impeller, decrease the initial priming volume of the pump head, and enhance biocompatibility compared to the closed impeller [99-100]. Furthermore, a washout hole of Φ6 mm is machined in the middle of the impeller to facilitate secondary flow and prevent blood stagnation. [101-102]. The mass of the integrated impeller/rotor is 0.088 kg. The diameter and height of the integrated impeller/rotor are 50.8 mm and 27.9 mm, respectively.

Figure 3.5 (a) Photograph of the iron rotor; (b) Photograph of the integrated waterproof impeller/rotor.

When the impeller/rotor is suspended at the geometric center, the upper, lower, and lateral fluid gaps between the rotor and the pump housing are 1.5 mm, 1 mm, and 0.2 mm, respectively, as illustrated in Fig. 3.3 (b). The initial priming volume of the disposable pump head is 20 mL, smaller than the 31 mL initial filling volume of CentriMag [103].

## 3.4. Electrical system

The electrical system comprises sensor and power systems. The compact slice structure of the BELSM poses challenges in sensor target design and the sensor placement configuration. Various types of power amplifiers are also explored to improve the rotational torque. The following section will discuss the model type and configurations of the sensors and amplifiers, respectively.

### 3.4.1 Radial displacement measurement sensors and calibration

The radial displacement of the rotor must be measured with high accuracy and high bandwidth from outside the pump housing, through the blood, so that the sensor does not come into contact with the blood. To measure displacement in the presence of bubbles or blood clots,

optical sensors are difficult to use, and eddy current sensors are the first candidates. However, due to the specific configuration of the BELSM, the rotor is thin and features salient poles on its periphery, and the compact stator coil structure occupies space. Therefore, the placement of ECD sensors is constrained to the interior of the rotor.

As shown in Fig. 3.2, three eddy current displacement sensors (PU-05A, AEC Corp, Japan) were positioned in the sensor holder at angles of ±45° and 135° relative to the X-axis. These sensor probes exhibit a 5 mm diameter, a linear measurement range of 0-2 mm, and a resolution of 0.3 μm. Consequently, the displacement of the rotor in the X and Y directions is determined through equations Eqs. (3.1) and (3.2) as follows:

$$x = \frac{V_{ED2} - V_{ED1}}{\sqrt{2}} \tag{3.1}$$

$$y = \frac{V_{ED2} - V_{ED3}}{\sqrt{2}} \tag{3.2}$$

where $V_{ED1}$, $V_{ED2}$, and $V_{ED3}$, are the output signals of the three ECD displacement sensors. The differential placement of sensors alleviates temperature drift and common-mode noise.

For precise measurements, sensor calibration is needed before each experiment. A sinusoidal currents are applied through the coil winding in the X- and Y-direction to make the rotor move slowly following the wall of the bottom pump housing. The calibration coefficients are adjusted so that the measured radial displacements form a circular orbit with a 200 μm radius equal to the fluid gap.

### 3.4.2 Rotor angle and speed measurement sensor

Precise rotor angle measurement is crucial for accurate phase current commutation in BELSM to enhance rotational torque in the closed-loop control. A HE (HW-322B, AKM Corp., Japan) was first mounted between the XpW and XpV phase stator poles, as depicted in Fig. 3.2, to detect the variations in magnetic flux alter the HE's output, facilitating the rotation speed and rotor angle measurement.

However, due to the installation position of the HE, a portion of the leakage magnetic flux generated by the phase current passes through the HE, as shown in Fig. 3.6, distorting the HE output. At high rotational speed, the distortion of the HE output is more obvious due to the increase in leakage flux with the motor current amplitude, as depicted in Figs. 3.7 (a) and (b). Since the frequency of phase current commutation is the same as the frequency of the HE voltage variation due to the rotor teeth, The tracking filters whose center frequency is the

electrical frequency cannot filter out this interference, making the signal processing very difficult.

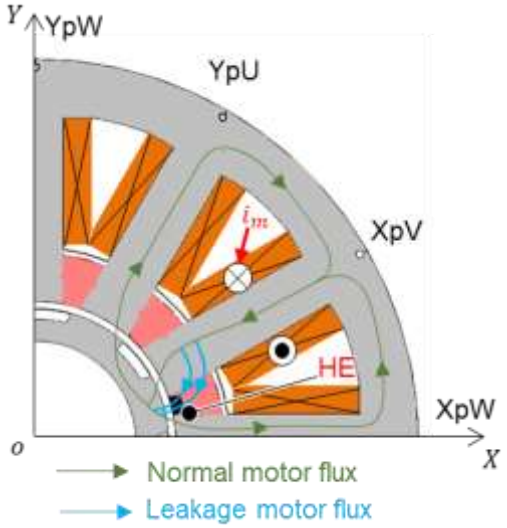


Figure 3.6 Schematic diagram of the leakage motor flux to distort the output of the HE.

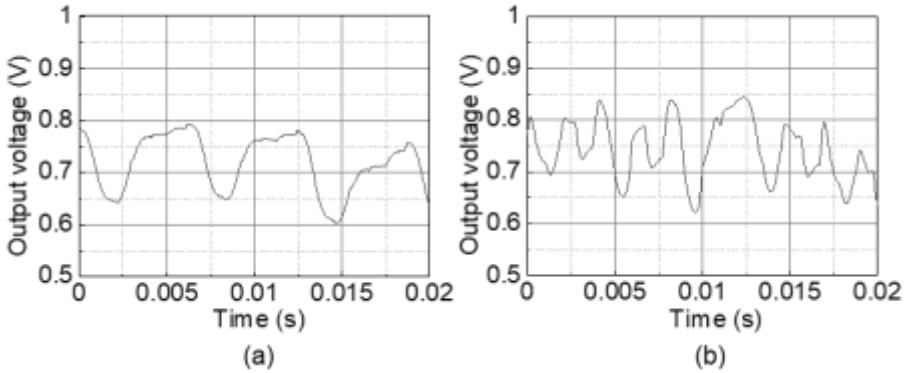


Figure 3.7 Measured output voltage of HE with open-loop rotation: (a) 1200 rpm with the amplitude of 0.4 A; (b) 1800 rpm with the amplitude of 0.8 A.

To remove the electromagnetic interference, a magnetic circuit model is proposed to restore the HE output by calculating the HE output without the effect of the leakage flux. However, the magnetic circuit model is not accurate with a large motor current amplitude at a higher rotational speed. The mechanical error is 4° at 1100 rpm, proving challenging to implement at a higher rotational speed.

To solve the distortion problem, a low-sensitivity HE (HG-372A, AKM Corp., Japan) was used. Compared with the previous HE model, this low-sensitivity HE exhibits a minor output voltage change when magnetic flux density is altered. Two models of HE are positioned symmetrically on the rotor. Figures 3.8 (a) and (b) present the raw voltage from the two models of HEs and the filtered output voltage after the tracking filter, whose central frequency equals electrical frequency, at a speed of 1400 rpm, respectively. Despite increased noise, the

distortion in the voltage waveform is reduced. After passing the tracking filter, the sinusoidal waveform of the filtered voltage from low-sensitivity HE has a more stable period and amplitude, facilitating subsequent signal processing. The detailed signal processing procedures will be discussed in Section 3.5.1.2.

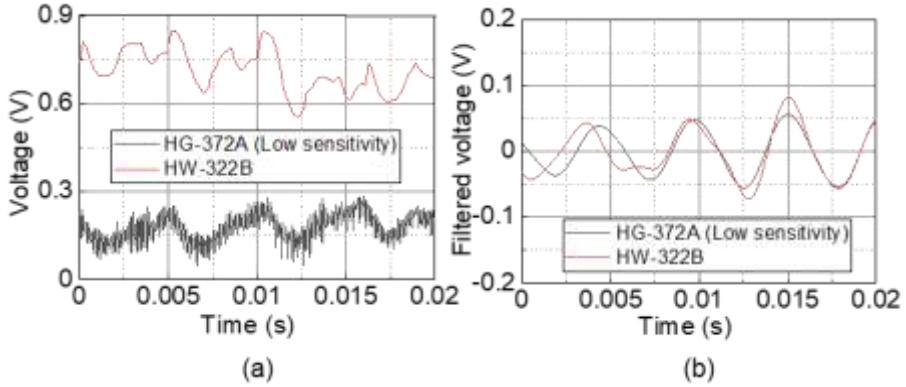


Figure 3.8 (a) Measured raw output voltage of HE at a speed of 1400 rpm utilizing two models of HE; (b) Measured filtered voltage of HE at a speed of 1400 rpm utilizing two models of HE.

### 3.4.3 Power system

In the proposed BELSM, the average resistance and inductance of the coil wire, featuring a diameter of 0.55 mm., is 2.22 Ω and 27.7 mH, respectively. To supply power to the twelve concentrated windings of the proposed BELSM, both linear amplifiers and Pulse Width Modulation (PWM) amplifiers have been tried. Linear amplifiers operate on the principle of amplifying signals continuously and proportionally, preserving the integrity of the input waveform with high linearity and minimal distortion. Though linear amplifiers excel in signal fidelity, their efficiency is comparatively lower, leading to increased heat dissipation and bulkier designs [104]. On the other hand, PWM amplifiers modulate the width of pulses to encode information. This method allows for higher efficiency, reduced heat generation, and a more compact design. However, the discrete nature of pulses introduces nonlinearity and potential electromagnetic interference [105]. In this section, the outcomes of employing these two amplifiers in the proposed BELSM will be discussed.

#### *3.4.3.1 Linear power amplifiers*

Twelve linear power amplifiers (PA04, Apex Microtechnology, Inc., USA) and twelve Hall-effect sensors (LA25-NP, LEM Corp.) were used to deliver and measure the current in each concentrated winding, respectively. Due to temperature constraints, the maximum supply voltage of the linear power amplifiers is ±60 V for safety. Independent current measurement in

each combined winding was achieved using twelve Hall-effect current sensors (LA25-NP, LEM Corp.).

Figure 3.9 shows the block diagram of the current controller. The PI controller was used with proportional and integral gain values set at 160 V/A and 800 V/A·s, respectively. The bode diagram of the current closed-loop feedback system, measured during magnetic levitation, is presented in Fig. 3.10. Notably, the amplitude of the reference current is 0.05 A, and the bandwidth of the current closed-loop feedback system ($I_{out}/I_{ref}$) is approximately limited below 780 Hz due to the voltage saturation.

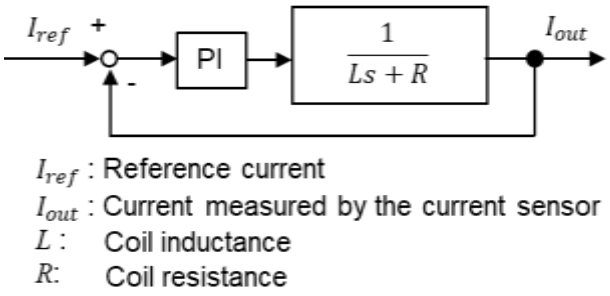


Figure 3.9 Block diagram of the current controller.

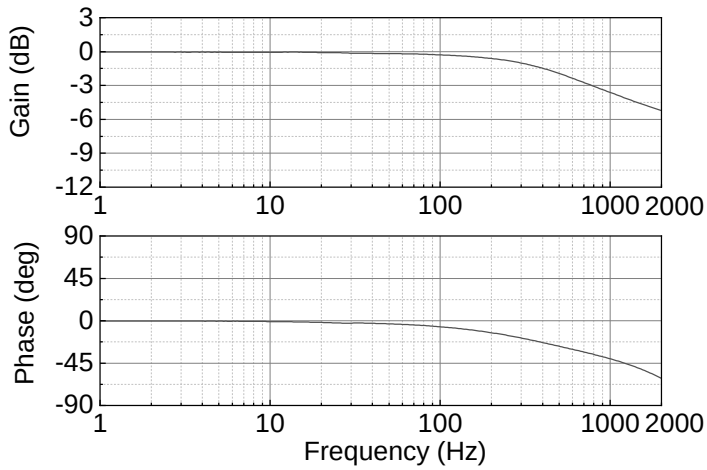


Figure 3.10 Measured bode diagram of the current closed-loop feedback system $I_{out}/I_{ref}$.

*3.4.3.2 PWM amplifiers*

To further increase the output voltage from the power amplifier and improve the current-loop bandwidth, PWM amplifiers are used for current transmission. Twelve PWM current amplifiers (JSP-090-10, Junus, USA) with a carrier frequency of 20 kHz were employed. The supply voltage of the PWM amplifiers is set at 100 V. This amplifier integrates a current controller, allowing us to adjust the bandwidth through an automatic parameter tune.

Consequently, by designing the controller and adjusting the parameters, the bandwidth of the current loop reached 1200 Hz with a current excitation amplitude of 0.1 A.

However, the PWM amplifier introduces electromagnetic noise, reducing the measurement accuracy of the sensor, especially the HE. Figures 3.11(a) and (b) depict the raw and filtered output voltage of the HE using the PWM amplifiers at a speed of 2200 rpm and the FFT result of the raw output voltage of the HE. The raw output voltage signal is distorted, and the filtered sinusoidal signal appears irregular and challenging to process. The FFT results reveal noticeable noise across the entire frequency domain. The difficulty in accurately measuring the rotor angle can lead to the failure of proper commutation of phase current during rotation feedback, resulting in rotation failure. Ultimately, the linear amplifiers were chosen to ensure rotation system stability and accuracy.

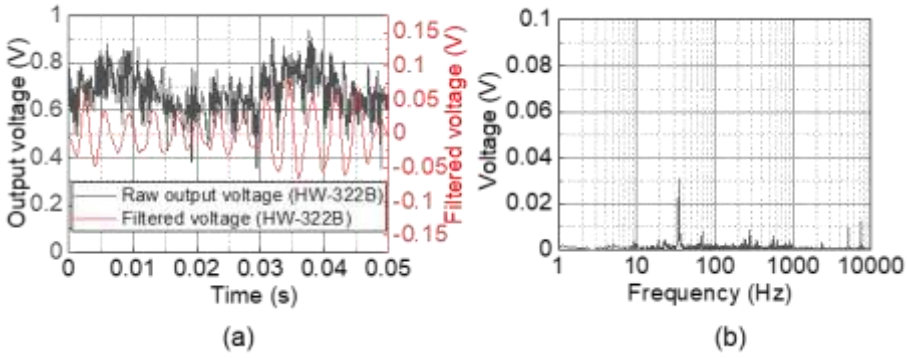


Figure 3.11 (a) Measured raw output voltage and filtered voltage utilizing the PWM amplifiers at a speed of 2200 rpm; (b) FFT result of the measured raw output voltage utilizing the PWM amplifiers at a speed of 2200 rpm.

## 3.5. Controller system

A DSP (MicroLabBox, dSPACE, GmbH.) is employed to calculate current reference commands to the twelve coil windings via the twelve linear power amplifiers. The suspension and rotation control algorism were implemented into the DSP system with a sampling frequency of 20 kHz. Both analog input and output operate on 16-bit channels, with voltage ranges set at ±10 V for both input and output. Figure 3.12 illustrates the schematic diagram of the control systems of the BELSM, consisting of the rotation control system and suspension control system. The variables in Fig. 3.12 will be explained in the next section.

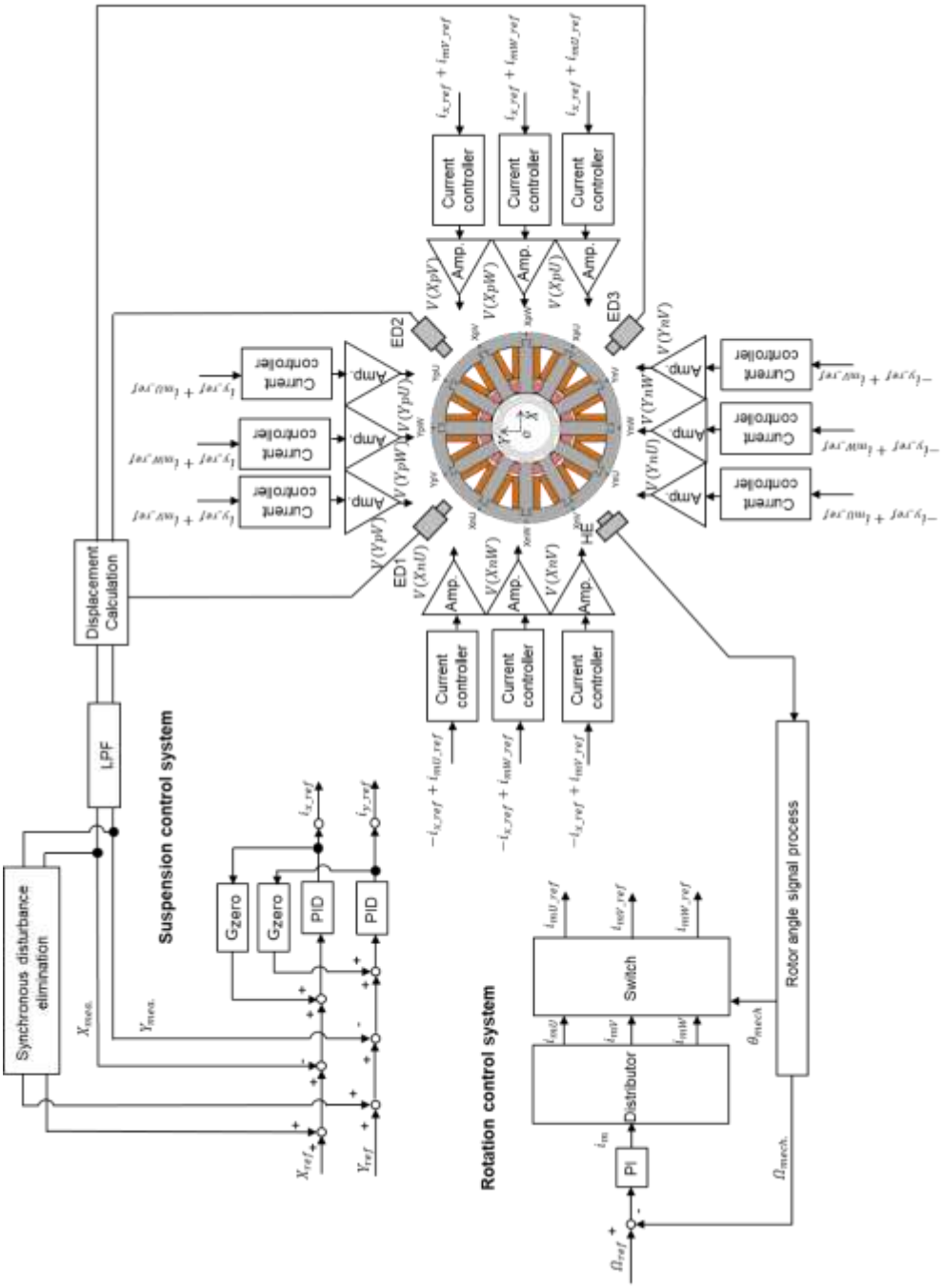


Figure 3.12 Schematic diagram of the entire control system.

### 3.5.1 Rotation control system

#### *3.5.1.1 Overall structure of the rotation control system*

In the rotation control, closed-loop feedback control is implemented to enhance rotational torque via the rotor angle measurement and phase current commutation, as depicted in Fig. 3.13. Utilizing a PI controller, detailed in Table 3.1, the amplitude of the reference current $i_m$ is calculated. The electrical angle is computed from the raw output voltage of HE, which is for the rotational signal process. Three phases, U, V, and W are energized at different electrical

angles to generate reference rectangular wave currents ($i_{mU\_ref}$, $i_{mV\_ref}$, $i_{mW\_ref}$). Employing the dual-phase excitation method, which has been introduced in Chapter 2, the current excitation period for each phase coil is set to 22.5°, determined via trial experiments to achieve the rotational torque with minimum current amplitude.

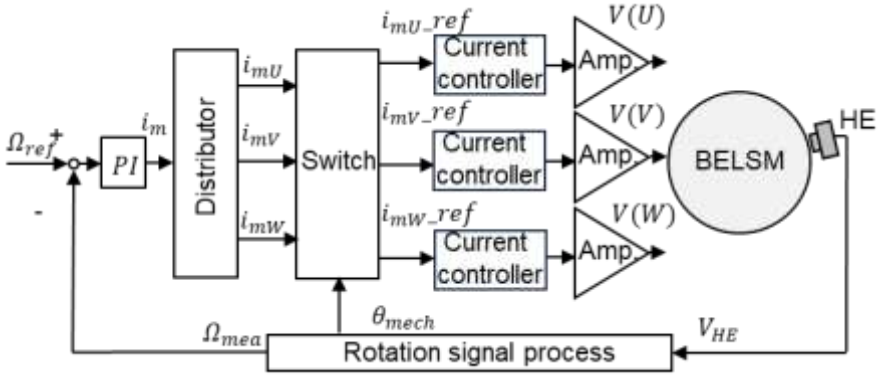


Figure 3.13 Block diagram of the rotation control system.

Table 3.1 Speed feedback control parameter

| Parameters | Rotation control system |
|---|---|
| Proportional gain $K_p$ | 0.005 A/rpm |
| Integral gain $K_i$ | 0.001 A/rpm·s |

*3.5.1.2 Rotation signal process*

The raw output voltages distorted by interference from the phase current can result in a significant error in rotor angle measurement, culminating in rotation failure. A rotation signal process method is employed to ensure rotational stability and improve the rotational torque, as depicted in Fig. 3.14. Rather than utilizing the time response of output voltage waveform from HE for rotor angle calculation, the rotor angle information was reconstructed using more precise measurement time points.

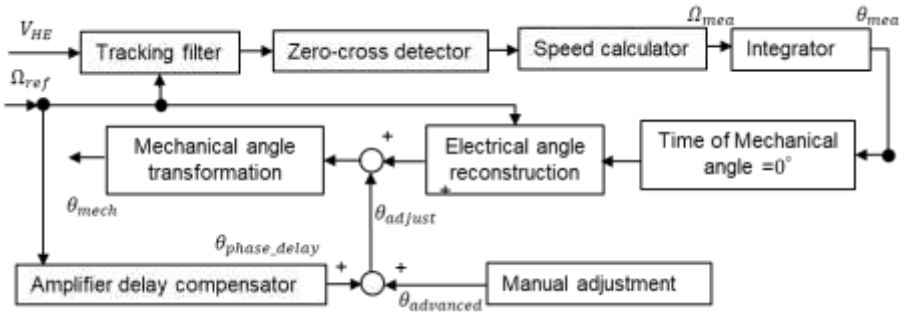


Figure 3.14 Block diagram of the rotational signal process.

The raw output voltage of the HE is filtered through a tracking filter to remove noise at other frequencies. Given that the peaks and troughs of raw output voltage from HE are prone to noticeable distortion, the rotational speed is determined based on the count of the pulse signal at zero-crossing points of the filtered signal. The integration of rotational speed yields the electrical rotor angle. Sinusoidal transformation of the electrical angle identifies the 0° position, where the W-phase stator pole aligns with the rotor teeth. The electrical angle is then constructed using the reference velocity based on the 0° position.

The amplifier phase delay compensator $\theta_{phase\_delay}$ and the advanced angle setting $\theta_{advanced}$ are introduced to enhance rotational torque, as illustrated in Fig. 3.14. The $\theta_{phase\_delay}$ is employed to offset the phase delay in the current loop feedback ($I_{out}/I_{ref}$), as depicted in Fig. 3.10. A cubic function is employed to fit the measured phase bode plot, determining $\theta_{phase\_delay}$ at various rotational speeds. The $\theta_{advanced}$ is used to reduce the impact of current response delays dependent on the rotational speed, which is experimentally turned to ensure the minimal current amplitude at each rotational speed. The adjustment angle $\theta_{adjust}$, which is the sum of $\theta_{phase\_delay}$ and $\theta_{advanced}$, is subtracted from the energized electrical angle of each phase. Table 3.2 shows the phase commutation of the mechanical angle of each phase.

Table 3.2 Phase commutation of the mechanical angle for U, V, and W phases

| Motor phase | | *U* phase | *V* phase | *W* phase |
|---|---|---|---|---|
| Energized mechanical angle (°) | On | -7.5-$\theta_{adjust}$ | 7.5-$\theta_{adjust}$ | 22.5-$\theta_{adjust}$ |
| | Off | 15-$\theta_{adjust}$ | 30-$\theta_{adjust}$ | 45-$\theta_{adjust}$ |

## 3.5.2 Suspension control system

### *3.5.2.1 Overall structure of the suspension control system*

A proportional-integral-derivative (PID) controller is employed for radial displacement feedback in the suspension control system, as shown in Fig. 3. 15. A 1st-order low pass filter (LPF) with a cut-off frequency $f_{l1}$ is introduced to the derivative part of the PID controller to limit the high-frequency gain. To mitigate high-frequency noise, a 2nd-order LPF with damping ratio $\xi$ and cut-off frequency $f_{l2}$ is applied to the output of the ECD sensor for radial displacement measurement. The simulation and experiments tune the control parameters, as detailed in Table 3.3.

A zero-power controller ($G_{zero}$) determines the magnetic center during levitation to reduce power consumption. However, it is not utilized in the later rotation experiment due to the combined windings. Instead, the determined magnetic center for the rotation experiment is

defined by the reference radial position that minimizes the levitation power consumption. This controller consists of an integral operator with a gain of 0.001 m/A·s.

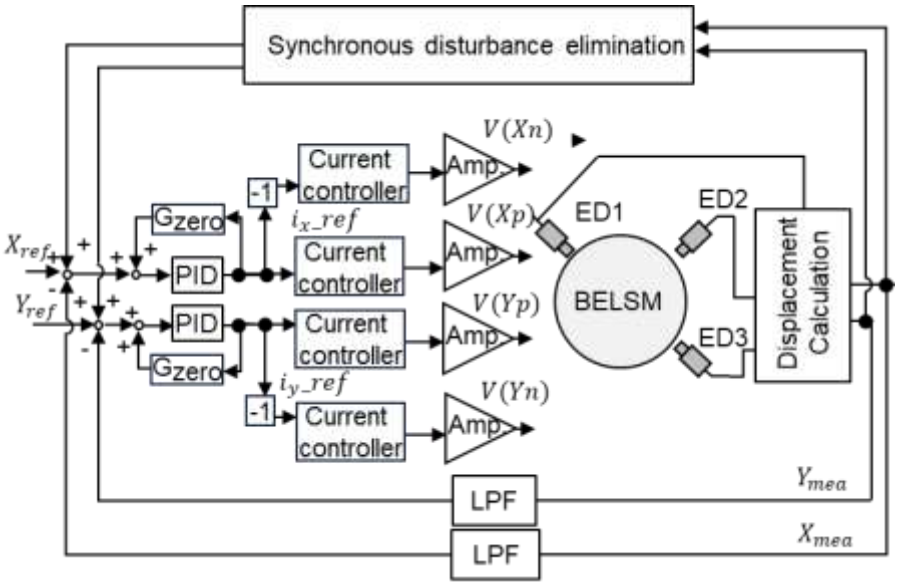


Figure 3.15 Block diagram of the suspension control system.

Table 3.3 Displacement feedback control parameter

| Parameters | Suspension control system |
|---|---|
| Proportional gain $K_p$ | 4300 A/m |
| Integral gain $K_i$ | 20000 A/m·s |
| Derivative gain $K_d$ | 7A·s /m |
| Cut-off frequency of the first-order LPF $f_{l1}$ | 500 Hz |
| Cut-off frequency of the second-order LPF $f_{l2}$ | 140 Hz |
| Damping ratio of the second-order LPF $\xi$ | 1 |

*3.5.2.2 Synchronous disturbance elimination*

To mitigate the risk of excessively small fluid gaps leading to severe blood clots, the rotation accuracy needs to be improved, diminishing the amplitude of the unbalanced vibration. Despite persistent efforts using experiments and simulation, achieving a further reduction in vibration amplitude solely through a PID controller has been proven challenging. Consequently, the synchronous disturbance elimination method is explored [106] to suppress unbalanced vibration. Figure 3. 16 illustrates the block diagram of the synchronous disturbance elimination method. The $X_d$ and $Y_d$ can be obtained from the measured radial displacements $X_{mea}$ and $Y_{mea}$

through coordinate transformation, which includes the DC component of unbalanced vibration. An LPF with a cut-off frequency of 2Hz is used to detect only this DC component. Through multiplication with gain, the sinusoidal displacement with a 180° phase shift, effectively counteracting unbalanced vibrations. Compared with the repetitive control [107], this method is simple while limited to eliminating disturbance at a specific known frequency.

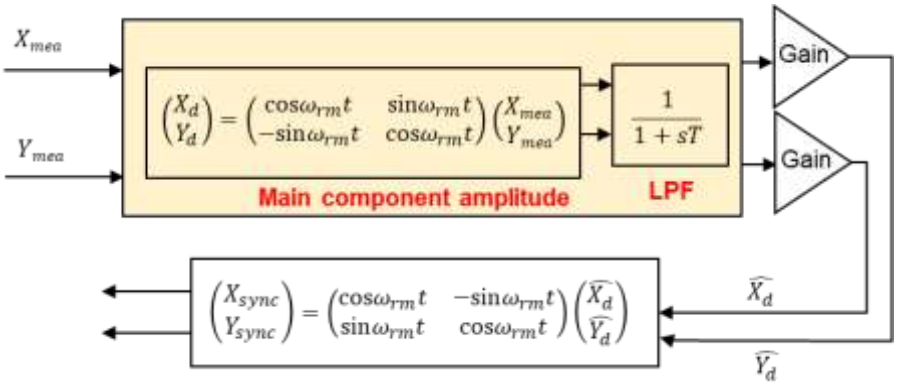


Figure 3.16 Block diagram of the synchronous disturbance elimination method.

## 3.6. Summary

This chapter provides an overview of the comprehensive mechanical structure of CBP, encompassing the proposed BELSM, disposable pump head, electrical system, and controller system. Leveraging the earlier simulation model, the proposed BELSM was processed and assembled. To facilitate performance evaluation, a disposable pump head with an initial priming volume of 20 mL was fabricated. The BELSM size has not been fully optimized yet, leaving room for further miniaturization. The slot fill factor for this BELSM is currently only 46.4%, while conventional motors can achieve 70-75% due to heat dissipation needs. Redesigning the coil parameters and arrangement can further reduce the size of the BELSM.

For the sensor system, the three ECD sensors were used within the rotor to measure radial displacement. Additionally, two different HE models are employed to measure the rotor angle, with the low-sensitivity HE sensor effectively mitigating distortion caused by large phase currents. For the power system, two types of power amplifiers are utilized. Compared to PWM amplifiers, linear power amplifiers prevent high-frequency noise in the sensor signal, ensuring accuracy in rotor angle measurement. However, heat dissipation concerns limit their usage. The relatively lower supply voltage leads to a low current-loop bandwidth.

Furthermore, the control system is integrated into the DSP, encompassing rotation and suspension control. In the rotation control, a PI controller is utilized for the speed feedback system, with the rotation signal processing designed to rectify angle measurement inaccuracies.

In the suspension system, PID control is used for the displacement feedback system, accompanied by a synchronous disturbance elimination method to counter unbalanced vibrations.

Chapter 4 will employ the constructed CBP system for performance evaluation and discuss the performance improvement method. Furthermore, as ECD sensor placement results in a small fluid gap for secondary flow, potentially impacting hemolysis and thrombolysis, a new radial measurement method will be proposed in Chapter 5 to address this issue.

# Chapter 4 Performance evaluation

## 4.1 Introduction

Chapter 3 discussed the prototype of the CBP and its control system. This chapter discusses the magnetic suspension and rotational performances of the proposed BELSM in the mock circulatory loop. Furthermore, the H-Q curve and power consumption of the CBP were also measured. However, the CBP fell short of achieving the targeted flow rate and head pressure. Consequently, the reasons and the potential solutions for enhancing hydraulic performance are discussed.

## 4.2 Experimental setup

Figures 4.1 (a) and (b) show the photograph and schematic diagram of the mock circulatory loop, respectively. The mock circulatory loop comprises the prototype CBP, two pressure gauges (GP-M001, KEYENCE; KL-76, Naganokeiki) positioned at the inlet and outlet of the disposable pump head, an ultrasonic flowmeter (TS410, Transonic Systems, Inc.), a reservoir tank, and a fluid resistance-regulating clamp. A mock circulatory loop filled with 40wt% aqueous glycerol was constructed. This solution's viscosity is 3.63 mPa·s at 20 ℃ within the blood viscosity at 37 ℃.

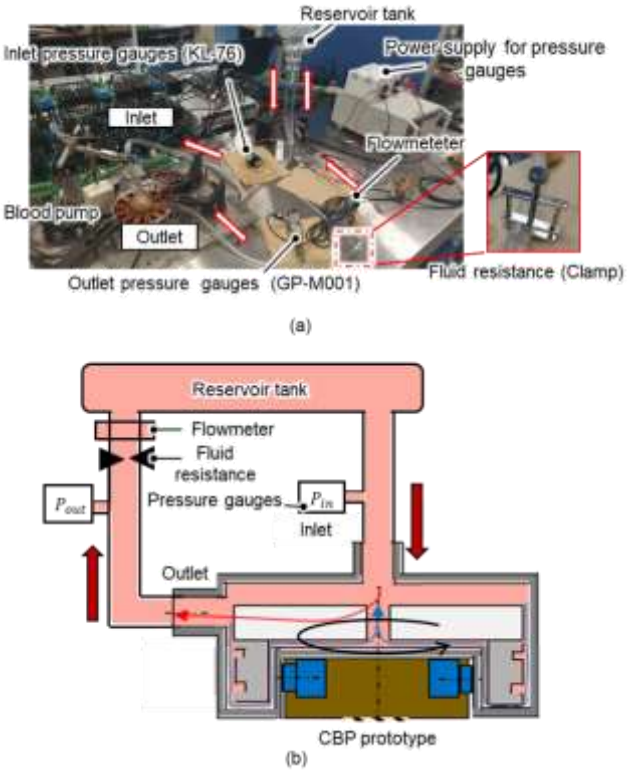


Figure 4.1 (a) Photograph of the mock circulatory loop for performance evaluation; (b) Schematic diagram of the mock circulatory loop for performance evaluation.

## 4.3 BELSM performance evaluation

### 4.3.1 Suspension performance evaluation

#### *4.3.1.1 Levitation startup*

A magnetic levitation startup experiment was conducted with the outlet fully clamped. The impeller/roter moves out of the electromagnetic contact with the wall of the pump housing and is positioned in the center of the pump housing, as illustrated in Figs 4.2 (a) and (b). The positioning accuracy at 0 rpm in the X and Y directions are 14.5 μm and 10.5 μm, respectively. The radial displacement exhibits oscillation around the origin point with a small amplitude, larger than the sensor noise. The reason for residual oscillation is that a larger differential gain cannot be used to ensure the system stability and reduce the high-frequency noise. Figures. 4.3 (a) and (b) depict the current and voltage waveform of a set of opposing coils XnW and XpW at the startup. During startup, a maximum instantaneous current of 0.52 A and a voltage of 39 V are generated, far from reaching the voltage saturation of the linear power amplifier.

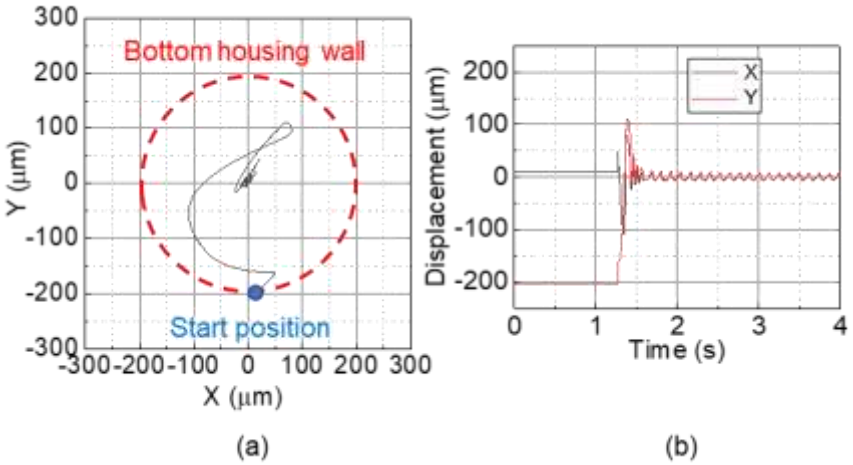


Figure 4.2 Magnetic levitation startup experiment without rotation: (a) Trajectory; (b) Radial displacement.

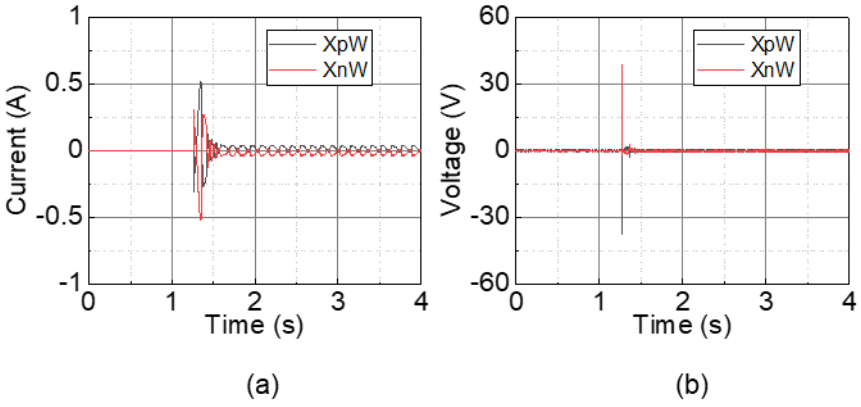


Figure 4.3 Magnetic levitation startup experiment without rotation: (a) Current; (b) Voltage.

*4.3.1.2 Frequency response in the radial direction*

The transfer function of the suspension system is measured by the FRA analyzer (FRA5022, NF Corp., Japan). Figure 4.4 illustrates the bode plot of the transfer function $X_{mea}/I_x$ from the measured current in the XpW coil to the measured radial displacement in the X-direction. This transfer function $X_{mea}/I_x$ can be derived from the radial motion equation of Eq. (4.1):

$$M\ddot{x} + C\dot{x} + K_s x = K_c I_x \tag{4.1}$$

where $M$ and $C$ represent the impeller/rotor mass plus additional mass [109] and the damping coefficient, respectively. $K_s$ and $K_c$ denote the negative stiffness in the radial direction and the current-force coefficient, respectively. After Laplace transformation, Eq. (4.2) can be obtained from Eq. (4.1) as follows:

$$\frac{x(s)}{I_x(s)} = \frac{K_c}{Ms^2+Cs+K_s} \tag{4.2}$$

The curve fitting is performed by adjusting the model parameters. Table 4.1 shows the identified model parameters. The identified model parameters can provide a radial motion model for designing the PID controller in displacement feedback control.

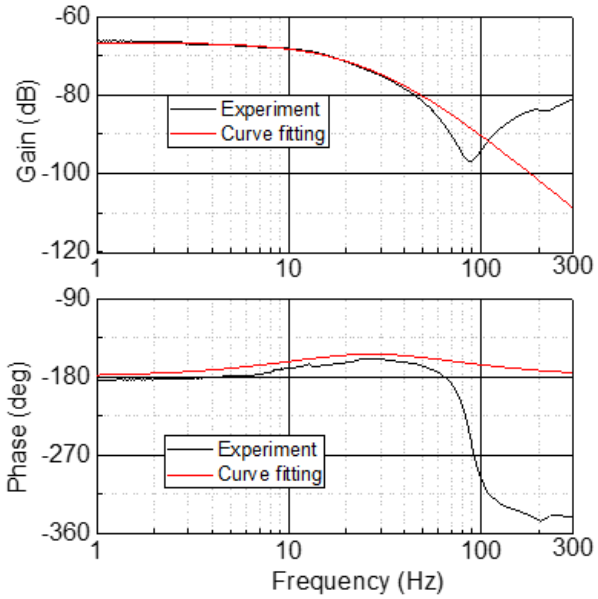


Figure 4.4 Measured bode diagrams of the transfer function $X_{mea}/I_x$.

Table 4.1 Identified and simulated model parameters in 40wt% aqueous glycerol solution

| | Identified model parameter | Simulated model parameter |
|---|---|---|
| $M$ | 1.8 kg | - |
| $C$ | 300 Nm/s | - |
| $K_s$ | -52 N/mm | -60.4 N/mm |
| $K_c$ | 24 N/A | 19.3 N/A |

Based on the radial motion model, the PID controller was first adjusted in the simulation and then tuned in the experiment. The goal is to attain a high bandwidth, maintain the gain in the low-frequency range close to 0 dB, and ensure a sufficient stability margin. Figure 4.5 shows the bode plot of the displacement closed-loop transfer function $X_{mea}/X_{ref}$ from the reference radial displacement to the measured radial displacement based on the tuned PID controller parameters, detailed in Chapter 4, in the X- and Y-directions. The amplitude of the reference displacement is 30 μm, and the bandwidth of the closed-loop feedback system is about 61 Hz.

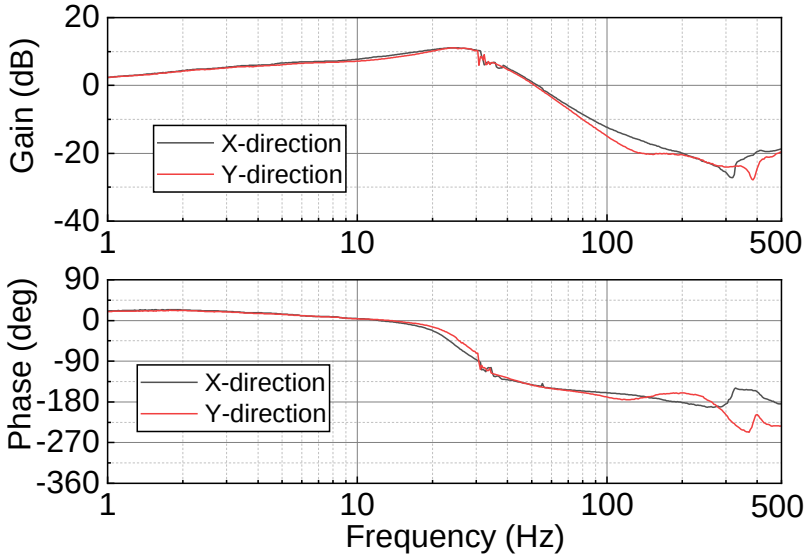


Figure 4.5 Measured bode diagrams of the displacement closed-loop feedback system $X_{mea}/ X_{ref}$.

### 4.3.2 Rotation performance evaluation

#### *4.3.2.1 Rotor angle measurement*

The measurement accuracy of the rotational angle is essential for improving the rotation performance. In Chapter 3, it was explained that owing to the placement of the HE, the raw HE output voltage is highly susceptible to interference from the magnetic flux generated by the motor current. A low-sensitivity HE was utilized to measure the rotor angle precisely. The

filtered HE output voltage, as shown in Fig. 4.6 (b), is derived from the raw HE one shown in Fig. 4 .6(a) at 1600 and 2400 rpm.

In Fig. 4.6 (b), two red lines are taken as a benchmark for the maximum peak and through of the filtered HE output voltage. Compared with 1600 rpm, the amplitude of the filtered HE output voltage undergoes a notable change at 2400 rpm, influenced by the magnetic flux from the motor current. The aforementioned rotation signal process method in Section 3.5.1.2 further reconstructs the rotor angle to mitigate the filtered HE output voltage distortion.

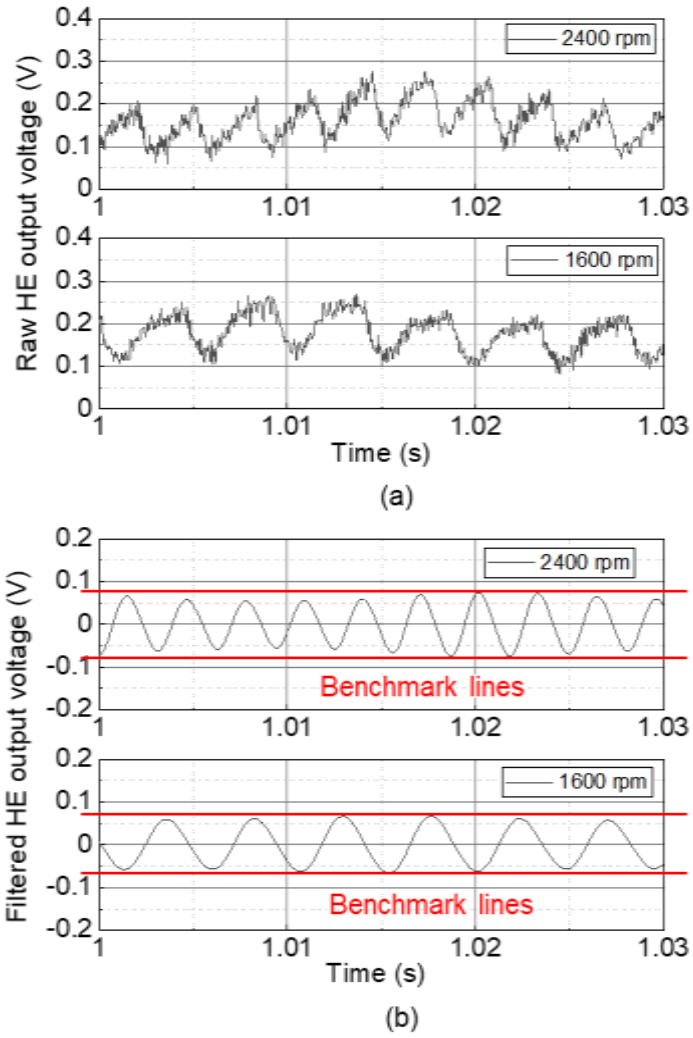


Figure 4.6 (a) Raw HE output voltage and (b) Filtered HE output voltage at different rotational speeds of 1600 rpm and 2400 rpm.

Figure 4.7 illustrates the calculated mechanical angle at different rotational speeds of 1600 and 2400 rpm. Within one electrical period, the difference between the calculated mechanical angle and the reference mechanical angle of 45° regarded as the measurement error. As shown in Fig. 4.7, although the rotor angle measurement error at 2400 rpm is approximately

1.1°, surpassing the error observed at 1600 rpm, which can achieve stable rotation at high rotational speed.

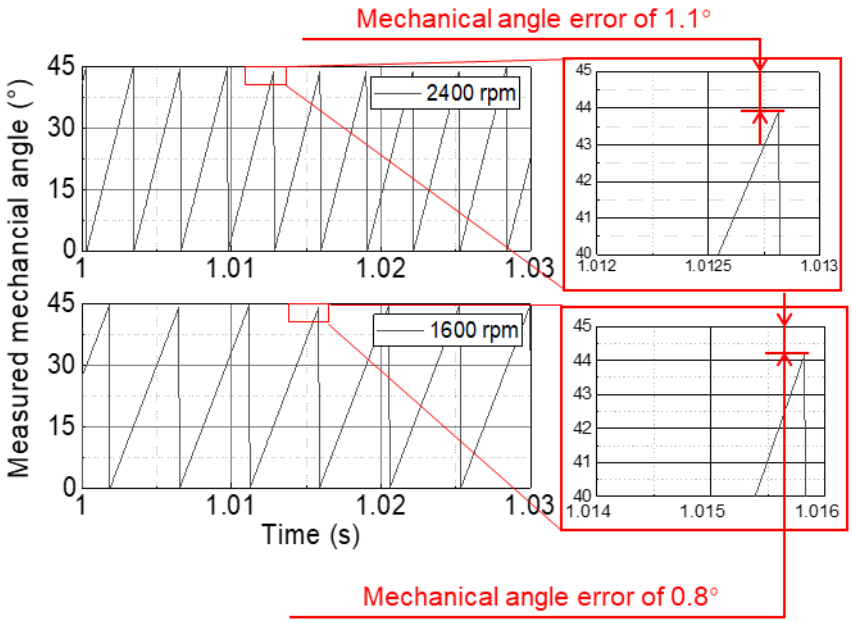


Figure 4.7 Measured mechanical angle at different rotational speeds of 1600 rpm and 2400 rpm utilizing the proposed rotation signal process method.

*4.3.2.2 Rotation accuracy*

Stable rotation ranging from 0 rpm to 2300 rpm in a 40wt% aqueous glycerol solution has been successfully achieved, with an outlet from fully clamped to fully opened. The synchronous disturbance elimination method is used to suppress the unbalanced vibration and to improve the rotation accuracy, as detailed in Chapter 3. Figure 4.8 shows the displacement and current before and after switching the synchronous disturbance elimination method at a speed of 2000 rpm. The gain of the synchronous disturbance elimination method is set to 0.4 to maintain suspension stability. It is evident that the displacement in X- and Y-directions is reduced. Simultaneously, the suspension current decreases, resulting in lower power consumption. This method makes the rotor rotate its principal axis of inertia, reducing the feedback radial force and winding current.

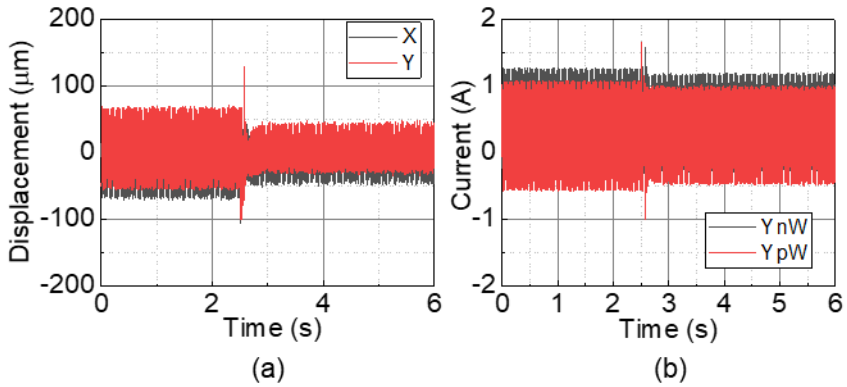


Figure 4.8 (a) Displacement in the X- and Y-directions and (b) Current in the YnW and YpW phases before and after switching the synchronous elimination disturbance method at a speed of 2000 rpm.

Figure 4.9 depicts the rotation accuracy of the impeller/rotor versus rotational speed at the maximum flow rate in the radial X- and Y- directions, spinning from 1600 rpm to 2300 rpm. The maximum displacements in the X- and Y-directions are less than 100 μm, ensuring no contact between the impeller/rotor and the bottom housing wall. Figures 4.10 (a), (b), and (c) illustrate the rotation trajectory of the impeller at a speed of 2300 rpm with varying flow rates. The maximum vibrational amplitude of the impeller/rotor trajectories remains under 100 μm even at the maximum flow rate. Considering the fluid gap is 200 μm, the vibrational amplitude remains below 50% when the rotor rotates at high flow rates and rotational speeds.

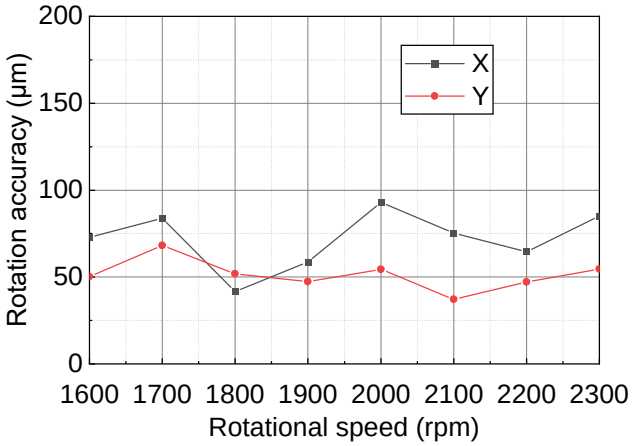


Figure 4.9 Measured rotational accuracy of the impeller/rotor versus rotational speed at each maximum flow rate in the X- and Y-directions.

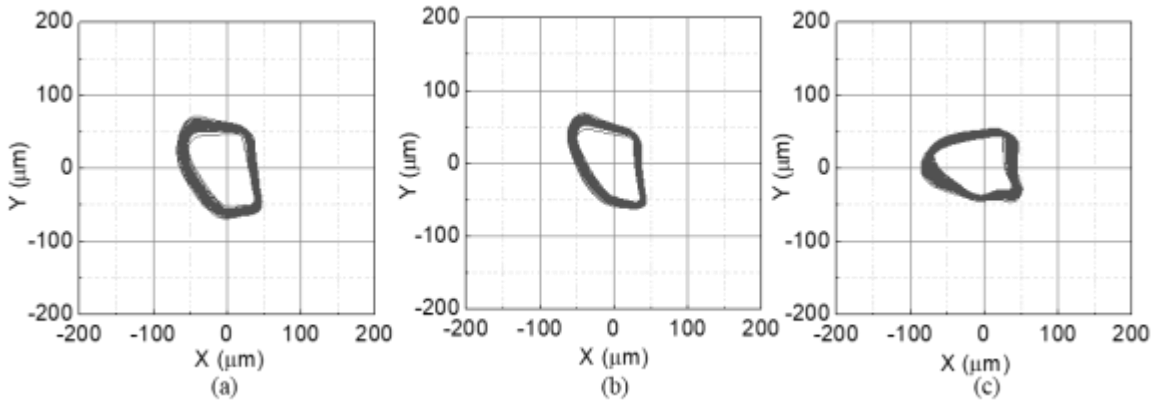


Figure 4.10 Measured rotation trajectory of the impeller/rotor at a speed of 2300 rpm with different flow rates: (a) 0 L/min; (b) 1.99 L/min; (c) 4.59 L/min.

## 4.4. Pump performance evaluation

In this section, the performance of the CBP utilizing the proposed BELSM will be assessed by measuring the H-Q curve, power consumption, and pump efficiency.

### 4.4.1 H-Q curve

Figure 4.11 illustrates the H-Q curves of the CBP utilizing the proposed BELSM across the range of 1600 rpm to 2400 rpm. The head pressure is the difference between the inlet and outlet pressures. The fluid resistance is adjusted by varying the clamp opening to change the flow rates. With increased rotational speed, both the achieved flow rate and head pressure gradually rise. The maximum head pressure and flow rate attained were 214.5 mmHg and 4.59 L/min at 2400 rpm and 2300 rpm, respectively.

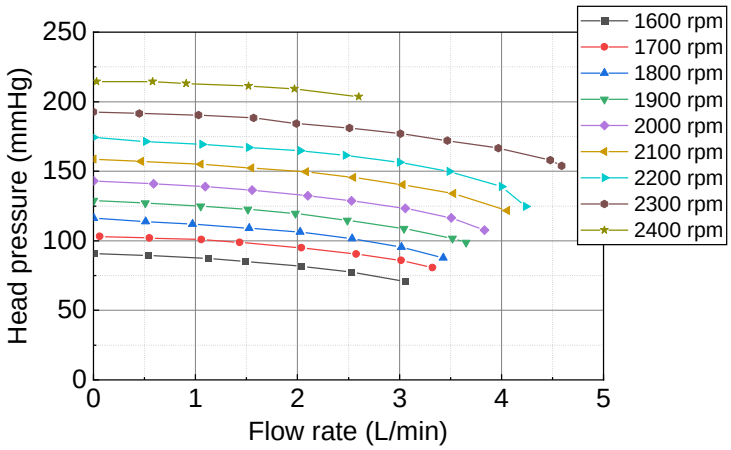


Figure 4.11 Measured H-Q curve with different rotational speeds.

4.4.2 Power consumption

The average power consumption $\overline{P}$ of the proposed BELSM was calculated using the following Eq. (4.3), which represents the mean of the product of twelve coil currents and terminal voltages over multiple rotation speeds. This calculation excludes the power consumption of the linear amplifiers, ECD displacement sensor system, and HE system.

$$\bar{P} = \frac{\sum_{c=1}^{12} V_c(N) I_c(N)}{N} \tag{4.3}$$

where $V_c$ ($N$) and $I_c$ ($N$) denote the transient twelve coil currents and voltages, respectively, measured in the discretized time domain by the current and voltage sensors. N represents the number of sampling points in the operational period.

The average power consumption at a speed of 0 rpm with the zero-power controller is 0.039 W, as shown in Fig. 4. 12. Figure 4. 13 shows the power consumption at different rotational speeds and flow rates, which is the sum of the power utilized for rotation and magnetic levitation. The power consumption rises gradually with the rotational speeds and flow rate increasing.

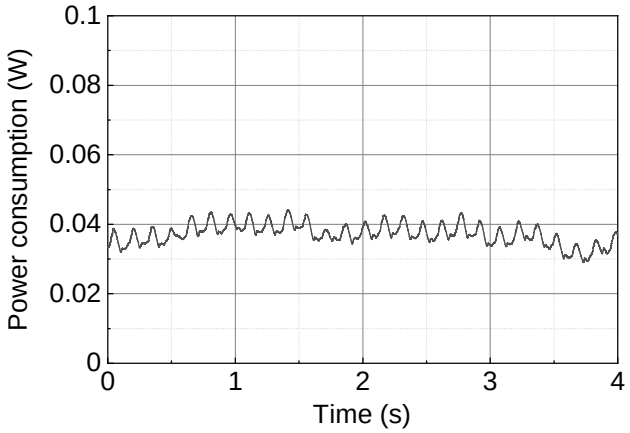


Figure 4.12 Measured power consumption at a speed of 0 rpm with a zero-power controller.

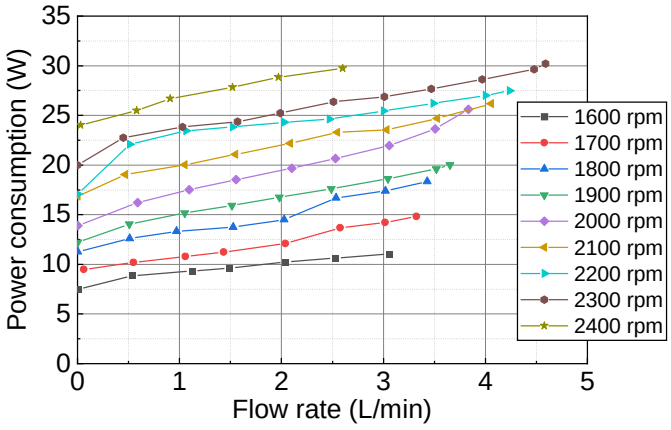


Figure 4.13 Measured power consumption at different rotational speeds and flow rates.

4.4.3 Pump efficiency

The pump efficiency $\eta$ is assessed based on the average power consumption in the H-Q curve, as per Eq. (4.4)

$$\eta = \frac{HQ}{\bar{P}} \tag{4.4}$$

where $H$ represents the head pressure of the CBP, calculated as the pressure difference between the inlet and outlet, and $Q$ is the flow rate measured by the flow rate sensor. $\bar{P}$ is the average power consumption mentioned in Section 4.4.2. The pump efficiency $\eta$ gradually increases, reaching its peak, as depicted in Fig. 4.14. In our experiment, the maximum pump efficiency reached 5.3% at a speed of 2300 rpm with a flow rate of 4.48 L/min.

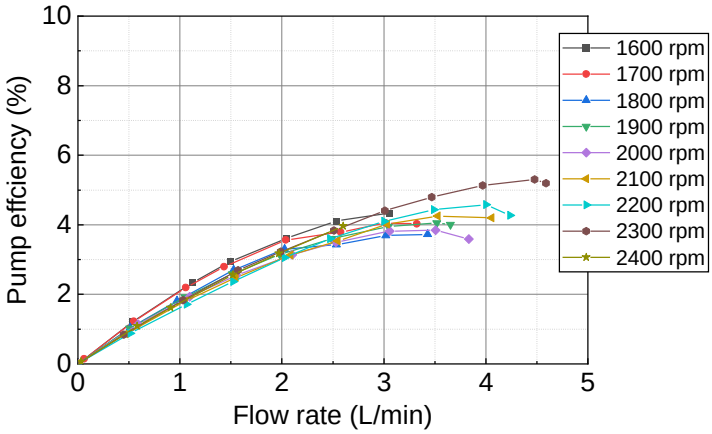


Figure 4.14 Calculated pump efficiency at different rotational speeds and flow rates.

## 4.5. Discussion

4.5.1 Reasons for not achieving target values

The CBP utilizing the proposed BELSM demonstrated hydraulic performance, yielding a maximum head pressure of 214.5 mmHg and a peak flow rate of 4.59 L/min while maintaining stable magnetic levitation. However, the CBP fell short of satisfying the hydraulic performance of an ECMO system due to rotational speed limitations. At high flow rates and rotational speeds, the impeller/rotor faced challenges in stable rotation, attributed to insufficient rotational torque and bearing stability. The primary factor contributing to this limitation is the relatively low current-loop bandwidth of 780 Hz, caused by insufficient output voltage ±60 V from the linear power amplifiers due to temperature limitations. As illustrated in Fig. 4.15, at a maximum speed of 2400 rpm and a flow rate of 2.60 L/min, the voltage exhibits noticeable saturation, indicating an inadequate supply to the linear power amplifiers. Since the current

utilized in each coil encompasses both levitation and rotation currents, directly measuring the voltage ratio for magnetic levitation and rotation is unfeasible. Through simulation, it can be roughly calculated that the proportion of voltage used for rotation exceeds 95%.

Figures 4.16 (a) and (b) further illustrate the relationships between the calculated mechanical angle, command reference current, and measured coil current at speeds of 1600 rpm and 2400 rpm without flow rates. The constrained current-loop bandwidth hinders precise tracking of command reference current at high rotational speeds, resulting in diminished rotational torque and levitation stability. Beyond the primary factors, it is essential to take into account the accuracy of rotor angle measurement. With the increases in rotational speed and current amplitude, the rotor angle error measured by the HE may also increase slightly.

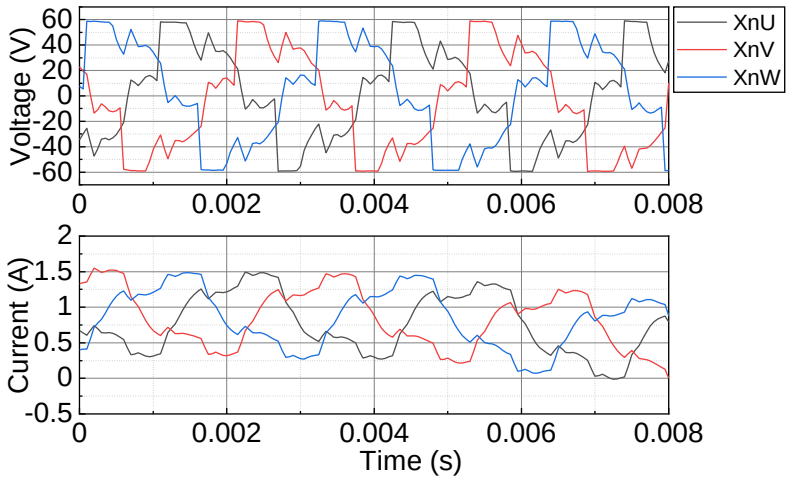


Figure 4.15 Measured voltage and current of the coil at a maximum speed of 2400 rpm with a maximum flow rate of 2.60 L/min.

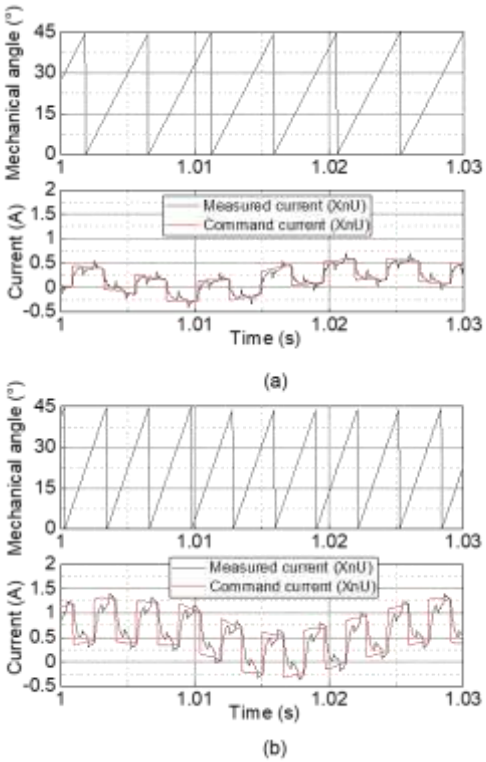


Figure 4.16 Relationship among the calculated mechanical angle, command current, and measured current: (a) 1600 rpm; (b) 2400 rpm.

## 4.5.2 Improvement of lower current-loop bandwidth

### *4.5.2.1 Reduction of power dissipation of the linear power amplifier by positive-negative phase current commutation method*

Figure 4.17 illustrates the simplifier linear power amplifier circuit. The output transistors $Q_1$ and $Q_2$ generate positive and negative output currents to the load, respectively. The temperature limit of the amplifier is determined by the heat dissipation of the output transistors. The previous phase current commutation method would concentrate the power consumption on the $Q_1$ energized positive current, reaching the temperature limit. However, the power consumption in $Q_2$ is minimal as shown in Fig. 4.18.

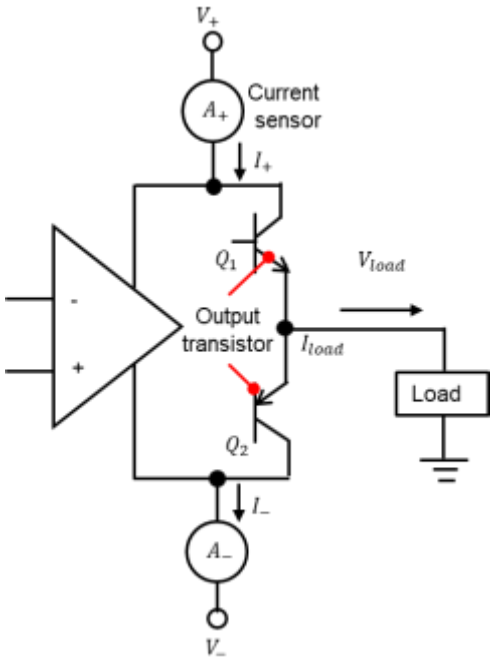


Figure 4.17 Simplified linear power amplifier circuits.

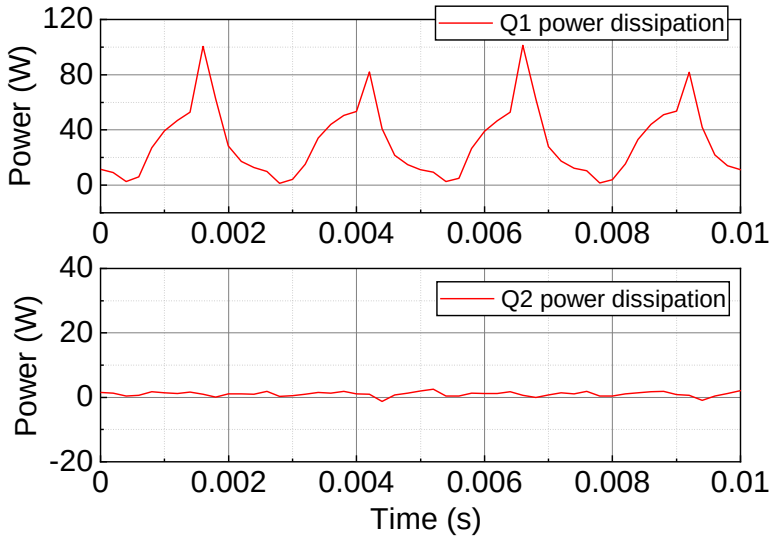


Figure 4.18 Measured $Q_1$ power dissipation and $Q_2$ power dissipation with a square wave current of 1 A at 400 Hz.

A new positive-negative phase current commutation method is proposed to use $Q_2$ to share the power consumption of $Q_1$. Figures 4.19 (a) and (b) display previous and new phase commutation methods with the same peak-to-peak current amplitude and the simulated rotational torque. Table 4.2 summarizes the simulation results of rotational torque and the experimental conditions and results of measured power dissipation of the output transistors with different phase commutation methods. The proposed method allows $Q_2$ to share part of the power dissipation and reduce the power dissipation of $Q_1$ by nearly half, but only a 6% average torque reduction. Therefore, further increasing the supply voltage of the linear power amplifiers is possible by using the proposed method.

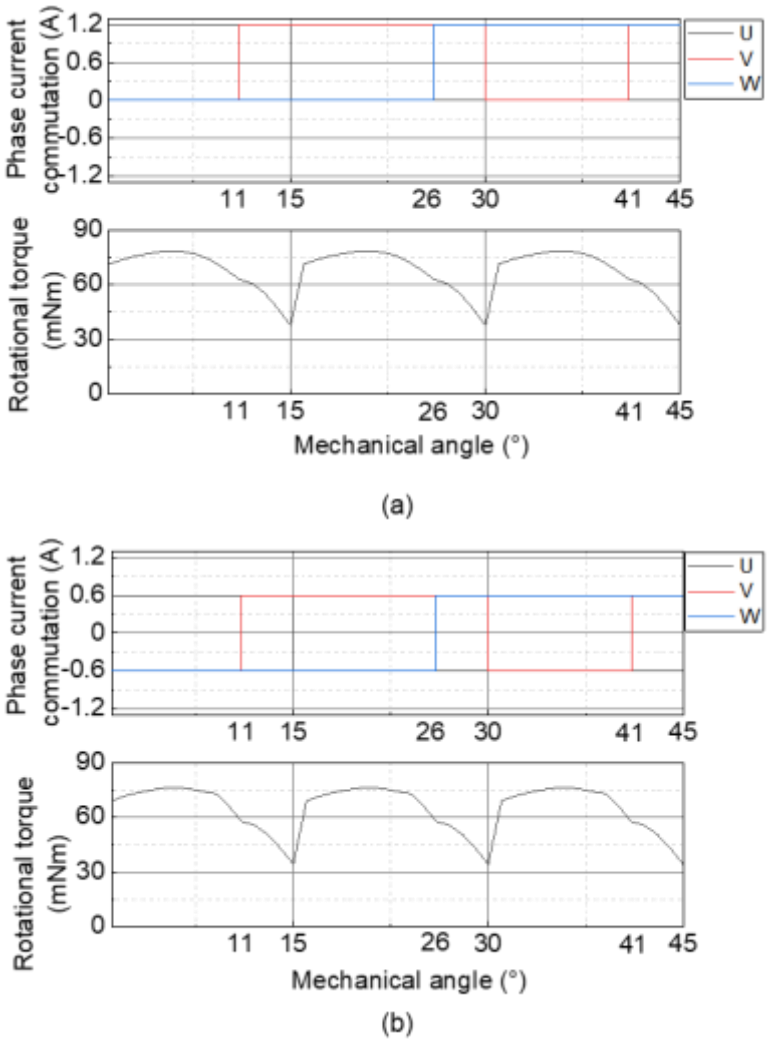


Figure 4.19 Phase commutation method and simulated rotational torque with different mechanical angles: (a) Positive phase current commutation method; (b) Positive-negative phase current commutation method.

Table 4.2 Summaries of the simulated average rotational torque and the experimental conditions and results of measured power dissipation of the output transistors with different phase commutation methods

| | | Positive phase commutation method (Previous) | | Positive-negative phase commutation method (Propose) | |
|---|---|---|---|---|---|
| Simulated average rotational torque | | 0.068 Nm | | 0.064 Nm (94%) | |
| Experimental condition | Current | Sinusoidal current of ± 0.3 A at 50 Hz (Simulated suspension current) Rectangular current with a peak-to-peak amplitude of 1.5 A at 400 Hz (Simulated motor current) | | | |
| | Supply voltage | ±60 V | | | |
| Power dissipation | | $Q_1$ | $Q_2$ | $Q_1$ | $Q_2$ |
| Peak value | | 209.3 W | 13.6 W | 105 W | 83.8 W |
| Average value | | 47.8 W | 1.5 W | 14.7 W | 17.2 W |

*4.5.2.2 Reduction of coil inductance*

Since coil inductance is proportional to the square of the number of turns, reducing the number of turns can effectively decrease the coil inductance, thereby increasing the current-loop bandwidth. Table 4.3 shows the experimental condition and results of measured close-loop bandwidth with two different numbers of turns of the coil. Considering the same heat dissipation of the transistor, using the same PI parameters, and maintaining the same magnetomotive force, the current-loop bandwidth increased from 685 Hz to 1127 Hz, as depicted in Fig. 4.20.

Table 4.3 Experimental condition and results of measured close-loop bandwidth with two different numbers of turns of the coil

| The number of turns of the coil | 386 turns | 300 turns |
|---|---|---|
| Input voltage | ±60 V | ±49 V |
| Coil inductance | 27.2 mH | 16.4 mH |
| Coil resistance | 2.2 Ω | 1.4 Ω |
| Amplitude of excitation current | 0.1 A | 0.128 A |
| Current-loop bandwidth | 685 Hz | 1023 Hz |

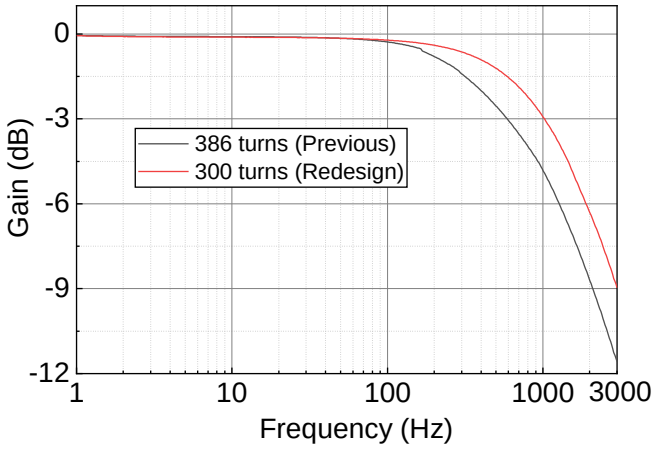


Figure 4.20 Measured current-loop bandwidth with different numbers of the turns of the coil.

## 4.6. Summary

In this chapter, a mock circulatory loop filled with 40wt% aqueous glycerol solution was constructed to evaluate the proposed BELSM and CBP performance. Initially, the suspension and rotation performance of the BELSM were investigated. The system demonstrated successful startup and stable levitation in liquid, achieving an amplitude of 14.5 μm and 10.5 μm in the X and Y directions, respectively.

The accuracy of rotor angle measurement was verified utilizing the low-sensitivity HE and the proposed rotation signal process method to reduce the impact of large currents on HE voltage distortion. Then, implementing the synchronous disturbance elimination method enabled precise rotor rotation, maintaining accuracy within 100 μm even at high speeds and large flow rates.

Hydraulic performance evaluation of the CBP achieved a maximum flow rate of 4.59 L/min and a maximum head pressure of 214.4 mmHg at speeds of 2300 rpm and 2400 rpm, respectively. However, the pump's maximum efficiency was 5.3%. Despite these achievements, the CBP fell short of the target requirements due to rotational speed limitations. The primary factor contributing to this limitation was the low bandwidth resulting from the insufficient output voltage of the linear power amplifiers, causing the actual current to deviate from the reference current.

To further improve the current-loop bandwidth utilizing the existing linear power amplifier, a positive-negative phase commutation method was proposed by reducing the power dissipation of individual transistors in the linear power amplifier, which enables increased input

voltage of the linear power amplifier. Simultaneously, the number of turns in the coil can be reduced to diminish coil inductance, thus improving current response speed.

# Chapter 5 Radial displacement measurement using ECD sensor below the rotor

## 5.1 Introduction

In the CBP utilizing the BELSM, the radial displacement measurement is crucial to achieving precise radial positioning feedback control to achieve contactless support. As the slice rotor is immersed in blood within the pump head, specific requirements govern the choice of radial displacement measurement method: (1) Non-contact measurement; (2) High precision; (3) High bandwidth; (4) Immunity to interference from bubbles and blood thrombus in the liquid.

Placing the ECD sensors along the radial displacement direction is the most standard measurement approach to fulfill the requirements above. These ECD sensors must be oriented towards the high roundness, the nonsalient, and the no-tooth side surface of the rotor to detect the radial displacement of the rotor effectively. The side surface is commonly referred to as a sensor target.

However, in the case of BELSM, the reluctance slice rotor is designed with salient poles on its outer circumference. These salient poles on the outer side of the slice rotor present a challenge in providing a sensor target independent of the rotor angle in the radial direction. Conventional methods, such as placing the sensor target on the inner circumference of the slice rotor or using an additional cylindrical sensor target on the upper or lower part of the slice rotor, have limitations in improving the performance of the CBP due to the constraints of the pump head structure as shown in Figs. 5.1 (a) and (b).

The placement of ECD sensors on the inner side of the slice rotor, as depicted in Fig. 5.1 (a), makes the flow path in the pump head complex due to sensor holder installation. This complexity results in the narrowing of the secondary flow, an increase in fluid resistance, and, consequently, more hemolysis and thrombus formation in the CBP. This placement method has been implemented in the developed CBP, as detailed in Chapter 3.

Furthermore, placing ECD sensors outside, constrained by the limited stator space, requires an increase in the height of the rotor to obtain additional sensor targets, as shown in Fig. 5.1 (b). This increase leads to a rise in the initial priming volume of the pump head. A pump head with a larger initial fill volume results in increased blood product usage and an

expanded contact area between blood and the pump housing surface, leading to hemodilution and an elevated risk of complications during blood transfusion.

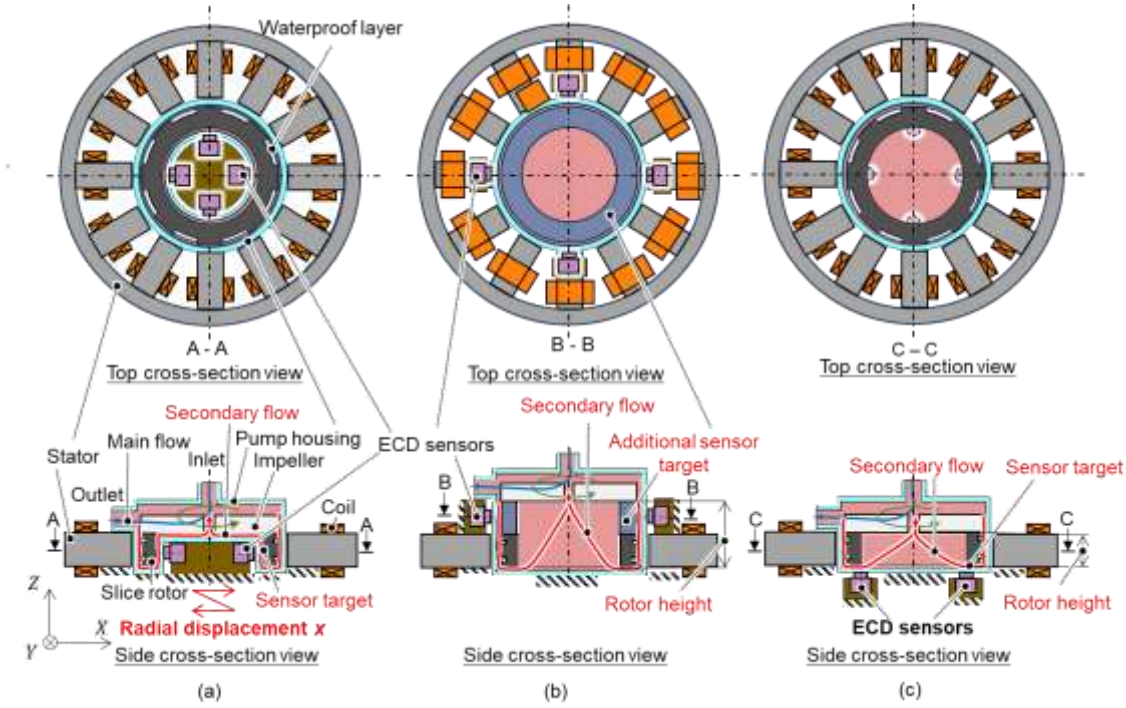


Figure 5.1 CBP utilizing a BELSM with different sensor placements: (a) Pump head structure with the sensor placement inside the slice rotor; (b) Pump head structure with the sensor placement outside the slice rotor; (c) Pump head structure with the proposed sensor placement under the slice rotor.

Therefore, the objective of this chapter is to enhance the design flexibility of the CBP structure by relocating the ECD sensors from their conventional placement on the side of the rotor, illustrated in Figs. 5.1 (a) and (b), to the underside of the rotor, as depicted in Fig. 5.1 (c). This relocation aims to improve the CBP performance while maintaining the same radial displacement measurement accuracy. The proposed sensor placement utilizes the bottom surface as the sensor target, ensuring independence from the rotor angle. Compared to conventional placement methods, this proposed approach eliminates the need for additional sensor targets, thus avoiding an increase in the initial priming volume of the disposable pump head. Furthermore, this placement method prevents the occupation of inner rotor space. The following sections will discuss the principles and feasibility of this proposed sensor placement.

## 5.2 Measurement principle and preliminary experiment

### 5.2.1 Measurement principle

The proposed ECD placement method tackles the issue of measuring radial displacement in the saliency slice rotor of the BELSM using ECD sensors. However, the output voltage of

the ECD sensor is affected by the axial and tilt motions of the rotor, making it challenging to derive radial displacement from the sensor output voltage directly.

In Fig. 5.2, the qualitative comparison illustrates the output voltage variations of ECD sensors concerning the rotor displacement under both conventional and proposed sensor placements. Figure 5.2 (a) depicts the conventional ECD sensor placement for radial displacement measurement. The output voltage of the ECD sensor demonstrates a linear correlation with radial displacement $x$ within a specific range, eventually reaching saturation beyond the measurement range. Assuming the rotor's height $H_R$ is significantly greater than the sensor probe's diameter $Ds$. With a constant initial radial installation distance $g_s$ and radial displacement $x$, the output voltages remain unaffected by axial displacement $z$ when the probe is not near the rotor's upper and lower ends.

In the proposed placement of the ECD sensor at the inner edge of the slice rotor bottom, as depicted in Fig. 5.2 (c), the centerline of the sensor probe is positioned $d/2$ away from the rotor's centerline in the radial direction. Given that part of the rotor bottom surface is utilized as the sensor target, any radial displacement of the rotor will result in changes in the output voltage of the ECD sensor due to alterations in the sensor target area. Assuming the initial axial installation distance $H_s$ and axial displacement $z$ remain constant, this change can be considered as a linear variation within a small radial displacement range. However, the axial displacement $z$ also influences the output voltage because the sensor target faces the probe directly. Therefore, the impact of axial and tilt motions on the output voltage of ECD sensors should be taken into account.

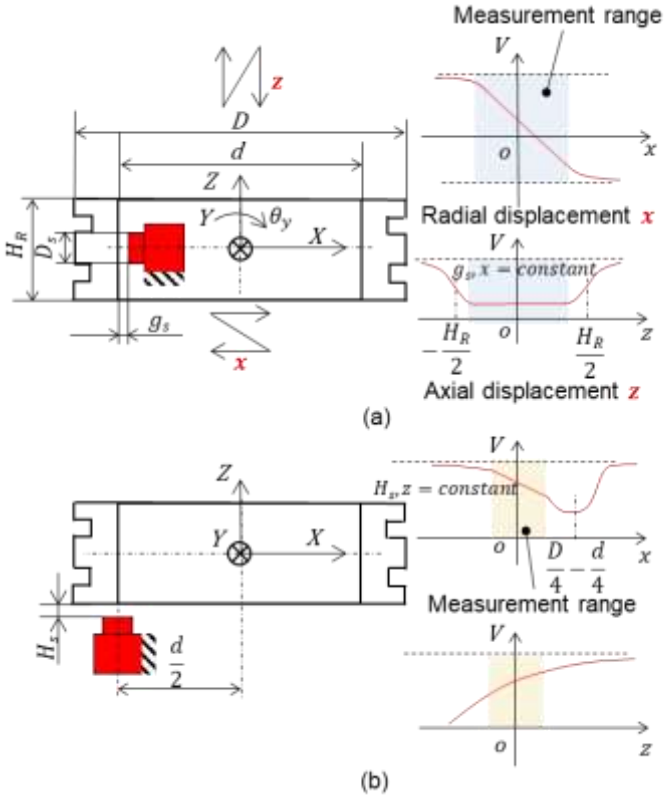


Figure 5.2 Output voltages from the ECD sensor in response to rotor displacements with different sensor placements: (a) Conventional sensor placement; (b) Proposed sensor placement.

### 5.2.2 Preliminary experiment

A preliminary experiment was conducted to validate the proposed sensor placement method, aiming to quantitatively verify the relationship between the output voltage of the ECD sensor and the three individual degrees of freedom (DOF) movements under the proposed sensor placement. The dimensions of the slice rotor mirrored our developed BELSM, as mentioned in Chapter 2. The rotor bottom surface is a flat ring shape with an inner diameter *d* of 38 mm and an outer diameter *D* of 50 mm, as shown in Fig. 5.3 (b). The ECD sensor used in this preliminary experiment is identical to the one employed in Chapter 3, featuring a probe diameter of 5 mm and generating output voltages from 0 to 2 mm within a linear output of ±5 V. Choosing a 5 mm diameter sensor probe is a tradeoff between measurement accuracy and measurement distance. Taking into account the thickness of the bottom housing, the fluid gap at the bottom, and the waterproof layer beneath the rotor, the measurement range of the sensor must be at least 2.5 mm. On the other hand, sensors with smaller diameters can offer increased measurement sensitivity and are also more convenient to arrange, helping avoid interference between multiple sensors due to proximity, thereby improving measurement accuracy.

Figure 5.3 (a) shows the experimental setup of the preliminary experiment. The ECD sensor is securely affixed upside down onto a plastic plate, linked to a micro-stage enabling adjustments along the X- and Y-directions. The rotor is anchored on a mico-stage with the capability to modify its angle. Specifically, the ECD sensor is oriented parallel to the negative X-axis, which is positioned at an initial radial distance of 19 mm from the centerline of the rotor and an initial axial installation distance $H_s$ of 2.1 mm from the bottom surface of the rotor, as illustrated in Fig. 5.3 (a). The specific axial distance $H_s$ was determined by considering factors such as the thickness of the bottom housing, waterproof layer, and fluid gap within the developed CBP in Chapter 3, surpassing the standard linear measurement range. Employing two micro-stages, both the axial and positions of the ECD sensor probe can be adjusted, along with the tile angle of the rotor, from their initial positions and attitudes. The output voltages of the ECD sensor were recorded for each DOF in rotor motion.

Figure 5.4 presents the measurement results of the preliminary experiment, depicting the relationships between the output voltages of the ECD sensor and five individual DOF movements, beginning from the initial position and attitude. Figures 5.4 (a) and (b) depict the variations in output voltage concerning radial displacement $y$ and tilt angle $\theta_x$ at different axial displacements $z$. Since the ECD sensor is placed parallel to the X-axis, the influence of the radial displacement $y$ and tilt angle $\theta_x$ on the output voltage is negligible. As shown in Fig. 5.4 (c), under conditions of constant axial displacement and tilt angles, the output voltage of the ECD sensor demonstrated a linear correlation with radial displacement $x$. Moreover, the slope and intercept of the linear correlation were influenced by axial displacement $z$. Figures 5.4 (d) and (e) further illustrate the susceptibility of sensor output to interference from axial and tilt movement, resulting in notable voltage changes. Figures 5.4 (d) and (e) also highlight the nonlinearity in the sensor output, attributed to the placement of the ECD sensor where the distance to the sensor target exceeds the linear operating range, and the area of the sensor target falls below the standard requirements. Therefore, the compensation for interference from multiple-DOF displacement and nonlinearity is essential.

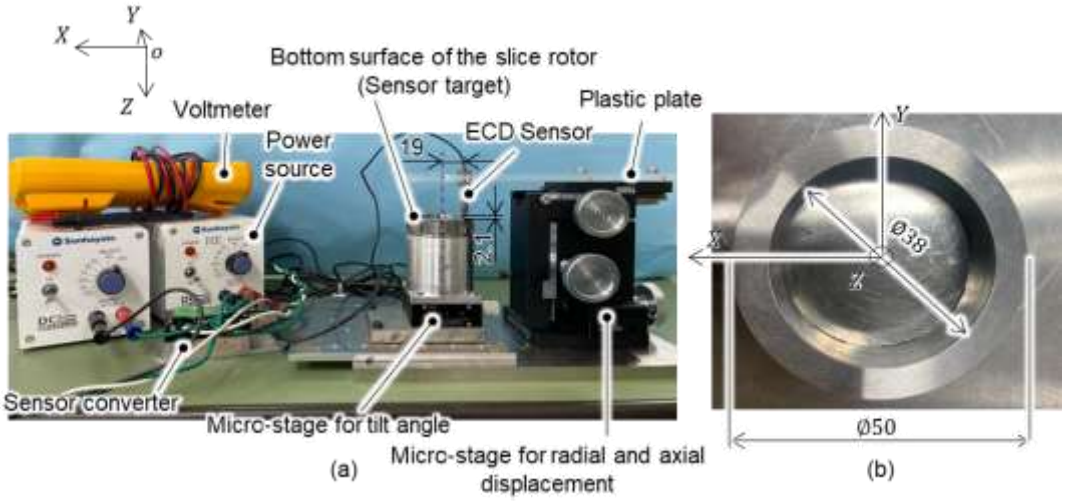


Figure 5.3 (a) Experimental setup of the preliminary experiment; (b) Bottom surface of the slice rotor.

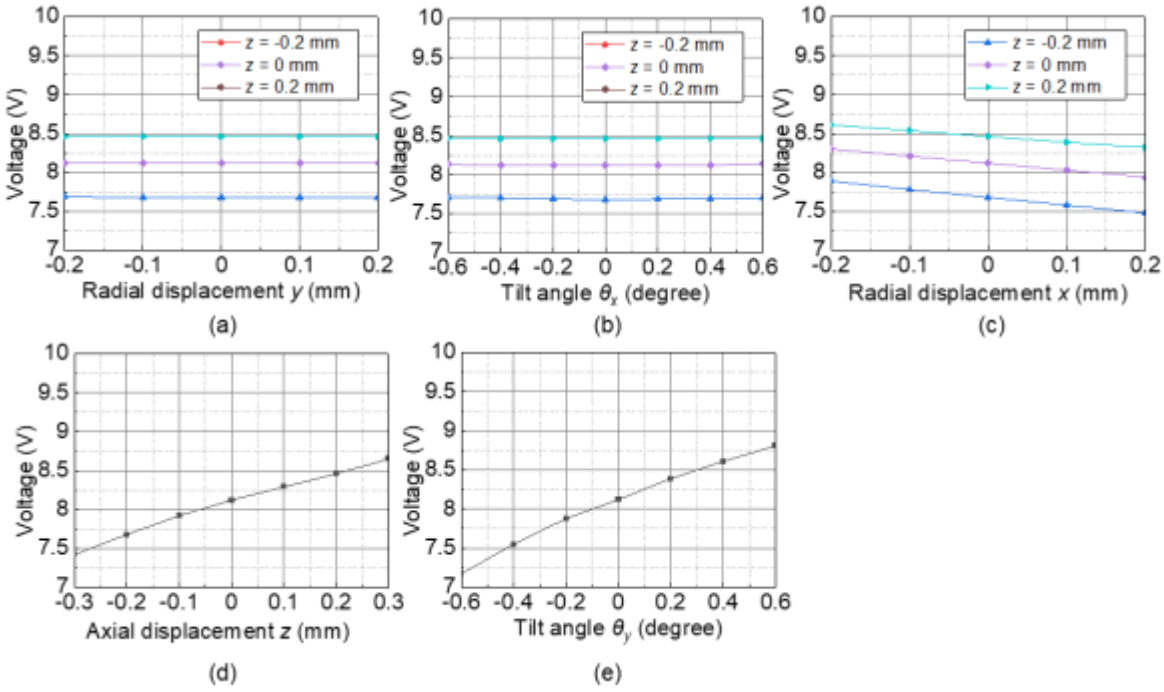


Figure 5.4 Relationships between the output voltages of the ECD sensor and five individual DOF movements by preliminary experiment: (a) Radial displacement $y$ from different axial displacements $z$; (b) Tilt angle $\theta_x$ from different axial displacements $z$; (c) Radial displacement $x$ from different axial displacements $z$; (d) Axial displacement $z$ from the initial position; (e) Tilt angle $\theta_y$ from the initial attitude.

## 5.3 Sensor arrangement

To compensate for the interferences from multiple-DOF displacements and nonlinearity, an arrangement method is proposed to place seven ECD sensors below the slice rotor, as illustrated in Fig. 5.5 (a). As shown in Fig. 5.5 (b), three ECD sensors $S_i$ ($i$ =1-3) were located at the center of the circular ring of the rotor bottom, while the remaining four ECD sensors $S_j$

($j$ =4-7) were mounted under the inner edge of the rotor bottom parallel to the X- and Y-axis, as described in the preceding section.

Due to the installation of the ECD sensor $S_i$, the impact of a small radial displacement on the output voltage of the ECD sensor is assumed to be negligible. Therefore, the functions between output voltages of the ECD sensor and the other three DOF motions can be expressed as Eq. (5.1):

$$V_i = V_i(z, \theta_x, \theta_y) \tag{5.1}$$

where $V_i$ denotes the output voltage of each sensor $S_i$. $z$ is the axial displacement. $\theta_x$ and $\theta_y$ are the tilt angles around the X- and Y- axes, respectively. In principle, the $z$, $\theta_x$, and $\theta_y$ can be calculated by $S_i$ to compensate for the interference from three DOF displacements.

For the ECD sensors $S_j$ positioned parallel to the coordinate axis, the output voltage of these ECD sensors can be assumed to be only affected by three DOF motions, as experimentally verified in section 5.2.2. Two pairs of the ECD sensors $S_6$ and $S_7$, and $S_4$ and $S_5$, are used to calculate the radial displacements in the X- and Y-directions from the output voltage $V_j$ differentially to compensate for nonlinearity and reduce temperature drift and noise. The functions of the $V_j$ can be expressed as follows:

$$V_4 = V_4(y, z, \theta_x) \tag{5.2}$$

$$V_5 = V_5(y, z, \theta_x) \tag{5.3}$$

$$V_6 = V_6(x, z, \theta_y) \tag{5.4}$$

$$V_7 = V_7(x, z, \theta_y) \tag{5.5}$$

where $x$ and $y$ denote the radial displacements in the X- and Y-directions, respectively. In theory, all five DOFs (radial, axial, and tilt motions) affect the output voltage of the ECD sensor placed under the rotor.

The proposed asymmetrical seven-sensor arrangement can not only measure the radial displacements but also simultaneously monitor the axial displacement and tilt angles. The monitoring of axial displacement and tilt angles can effectively observe the rotor motion state during operation.

Assuming these functions can be established through sensor calibration, the output of seven ECD sensors can then be utilized to deduce the radial displacement in both the X- and Y-directions. However, for the proposed seven-sensor placement, calibration must account for the influence of multiple rotor motions and nonlinearity, making precise sensor calibration

challenging. In the following Sections 5.4 and 5.5, the two sensor calibration methods will be proposed and verified.

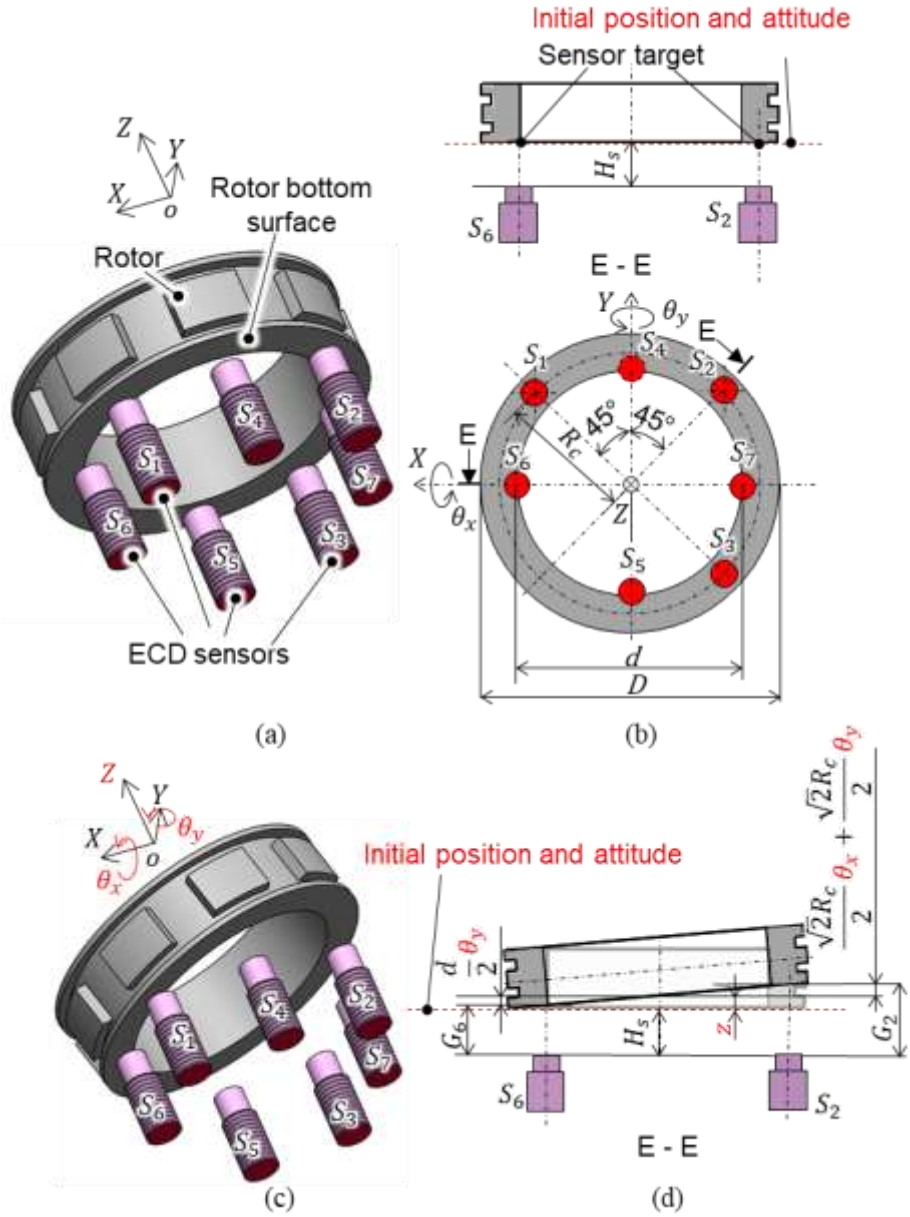


Figure 5.5 Seven ECD sensor arrangement: (a) Schematic diagram of the seven ECD sensor arrangement with initial position and attitude; (b) Bottom and side cross-section view of the seven ECD sensor arrangement with initial position and attitude; (c) Schematic diagram of the seven ECD sensor arrangement with rotor displacements $z$, $\theta_y$, and $\theta_x$; (d) Side cross-section view of the seven ECD sensor arrangement with rotor displacements $z$, $\theta_y$, and $\theta_x$.

## 5.4 Displacement measurement based on the polynomial fitting method

5.4.1 ECD sensor calibration methods using the polynomial fitting method

*5.4.1.1* Axial displacement and tilt angles calculation

The ECD sensors $S_i$ ($i$ = 1-3), located in the middle of the rotor bottom, are assumed to be unaffected by minor radial displacements, which are only affected by the other three DOF motions $z$, $\theta_x$, and $\theta_y$ of the slice rotor. Figure 5.5 (c) shows the schematic diagram of the seven-ECD sensor arrangement with rotor displacement $z$, $\theta_x$, and $\theta_y$. The axial distances $G_i$ of each sensor $S_i$ are defined as the distance between the sensor target and the center point of each sensor probe to simplify the relationships among the three DOF motions of the slice rotor. Figure 5.5 (d) presents the geometrical relationships among the axial distance $G_2$ and the other three DOF motions $z$, $\theta_x$, and $\theta_y$, and the initial installation distances $H_s$ as an example. These mapping between $G_i$ and $V_i$ using polynomial, as shown in Eq. (5.6):

$$G_i = u_i(V_i) \tag{5.6}$$

$$u_i(V_i) = \sum_{l=0}^{q} \alpha_{il} (V_i)^l$$

where $G_i$ is the axial distance, $q$ is the order of the polynomial ($q$ = 0,1,2,…), and $\alpha_{il}$ is the coefficient of each polynomial term for each $u_i$. Through the sensor calibration, each $G_i$ can be derived from each output voltage $V_i$ of $S_i$.

After obtaining the $G_i$, these geometrical relationships of each sensor probe $S_i$ can be assumed as in Eq. (5.7) based on Eq. (5.1):

$$\begin{bmatrix} G_1 \\ G_2 \\ G_3 \end{bmatrix} = \begin{bmatrix} 1 & \frac{\sqrt{2}}{2}R_c & -\frac{\sqrt{2}}{2}R_c \\ 1 & \frac{\sqrt{2}}{2}R_c & \frac{\sqrt{2}}{2}R_c \\ 1 & -\frac{\sqrt{2}}{2}R_c & \frac{\sqrt{2}}{2}R_c \end{bmatrix} \begin{bmatrix} z \\ \theta_x \\ \theta_y \end{bmatrix} + \begin{bmatrix} 1 \\ 1 \\ 1 \end{bmatrix} H_s \tag{5.7}$$

where $R_c$ is the radial distance between the centerlines of the sensor probes $S_i$ and slice rotor. Assuming the $\theta_x$ and $\theta_y$ are sufficiently small, tan$\theta_x$ and tan$\theta_y$ are approximately equal to $\theta_x$ and $\theta_y$, respectively. By performing the inverse matrix transformation of Eq. (5.7), $z$, $\theta_x$, and $\theta_y$ can be derived from $G_i$ using Eq. (5.8) as follows:

$$\begin{bmatrix} z \\ \theta_x \\ \theta_y \end{bmatrix} = \begin{bmatrix} 1/2 & 0 & 1/2 \\ 0 & \frac{\sqrt{2}}{2R_c} & -\frac{\sqrt{2}}{2R_c} \\ -\frac{\sqrt{2}}{2R_c} & \frac{\sqrt{2}}{2R_c} & 0 \end{bmatrix} \begin{bmatrix} G_1 - H_s \\ G_2 - H_s \\ G_3 - H_s \end{bmatrix} \tag{5.8}$$

*5.4.1.2* Radial displacement calculation

Illustrated in Fig. 5.4 (c), the output voltages $V_j$ of $S_j$ show a linear correlation with the radial displacement across various axial displacements while keeping the other DOF motions constant. This correlation can be fitted with a 1st-order linear equation in the X- and Y-directions using Eqs. (5.9)-(5.12):

$$V_4 = k_4(G_4)y + b_4(G_4) \tag{5.9}$$

$$V_5 = k_5(G_5)y + b_5(G_5) \tag{5.10}$$

$$V_6 = k_6(G_6)x + b_6(G_6) \tag{5.11}$$

$$V_7 = k_7(G_7)x + b_7(G_7) \tag{5.12}$$

where $k_j$ and $b_j$ ($j$ = 4-7) represent the slope and intercept of the linear equation, respectively. In the depicted Fig. 5.4 (c), as the constant value of axial displacement varies, the slope and intercept of the 1st-order linear equation exhibit corresponding changes. Therefore, the slope and intercept can be assumed to associate with the axial distance $G_j$ of $S_j$, which is also defined as the axial distance between the sensor target and sensor probes' center points of $S_j$ when ($x$, $y$) = (0, 0). Figure 5.4 (d) shows the axial distance $G_6$ of $S_6$ as an example. When $z$, $\theta_x$, and $\theta_y$ are obtained, $G_j$ can be calculated through the geometrical relationships using Eq. (5.13):

$$\begin{bmatrix} G_4 \\ G_5 \\ G_6 \\ G_7 \end{bmatrix} = \begin{bmatrix} 1 & d/2 & 0 \\ 1 & -d/2 & 0 \\ 1 & 0 & -d/2 \\ 1 & 0 & d/2 \end{bmatrix} \begin{bmatrix} z \\ \theta_x \\ \theta_y \end{bmatrix} + \begin{bmatrix} 1 \\ 1 \\ 1 \\ 1 \end{bmatrix} H_s \tag{5.13}$$

$k_j$ and $b_j$ can be represented by polynomial functions of $G_j$ using Eq. (5.14) and Eq. (5.15), respectively.

$$k_j(G_j) = \sum_{l=0}^{q} \beta_{jl} (G_j)^l \tag{5.14}$$

$$b_j(G_j) = \sum_{l=0}^{q} \gamma_{jl} (G_j)^l \tag{5.15}$$

where $\beta_{jl}$ and $\gamma_{jl}$ represent the coefficients of each polynomial term $k_j$ and $b_j$, respectively. Once these coefficients are determined by polynomial curve fitting, the value of $k_j$ and $b_j$ can be initially calculated by substituting calculated $G_j$ from (5.13) into (5.14) and (5.15). Subsequently, the radial displacements in the X- and Y-directions can be deduced using Eqs. (5.9)-(5.12) and measured output voltages $V_j$ of $S_j$.

The radial displacements in the X- and Y- directions were determined utilizing a pair of ECD sensors positioned between $S_6$ and $S_7$, and $S_4$ and $S_5$, respectively. The differential

measurements can be expressed as Eqs. (5.16) and (5.17) by subtracting Eq. (5.12) from Eq. (5.11) and Eq. (5.10) from Eq. (5.9):

$$x = \frac{V_6 - V_7 + b_7(G_7) - b_6(G_6)}{k_6(G_6) - k_7(G_7)} \tag{16}$$

$$y = \frac{V_4 - V_5 + b_5(G_5) - b_4(G_4)}{k_4(G_4) - k_5(G_5)} \tag{17}$$

Hence, after obtaining the values of $z$, $\theta_x$, and $\theta_y$ from the measured output voltage $V_i$, $z$, $\theta_x$, and $\theta_y$ can be substituted into Eq. (5.13) to calculate the axial distance $G_j$ of $S_j$ when the ($x$, $y$) = (0, 0). Subsequently, using the Eqs. (5.14) and (5.15), the slope $k_j(G_j)$ and intercept $b_j(G_j)$ of the linear equations can be calculated by substituting the $G_j$ into polynomial functions $k_j$ and $b_j$. Finally, by substituting the values of the slope and intercept into Eqs. (5.9)-(5.12), the radial displacements $x$ and $y$ can be obtained through differential measurements, like Eqs. (5.16) and (5.17).

### 5.4.2 Experimental method and results of the polynomial fitting method

In Fig. 5.6, the configuration of the experimental setup is presented, featuring two sensor systems for ECD sensor calibration, one below the rotor and the other on the inner side of the rotor. The carrier frequencies of the ECD sensor amplifiers were carefully selected to avoid interference between the ECD sensor probes. The radial ECD sensors, previously employed for magnetic suspension and individually calibrated for radial displacement measurement, as mentioned in Chapter 3, served as a reference in sensor calibration.

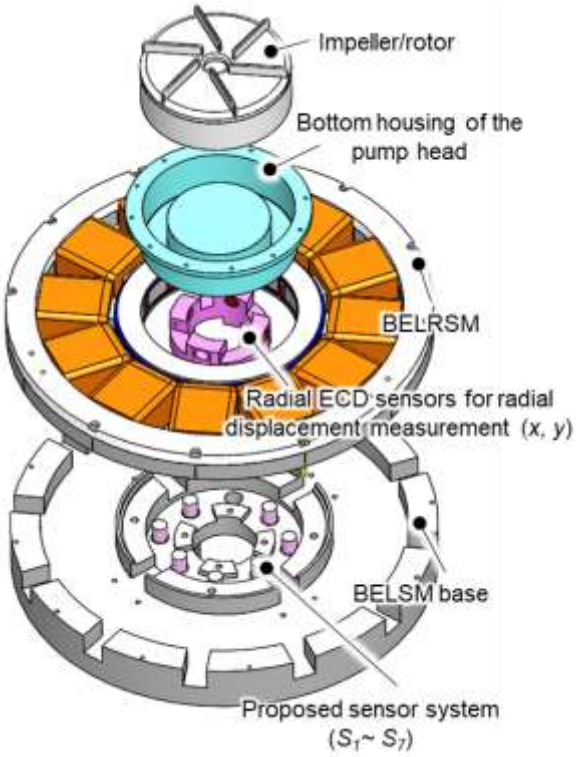


Figure 5.6 Configuration of the experimental setup with two sensor systems for ECD sensor calibration.

To determine the polynomial function order and coefficient of $u_i$, $k_j$, and $b_j$, experimental variations were introduced in axial distance $G_i$ and $G_j$, radial displacement ($x$, $y$), and the corresponding output voltage $V_i$ and $V_j$ were recorded for sensor calibration. Figure 5.7 (a) illustrates the experimental setup for sensor calibration based on the polynomial fitting method. The top housing of the pump head was removed, and the slice rotor was directly placed into the bottom housing of the pump head and pressed with a pressure plate to prevent tilting. Various polyester films of 0.1 mm thickness, as shown in Fig. 5.7 (b), were inserted into the radial and axial gaps between the slice rotor and bottom housing wall to vary the axial distance $G_i$ and $G_j$ and radial displacement ($x$, $y$) of the slice rotor.

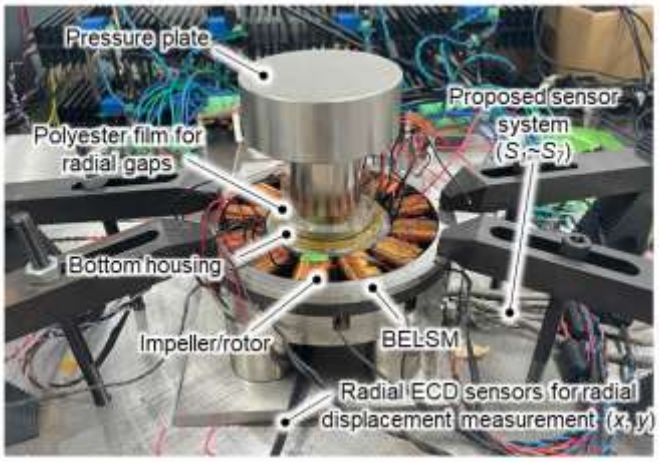


(a)

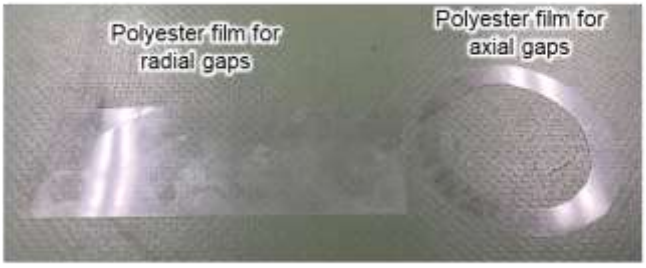


(b)

Figure 5.7 Experimental method of ECD sensor calibration based on the polynomial fitting method: (a) Experimental setup; (2) Polyester film for axial and radial gaps.

In Figs 5.8, the results of the experimental sensor calibration using the polynomial fitting method are shown. The polynomial functions $u_i$ and the 2$^{nd}$-order fitted curves are depicted in Fig. 5.8 (a). Figure 5.8 (b) illustrates the variation of $V_4$ with y at different $G_4$ values and the fitted line of $S_4$. The two pairs of ECD sensors, $S_6$ and $S_7$, $S_4$ and $S_5$, display similar linear trends with radial displacements in the X- and Y-directions, respectively. The slopes and intercepts of the fitted linear equations of $S_j$ with different $G_j$ are shown in Figs. 5.8 (c) and (d), respectively. These relationships were fitted using a 2nd-order polynomial in the figure.

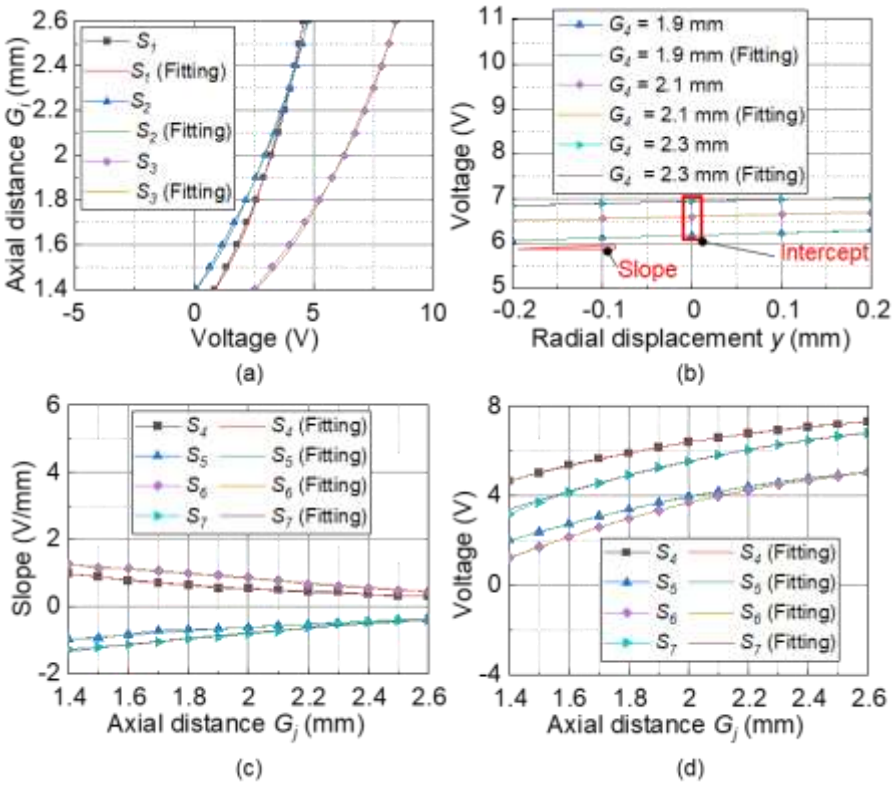


Figure 5.8 Experimental sensor calibration results using the polynomial fitting method: (a) Axial distance $G_i$ at different output voltages $V_i$ and 2nd-order fitted curves; (b) Variation of output voltage $V_4$ with radial displacement $y$ at different axial distances $G_4$ and the fitted lines of $S_4$; (c) Slopes of the linear equations of $S_j$ with different axial distances $G_j$; (d) Intercepts of the linear equations of $S_j$ with different axial distances $G_j$.

After deriving the polynomial functions $u_i$, $k_j$, and $b_j$ through sensor calibration, the computation process from measured output voltages $V_i$ and $V_j$ to radial displacement was implemented into the DSP. The radial displacement results measured by the proposed sensor system are compared with those measured by the radial ECD sensors to evaluate the measurement accuracy. The BELSM rotor was not magnetically suspended but moved around the bottom housing wall. This movement was induced by injecting a sinusoidal current into the coil windings. The trajectory of this motion was measured using both the radial ECD sensors and the proposed sensor system, as depicted in Fig. 5.9 (a). The maximum error between the proposed sensor system and radial ECD sensors was found to be 44 μm and 56 μm in the X- and Y-direction, respectively, as shown in Figs. 5.9 (b) and (c). These errors are deemed unacceptable for the precise radial displacement feedback control system required for magnetic suspension.

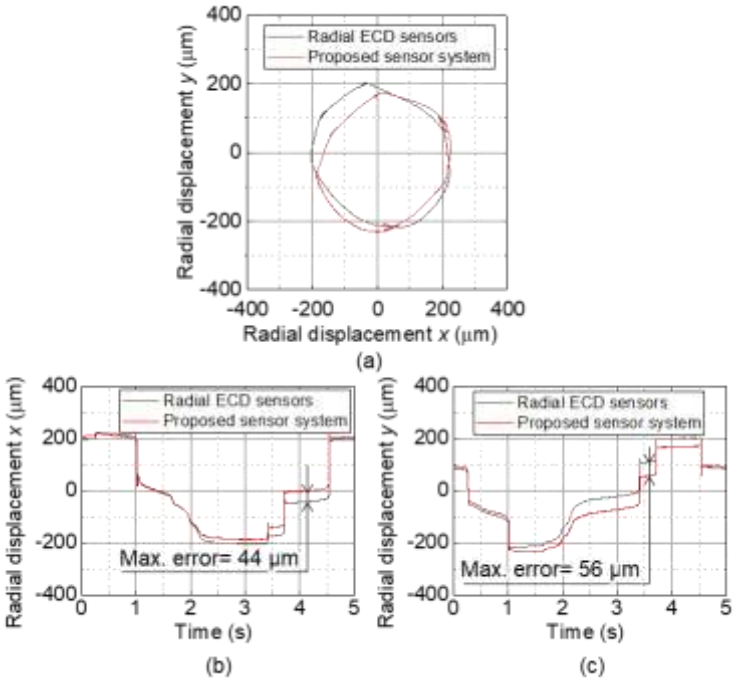


Figure 5.9 Experimental results of the displacement estimation based on the polynomial fitting method: (a) Trajectory of radial motion ($x$, $y$); (b) Radial displacement $x$; (c) Radial displacement $y$.

Calibration of the ECD sensors within the BELSM is crucial for ensuring accuracy and repeatability. The large measurement errors associated with the polynomial fitting method resulted from the inaccuracies of the sensor calibration and the calculated intercept $b_j$. Polyester films of 0.1 mm thick did not provide a sufficiently small radial displacement variation within the 0.2 mm radial gap necessary for precise sensor calibration of $S_j$, which results in inaccurate slopes and intercepts of the 1$^{st}$-order linear equation at various $G_j$, thereby affecting the fitting of polynomials functions $k_j(G_j)$ and $b_j(G_j)$. Furthermore, $G_j$ is assumed to neglect the influence of the tilt angles, making the intercept $b_j$ solely dependent on $G_j$. However, since $S_j$ is positioned at the inner edge of the rotor bottom, the impact of the tilt angles on its output voltage cannot be dismissed, unlike the effect on $S_i$. Consequently, this results in a significant error in calculating the intercept $b_j$ via the polynomial functions $b_j(G_j)$, thus causing a large radial displacement measurement error. To address these problems, the following section proposes sensor calibration using the neural network (NN) method, aiming to establish complex nonlinear relationships and achieve precise measurements of radial displacement.

## 5.5 Displacement measurement based on the neural network method

5.5.1 ECD sensor calibration methods using the neural network method

The relationship between the outputs of seven ECD sensors and two radially positioned ECD sensors fitted with higher-order polynomial functions has been elucidated. Nonetheless, achieving the desired level of accuracy remains a challenge. A feedforward NN employing a backpropagation algorithm was introduced to enhance the measurement accuracy. The structure of NN can model nonlinear input-output relationships, and the backpropagation algorithm can automatically determine the NN parameters, respectively.

The NN architecture depicted in Fig. 5.10 consists of the input, hidden, and output layers. Each layer incorporates multiple neuron units that receive inputs from all neurons in the preceding layer. The total input is computed as the sum of the neuron outputs in the preceding layer, multiplied by the weights, and added to the bias. This input is then transformed using an activation function to generate the neuron's output. The equation for forward propagation and the activation function are illustrated in Eqs. (5.18) and (5.19):

$$N_n = \sum_{m=1}^{p} w_{nm} a_m + B_n \ (n = 1, 2, \dots, c) \tag{5.18}$$

$$a_n = g(N_n) = \frac{2}{1+e^{-2N_n}} - 1 \tag{5.19}$$

where *p* and *c* represent the quantities of neurons in the preceding and current layers, respectively. $N_n$ represents the input of the *n*th neuron in the current layer from the preceding layer. $w_{nm}$ and $B_n$ denote the weight of the connection originating from the *m*th neuron in the preceding layer to the *n*th neuron in the current layer and the bias values of the *n*th neuron in the current layer, respectively. Meanwhile, $a_n$ and $a_m$ represent the output of the *n*th and *m*th neurons in the current and preceding layers, respectively. The function $g$ symbolizes the appropriate activation function, which, in this case, is characterized by a hyperbolic tangential sigmoid function.

In the NN training process, determining weights and biases relies on a dataset encompassing input data and their corresponding desired output values. Initially, weights are assigned random suitable values and adjusted using the gradient descent method through iterations. The gradient descent method can minimize the mean square errors (MSEs), calculated as the average squared difference between the predicted and desired outputs across the entire dataset for NN training. This minimization process serves as the loss function. The backpropagation algorithm is then employed to propagate the error backward through the NN, as illustrated in (5.20)-(5.23), facilitating the update of weights and biases in each layer:

$$\widehat{w}_{nm} = w_{nm} + \Delta w_{nm} \tag{5.20}$$

$$\Delta w_{nm} = -\eta \frac{\partial E}{\partial N_n} a_m \tag{5.21}$$

$$\hat{B}_n = B_n + \Delta B_n \tag{5.22}$$

$$\Delta B_n = -\eta \frac{\partial E}{\partial N_n} \tag{5.23}$$

where $\Delta w_{nm}$ and $\Delta B_n$ denote the weight and bias correction terms, respectively. $\hat{w}_{nm}$ and $\hat{B}_n$ represent the updated weights and biases, respectively. $E$ corresponds to the MSEs, and $\eta$ is the learning rate parameter to control the convergence rate of the NN and stability. The Levenberg-Marquardt algorithm serves as the training function, with this iterative process continuing for multiple epochs until the MSEs reach a minimum or converge to a certain value.

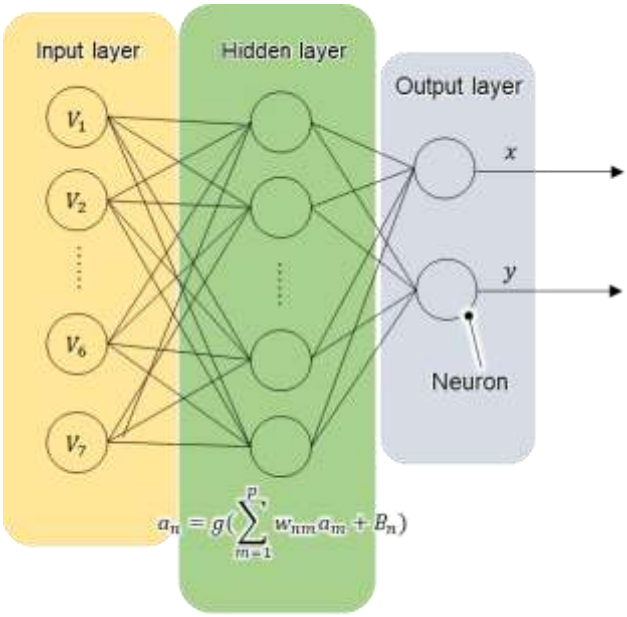


Figure 5.10 Neural network architecture.

Considering the computational time constraints for real-time implementation on a digital signal processor (DSP), an NN with a simple architecture is used with one hidden layer. The hidden, input, and output layers comprise ten, seven, and two neurons. The neurons in the input layer received the output voltages of the seven ECD sensors, whereas the radial displacements measured in the X- and Y-directions by the radial ECD sensors were fed into the output layer. One hidden layer with ten neurons is adapted for establishing the relationship between sensor output voltages and radial displacements, which reaches a tradeoff among precision fitting requirements, training time, and hardware resources for real-time implementation. The NN was designed using the NN toolbox in MATLAB.

Expanding the number of neurons and hidden layers in NN facilitates the more complex models, enabling advanced nonlinear fitting and potentially improving the accuracy of the fitting process. Nonetheless, it is crucial to exercise caution when employing an excessively large

number of neurons and hidden layers, as it may result in overfitting. Additionally, complex models involve a higher count of parameters, translating to longer training times and heightened utilization of hardware resources during real-time implementation.

### 5.5.2 Construction of the dataset for NN training

A comprehensive dataset for NN training that includes diverse slice rotor positions and attitudes is required to train a precise NN. An outlet-clamped mock circulatory loop filled with 40 wt% glycerol aqueous solution was used, as previously detailed in Chapter 4. The BELSM rotor was magnetically suspended utilizing the radial displacements measured by the radial ECD sensors. Simultaneously, the axial displacement and tilt angles were measured utilizing three calibrated ECD sensors $S_i$, as outlined in Section 5.4.1. A. The radial positioning and speed feedback control systems were consistent with those employed in Chapter 3, but the parameter values in the radial positioning control system were slightly different. These adjustments aim to slightly decrease the bandwidth while enhancing stability to meet the requirements of various wide-range positions and attitudes of the slice rotor at a high rotational speed. The displacement feedback controller parameters are listed in Table 5.1.

Diverse experimental conditions were configured to simulate the various rotor positions and attitudes. The startup responses with varying initial positions were measured. Furthermore, the radial circular orbital motion with various amplitudes under non-rotating and rotating conditions was measured. The experimental condition types of the dataset for NN training are listed in Table 5.2.

Figure 5.11 illustrates the measured radial, axial, and tilt responses during the magnetic suspension startup from the distinct initial position along the positive and negative directions of the X- and Y-axes. The lines represent responses from various initial startup positions with the same PID parameter in the control system. The different initial positions result in distinct radial orbits, as shown in Fig. 5.11 (a). The axial and tilt orbits also exhibit variations with different initial values, as shown in Figs. 5.11 (a), (b), and (c), which are to replicate the variations in rotor position and attitude that occur during the startup in the real operation.

Table 5.1 Displacement feedback control parameter for dataset capture

| Parameters | Values |
|---|---|
| Proportional gain [A/m] | 5000 |
| Integral gain [A/m·s] | 8000 |
| Derivative gain [A·s /m] | 4 |
| Cut-off frequency of the first-order LPF for derivative part [Hz] | 500 |
| Cut-off frequency of the second-order LPF [Hz] | 200 |
| Damping ratio of the second-order LPF | 0.707 |

Table 5.2 Lists of the experimental condition types of the dataset for NN training

| Experimental condition types of the dataset for NN training | | |
|---|---|---|
| Types | Parameters | Positions and values |
| Magnetic suspension startup with different initial positions | Initial positions | Positive and negative directions of the X-axis; Positive and negative directions of the Y-axis |
| Magnetic suspension with the different radial circular orbit targets | Amplitudes of several radial circular orbit targets [μm] | 0/10/20/30/40/50 60/70/80/90/100 |
| Magnetic suspension at different rotational speeds with the different radial circular orbit targets | Amplitudes of several radial circular orbit targets [μm] | 0/10/20/30 |
| | Rotational speeds [rpm] | 100/300/500/700/900 1100/1300/1500/1700 |

The radial circular orbit targets with amplitudes of 20, 40, 60, and 80 μm at a frequency of 1 Hz were input into the compensator during non-rotation. The corresponding measured radial, axial, and tilt responses are illustrated in Fig. 5.12. Various radial circular orbits are depicted in Fig. 5.12 (a). Larger amplitudes of the radial circular orbit led to more substantial variations in the axial displacements and tilt angles, as evidenced in Figs. 5.12 (b), (c), and (d), respectively.

The average axial displacements were determined by adjusting the rotational speed from 300 to 1500 rpm in the outlet-clamped mock circulatory loop. This adjustment resulted in a dataset with a broader range of axial displacement variations attributed to differences in the hydraulic pressure between the upper and lower surfaces of the rotor/impeller, which are resented in Fig. 5.13.

The measured radial, axial, and tilt responses of the compensator at a speed of 900 rpm are represented in Fig. 5.14. These responses were measured when several small radial circular orbit targets with amplitudes of 10, 20, and 30 μm at a frequency of 1 Hz were introduced. The amplitudes of the axial displacement and tilt angles also exhibited variations corresponding to the amplitudes of the radial circular orbit target, as indicated in Figs. 5.14 (b), (c), and (d). The radial, axial, and tilt responses at the other rotational speed showed consistent trends.

To ensure accurate radial displacement measurement during suspension under startup, non-rotating, and rotating conditions, a diverse dataset for NN training must cover variations in the rotor displacement and attitude across these conditions. This diversity was achieved by adjusting the control parameters, such as the reference displacement and rotational speed. For the suspension startup and non-rotating conditions, various initial startup positions were set to simulate the substantial variation in axial displacement and inclination arising from the large positioning force during startup, as depicted in Fig. 5.11. Additionally, a range of radial circular orbits were employed to offer a diverse set of radial displacement changes, as illustrated in Fig. 5.12. For suspension under rotating conditions, different rotational speeds were utilized to replicate a broad range of axial displacement variations induced by the hydraulic force, as shown in Fig. 5.13. Furthermore, different radial circular orbits were set to simulate large rotor inclination and radial displacement during rotation, as presented in Fig. 5.14.

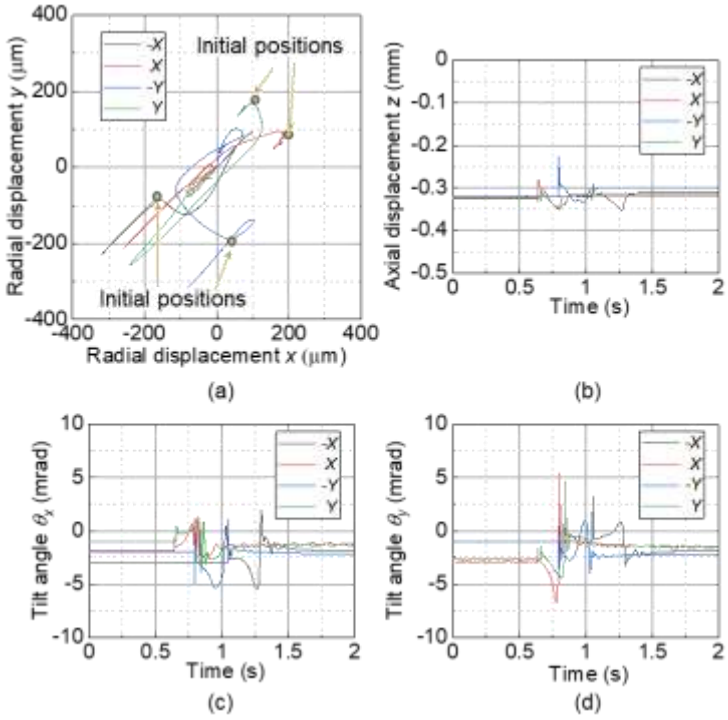


Figure 5.11 Magnetic suspension startup with different initial positions in the positive and negative directions of the X- and Y-axes: (a) Trajectories of rotor radial motion ($x$, $y$) measured by the radial ECD sensors; (b) Axial displacement $z$ measured by the calibrated ECD sensors $S_i$; (c) Tilt angle $\theta_x$ measured by the calibrated ECD sensors $S_i$; (d) Tilt angle $\theta_y$ measured by the calibrated ECD sensors $S_i$.

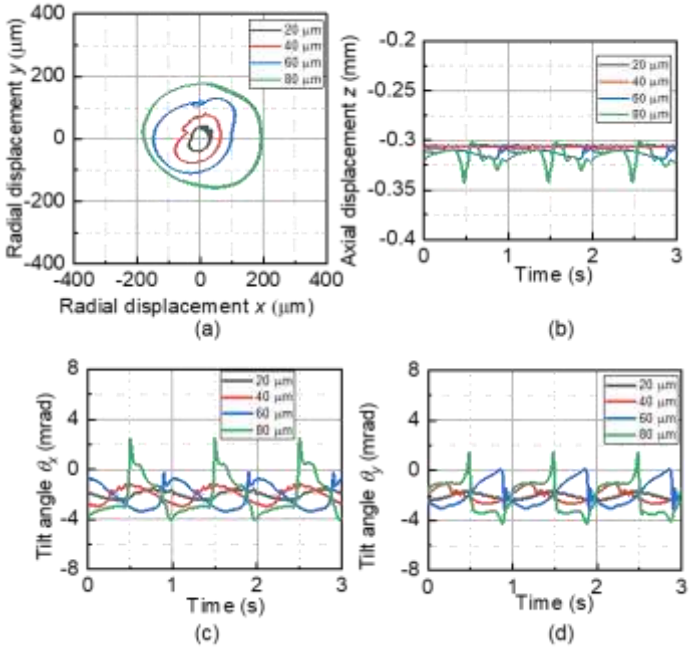


Figure 5.12 Magnetic suspension when several radial circular orbit targets with amplitudes of 20, 40, 60, and 80 μm at a frequency of 1 Hz were inputted into the compensator during non-rotation: (a) Trajectories of rotor radial motion ($x$, $y$) measured by the radial ECD sensors; (b) Axial displacement $z$ measured by the calibrated ECD sensors $S_i$; (c) Tilt angle $\theta_x$ measured by the calibrated ECD sensors $S_i$; (d) Tilt angle $\theta_y$ measured by the calibrated ECD sensors $S_i$.

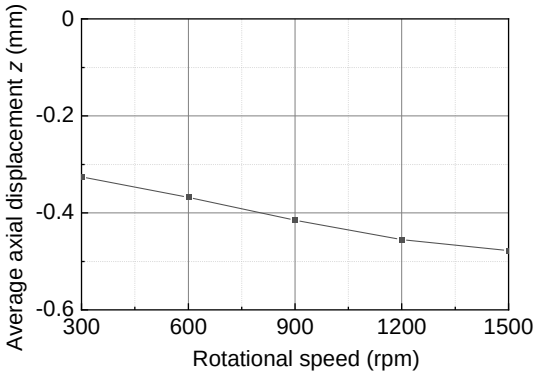


Figure 5.13 Average measured axial displacements obtained by varying the rotational speeds from 300 rpm to 1500 rpm with the outlet-clamped mock circulation loop using the calibrated ECD sensors $S_i$.

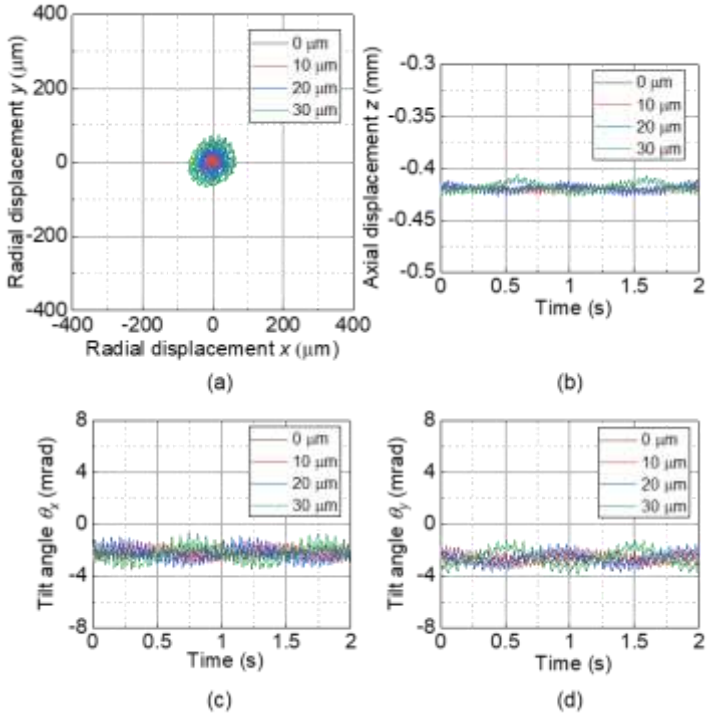


Figure 5.14 Magnetic suspension at a speed of 900 rpm when several radial circular orbit targets with amplitudes of 10, 20, and 30 μm at a frequency of 1 Hz were input into the compensator: (a) Trajectories of rotor radial motion ($x$, $y$) measured by the radial ECD sensors; (b) Axial displacement $z$ measured by the calibrated ECD sensors $S_i$; (c) Tilt angle $\theta_x$ measured by the calibrated ECD sensors $S_i$; (d) Tilt angle $\theta_y$ measured by the calibrated ECD sensors $S_i$.

### 5.5.3 Experimental method of the NN method

The dataset utilized for training the NN was captured under various experimental conditions in the outlet-clamped mock circulatory loop, employing a sampling frequency of 5 kHz for 3 seconds, as delineated in Table 5.2. This dataset encompasses a total of 765,000 time response points. Using the MATLAB NN toolbox, the time responses were randomly allocated into the train, validation, and test sets in a ratio of 7:1.5:1.5, resulting in 535,500 points for the

train set, 114,750 points for the valid set, and 114750 points for the test set. To decrease high-frequency noise, the measured seven raw output voltages of the sensors below the rotor were passed through a 2nd-order LPF with a cut-off frequency of 200 Hz, aligning with the settings for the radial ECD sensors, as outlined in Table 5.1.

The time responses of the measured output voltages from the seven ECD sensors and the corresponding radial displacements obtained via the radial ECD sensors in diverse experimental conditions served as input and desired output for the NN training. The NN training was accomplished using the NN toolbox three times to verify the repeatability and the NN with the best training result was selected for comparison and experiment, achieving a minimum MSE of 60.3 $\mu m^2$ after 1000 epochs. The training process was executed on a workstation (CPU: Intel® Xeon® Silver 4214R; Memory: 64GB.), taking a total training time of 100 min. Subsequently, the trained NN was implemented in DSP for real-time calculation of radial displacements in the X- and Y-directions from the outputs of seven sensors, operating at a sampling frequency of 20 kHz.

### 5.5.4 Experimental results of the NN method

#### *5.5.4.1* Sensor measurement characteristics using the NN method

The linearity and bandwidth of the radial displacement measured utilizing the NN were evaluated. In the linearity evaluation, the slice rotor of BELSM was precisely positioned by the radial ECD sensors. Subsequently, a sinusoidal signal with a frequency of 0.1 Hz and an amplitude of 150 μm was injected into the reference displacements along the X- and Y-directions. Across the range of ±150 μm, the maximum errors between the evaluated radial displacement from the proposed sensor system and the reference radial displacement measured by the radial ECD sensors were determined to be 13.6 μm and 17.1 μm in the X- and Y-directions, as depicted in Figs. 5.15 (a) and (b), respectively.

A sinusoidal current with an amplitude of 0.1 A was introduced into the reference current in the X- and Y-directions to evaluate the measurement bandwidth. The frequency responses from the radial displacement measured by the radial ECD sensors to the evaluated radial displacement by the proposed sensor system using the NN method were measured. As illustrated in Figs. 5.16 (a) and (b), the measured frequency responses in the X- and Y-directions indicated an absence of attenuation within the cut-off frequency 200 Hz of the LPF. Nonetheless, specific frequency ranges exhibited a measured gain greater than 0 dB, attributable to significant vibration in the radial, axial, and tilt directions induced by the current excitation within these specific frequency ranges. Such large rotor motions and attitudes were not included in the previous dataset

for NN training from Table 5.2, resulting in inaccuracies in radial displacement measurement within these frequency ranges. Addressing this limitation may involve enhancing the dataset to encompass a broader range of rotor motion and attitude.

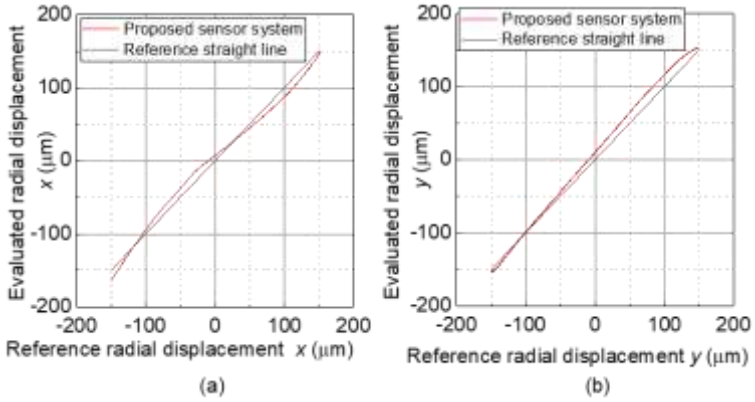


Figure 5.15 Sensor linearity between the reference radial displacement measured using radial ECD sensors and evaluated radial displacement measured using the proposed sensor system based on the NN method: (a) X direction; (b) Y direction.

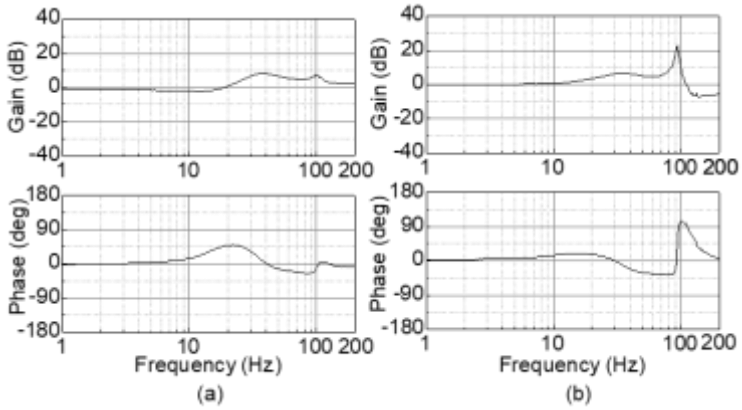


Figure 5.16 Measured frequency responses from the radial displacement measured using the radial ECD sensors system to the evaluated radial displacement measured using the proposed sensor system based on the NN method: (a) X direction; (b) Y direction.

*5.5.4.1* Displacement feedback experiments using the NN method

The feedback of the radial displacements using the proposed sensor system based on the NN methods achieved the magnetic suspension startup and stable rotation within 1700 rpm. Figures 5.17 (a) and (b) illustrate the measured radial displacement in the X- and Y-directions during the magnetic suspension startup, respectively. At startup with significant axial and tilt displacements, the difference between the outputs of the radial ECD sensors and the proposed method remains negligible. During the stable state condition, errors of 3.5 μm and 1.5 μm were measured in the X- and Y-directions, respectively.

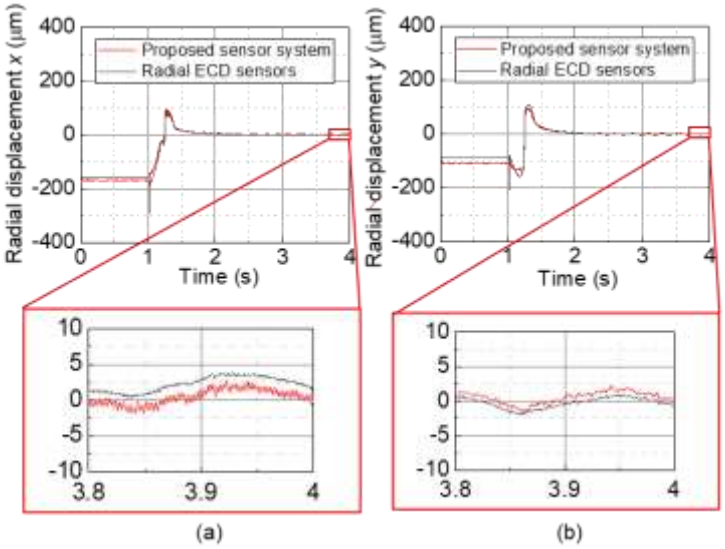


Figure 5.17 Displacement feedback control based on the evaluated radial displacement using the proposed sensor system during magnetic suspension startup: (a) X direction; (b) Y direction.

Figures 5.18 (a) and (b) show the measured radial displacements in the X- and Y-directions at a speed of 1700 rpm. This speed represents the highest rotational speed within the experimental conditions of the dataset for NN training from Table 5.2. The root mean square errors (RMSEs) between radial displacement measured with radial ECD sensors and that evaluated using the proposed sensor system were 11.3 μm and 8.8 μm in the X- and Y-directions, respectively. As delineated in Table 5.3, the RMSEs consistently remained within 16 μm across various rotational speeds within 1700 rpm.

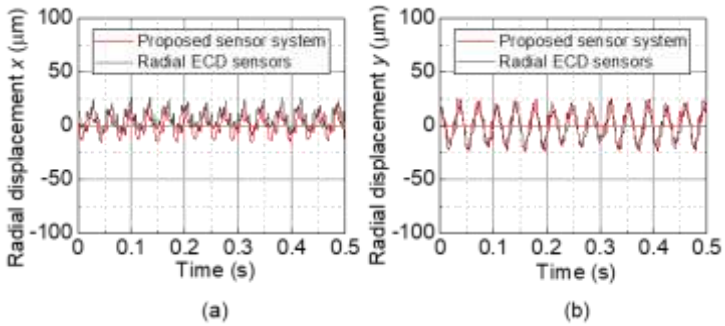


Figure 5.18 Displacement feedback control based on the evaluated radial displacement measured using the proposed sensor system at a speed of 1700 rpm: (a) X direction; (b) Y direction.

Table 5.3 RMSEs between the radial displacements measured using the radial ECD sensors and proposed sensor system at different rotational speeds in the X- and Y- directions

| Rotational speeds [rpm] | RMSE [μm] | |
|---|---|---|
| | X direction | Y direction |
| 300 | 12.4 | 16.0 |
| 600 | 12.6 | 12.3 |
| 900 | 12.9 | 9.0 |
| 1200 | 15.0 | 10.4 |
| 1500 | 12.0 | 9.8 |
| 1700 | 11.3 | 8.8 |

### 5.5.5 Reduction of the dataset for NN training

The dataset size for NN training plays a crucial role in determining the accuracy of the NN and the training time. In the previous experiment in Section 5.5.3, a sampling frequency of 5 kHz and a sampling time of 1s for each experimental condition from Table 5.2 were chosen to capture the dataset for NN training. This section will discuss the effects of the downsized datasets on the accuracy of NN and training time and explore methods for reducing the dataset capture task and NN training time while maintaining the same level of NN accuracy.

Table 5.4 Lists of the decreased variety of the experimental conditions types of the dataset for NN training

| Decreased variety of the experimental condition types of the dataset for NN training | | |
|---|---|---|
| Types | Parameters | Positions and values |
| Magnetic suspension startup with different initial positions | Initial positions | Positive and negative directions of the Y-axis |
| Magnetic suspension with the different radial circular orbit targets | Amplitudes of several radial circular orbit targets [μm] | 0/20/40/60/80/100 |
| Magnetic suspension at different rotational speeds with the different radial circular orbit targets | Amplitudes of several radial circular orbit targets [μm] | 0/10/20/30 |
| | Rotational speeds [rpm] | 100/500/900/1300/1700 |

The reduced variety of experimental condition types and decreased sampling frequency and time contribute to a downsized dataset. Table 5.4 displays the decreased variety of experimental condition types of the dataset for NN training. Besides, Table 5.5 lists the different datasets for NN training under various conditions. Datasets 2 and 3 in Table 5.5 reveal that decreasing the sampling frequency and time, while maintaining the same types of experimental conditions, results in an increase in the calculated MSEs and a decrease in training time. When the sampling frequency and time are reduced to 500 Hz and 1 s, respectively, while ensuring the sampling frequency is greater than twice the cut-off frequency of the LPF for ECD sensors, the final calculated MSE increases a little from 60.3 $\mu m^2$ to 63.8 $\mu m^2$. Simultaneously, the training time significantly decreases from 100 min to 4 min. Furthermore, when the number of experimental condition types of dataset for NN training is reduced, like Table 5.5, the training time decreases due to the reduction in the number of time response points. However, the calculated MSE increases significantly from 60.3 $\mu m^2$ to 91.6 while maintaining the same sampling frequency and time.

Table 5.5 Lists of different datasets for NN training under various conditions

| Datasets | 1 | 2 | 3 | 4 | 5 |
|---|---|---|---|---|---|
| Experimental condition types | Table 5.3 | Table 5.3 | Table 5.3 | Table 5.5 | Table 5.5 |
| Sampling frequency (Hz) | 5000 | 500 | 100 | 5000 | 100 |
| Sampling time (s) | 3 | 1 | 1 | 3 | 1 |
| Time response points | 765000 | 25500 | 5100 | 420000 | 2800 |
| Training time (min) | 100 | 4 | 1 | 70 | 0.5 |
| Final calculated MSE ($\mu m^2$) | 60.3 | 63.4 | 80.4 | 91.6 | 121.1 |

The outputs from seven ECD sensors at varying rotational speeds were inputted into different NNs obtained from different datasets from Table 5.5 to estimate radial displacements. The calculated radial displacement results were compared with measurements obtained using radial ECD sensors for measurement accuracy evaluation. Figures 5.19 (a) and (b) show the measurement accuracy of RMSE using NNs trained by different datasets in Table 5.5 at different

rotational speeds in the X- and Y-directions, respectively. Datasets with greater numbers and diversity result in higher measurement accuracy. Therefore, increasing the diversity of the experiment condition types in the datasets for NN training can expand the operational range and improve the accuracy. Besides, choosing adequate sampling frequency and time can significantly reduce training time.

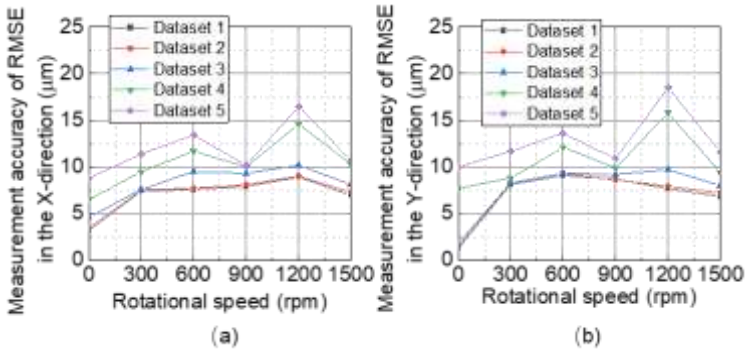


Figure 5.19 (a) Measurement accuracy of RMSE using NNs trained by different datasets in Table 5.5 at different rotational speeds in the X-direction; (b) Measurement accuracy of RMSE using NNs trained by different datasets in Table 5.5 at different rotational speeds in the Y-direction.

After comparing the measurement accuracy of NNs, the closed-loop feedback experiments based on the evaluated radial displacement using the NN trained by dataset 4 in Table 5.5 were conducted. When the radial displacement obtained by the NN was used as the feedback signal, the rotor became unstable at startup in the X- and Y-directions, as shown in Fig.5.20 (a) and (b), respectively. After reaching the origin position, the radial displacement oscillates without achieving convergence.

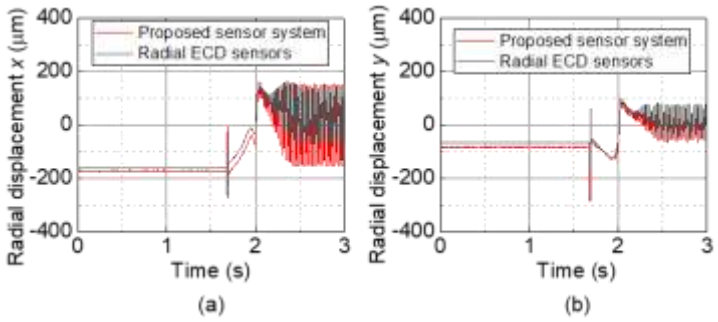


Figure 5.20 Measured radial displacement during displacement feedback control based on the evaluated radial displacement using NN trained by dataset 4 in Table 5.5 at magnetic suspension startup: (a) X direction; (b) Y direction.

Stable suspension near the original position can be achieved by switching the feedback signals measured by the radial ECD sensors only at startup to the signals obtained using the NN near the origin. The measured radial displacement during magnetic suspension in the X- and Y-directions at a speed of 900 rpm is shown in Figs 5.21 (a) and (b), respectively. The RMSEs

between the radial ECD sensors and the proposed sensor system were 13.6 and 12.8 μm in the X- and Y-directions, respectively, slightly larger than the previous error as shown in Table 5.3. However, the rotor experienced instability and failure when operated at higher rotational speeds owing to measurement errors.

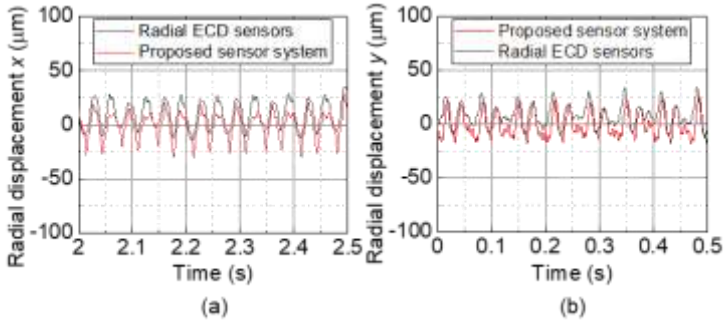


Figure 5.21 Measured radial displacement during displacement feedback control based on the evaluated radial displacement using NN trained by dataset 4 in Table 5.5 at a speed of 900 rpm: (a) X direction; (b) Y direction.

### 5.5.6 Reduction of the number of ECD sensors

In principle, reducing the number of ECD sensors from seven to five is possible. To explore this, ECD sensors $S_4$ and $S_7$ were removed, and their outputs were not included in the NN training. However, the calculated MSE increased to 179 μm$^2$, using the same dataset 1 in Table 5.5. This MSE is significantly higher than the previous MSE, indicating a notable impact on the accuracy of the radial displacement measurement. Figures 22 (a) and (b) show the measurement accuracy of RMSE using different sensor placements at different rotational speeds in the X- and Y-directions, respectively. With the same neural network structure, the measurement accuracy of RMSE of radial displacement using the seven-sensor placement surpasses the measurement accuracy achieved with the five-sensor placement due to sufficient input information. This NN cannot achieve magnetic suspension in the feedback experiments.

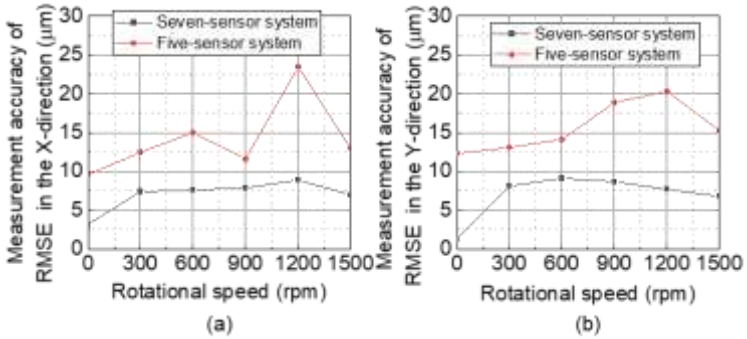


Figure 5.22 (a) Measurement accuracy of RMSE using different sensor systems at different rotational speeds in the X-direction; (b) Measurement accuracy of RMSE using different sensor systems at different rotational speeds in the Y-direction.

To enhance the measurement accuracy and reliability, the number of neurons in the hidden layer was increased from 10 to 4. Consequently, the training time was tripled utilizing the same dataset 1 from Table 5.5, and the calculated MSE decreased to 72.3 $\mu m^2$. Figures 23 (a) and (b) show the comparison of linearity between the proposed seven-sensor system and the proposed five-sensor system with the enhanced NN in the X- and Y-directions, respectively. The maximum error of the linearity measured by the five-sensor system increases from 13.6 μm to 24.4 μm in the X- direction and from 17.1 μm to 27.2 μm in the Y-direction, respectively.

The enhanced NN has facilitated stable magnetic suspension during startup and rotation. Fig. 5.24 (a) depicted the measured radial displacements at a speed of 900 rpm in the X-direction, exhibiting an RMSE of 13.0 μm between the radial ECD sensors and the proposed five-sensor system. However, as the rotational speed increased, the rotor became unstable, as illustrated in Fig. 5.24 (b). Furthermore, the magnetic suspension startup was achieved with an error of 7.1 μm and 5.1 μm in the X- and Y-directions after reaching stability, as shown in Figs. 25 (a) and (b), respectively. Nevertheless, a large oscillation during startup was observed due to measurement error.

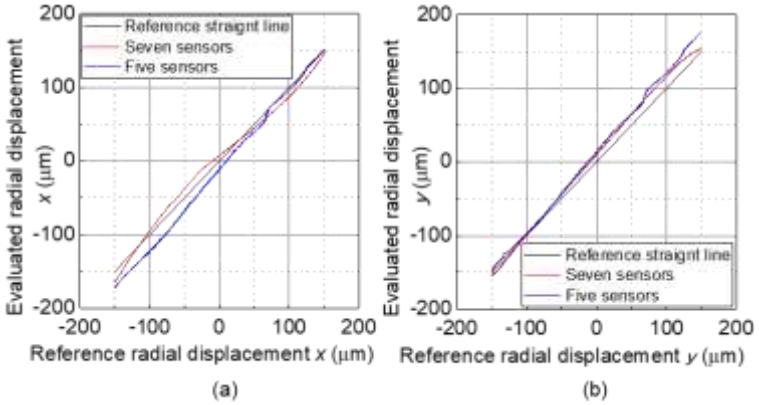


Figure 5.23 Comparison of the sensor linearity between the proposed seven-sensor system and proposed five-sensor system: (a) X direction; (b) Y direction.

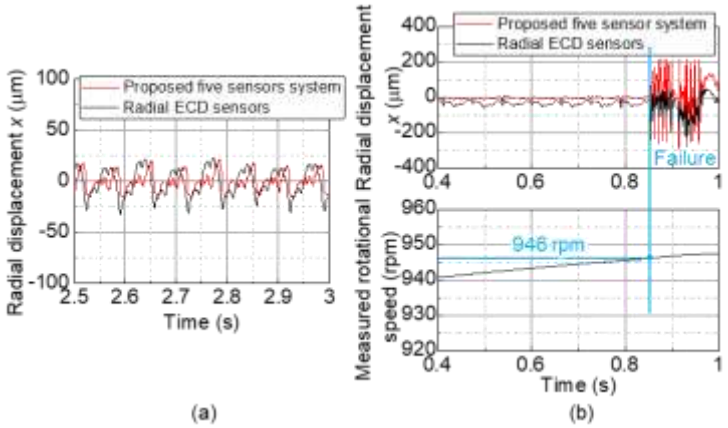


Figure 5.24 Displacement feedback control based on the evaluated radial displacement measured using the proposed five-sensor system: (a) Stable suspension at 900 rpm; (b) Failed suspension when further increasing rotational speed.

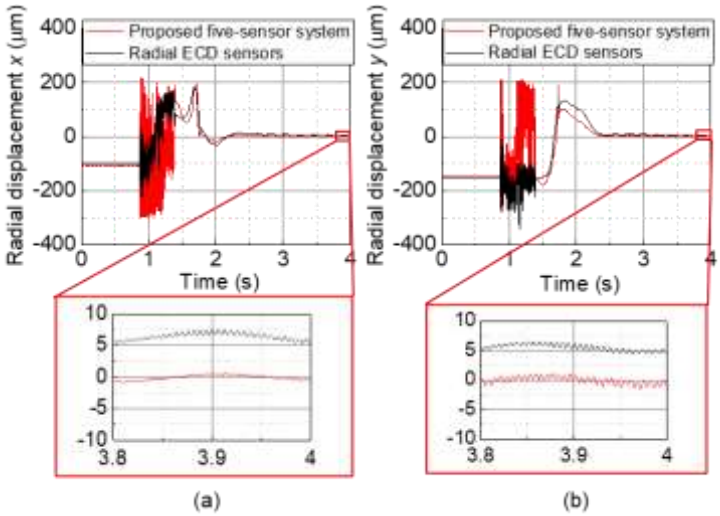


Figure 5.25 Measured radial displacement during displacement feedback control based on the evaluated radial displacement measured using the proposed five-sensor system during magnetic suspension startup: (a) X direction; (b) Y direction.

### 5.5.7 Dataset capture in the commercial application for NN training

In our experiment, the dataset for NN training was captured using radial ECD sensors inside the rotor of the BELSM to calibrate the ECD sensors under the rotor. However, this method does not apply to commercially available CBPs because the radial ECD sensors occupy the inner rotor space, requiring specialized processing of the bottom housing of the pump head. Moreover, after sensor calibration, replacing the bottom housing is necessary, potentially compromising the calibration accuracy and increasing the repetitive work step.

To address this issue, laser displacement sensors can be employed, mounted on the outside of the rotor, to measure the radial displacement of the rotor instead of utilizing radial ECD sensors. The commercially available pump top housing can be removed without a

working fluid to acquire the dataset for NN training. Hammering can then be applied to introduce an impulse force on the rotor during suspension, simulating a wider range of rotor motions and attitudes in place of the hydraulic force in the CBP.

## 5.6 Summary

This chapter proposes the radial displacement measurement method for BELSM by placing the ECD sensors on the underside of the rotor's inner edge. This sensor placement method prevents an increase in rotor height and avoids occupying the inner side of the rotor space, contrasting with conventional placements outside or inside the rotor. An arrangement of seven ECD sensors is proposed to compensate for interference from axial and tilt displacement and nonlinear effects in radial displacement measurements. The relationship between the output voltages of the seven ECD sensors and radial displacement is established using two methods: (1) Polynomial fitting method and (2) NN method. However, the polynomial fitting method cannot meet the measurement accuracy requirements due to the limitation of the sensor calibration precision and the inaccurate assumption. The NN method based on the backpropagation algorithms is proposed to achieve the multiple DOF sensor calibration within the constraint space.

The proposed system arrangement based on the sensor calibration using the NN method shows maximum errors of 13.6 and 17.1 μm in the X- and Y-direction within the ± 150 μm range, respectively. A measured bandwidth of 200 Hz is achieved. Successful radial displacement during magnetic suspension startup and rotation is demonstrated, with RMSE within 16 μm. Increasing the diversity and size of the dataset for NN training can enhance the accuracy of NN fitting. Furthermore, a differentially placed seven-sensor configuration offers higher measurement accuracy than a five-sensor configuration.

In the future, further experiments are crucial to assess the robustness of NN in scenarios where serious measurement errors may arise if the motion and attitude of the rotor are not adequately represented in the dataset for NN training. The ultimate goal is to minimize the number of sensors required for radial displacement measurement. Experiments in section 5.5.6 have revealed that increasing the number of neurons in the hidden layer significantly enhances the fitting accuracy of five ECD sensors. However, a complex NN structure demands substantial hardware computing resources during real-time implementation, increasing training time. Therefore, improving the measurement accuracy while simplifying the NN structure in a five-sensor configuration is necessary.

# Chapter 6 Conclusion

## 6.1 Summary

Aiming to realize the extracorporeal VAD with high durability, high biocompatibility, compact size, and low disposable cost, the disposable CBP utilizing a homopolar BELSM with a PM-free rotor was researched in this thesis. The research consists of two main parts: (1) the development of the CBP utilizing a novel BELSM (Chapters 2-4); (2) the development of a new radial displacement measurement method to improve CBP performance (Chapter 5).

The content of this thesis is summarized as follows:

"Chapter 1 Introduction"

This chapter first introduces the necessity of extracorporeal VAD as a solution for heart failure treatment with the circulatory machine, offering a range of short-term to long-term application options. Based on the application scenarios, the requirements of the blood pump in VAD were presented. Various generations of blood pumps were mentioned, and their respective advantages and disadvantages were discussed.

Nevertheless, none of the commercial blood pumps can fulfill all the requirements simultaneously. Among them, the commonly utilized CentriMag, employing BELSM technology, has faced high disposable costs attributed to the embedded PM in the impeller/rotor. Therefore, using BELSM with a PM-free is the most suitable solution to meet all requirements.

Several developed BELSM with a PM-free were introduced. However, existing BELSM presents challenges, such as insufficient rotational torque and passive stiffness. Therefore, this thesis aims to develop a CBP utilizing a proposed BELSM with a PM-free rotor capable of generating sufficient rotational torque and passive stiffness for blood circulation with artificial lungs, featuring a simple structure, low power consumption, and rotor angle-independent magnetic suspension. Furthermore, the new radial displacement measurement method for BELSM by installing the ECD sensor below the rotor is proposed to improve the CBP performance.

"Chapter 2 Principle and design"

To fulfill the requirements of CBP, this chapter introduces the configuration of the proposed BELSM with a PM-free rotor. The entire structure is similar to the conventional switched reluctance motors. Two PM rings and iron rings are mounted above and below the

stator pole tips, which form a vertical triple-layer magnetic circuit with the rotor structure to provide homopolar flux bias in the air gap.

The working principle of passive stabilization in the axial and tilt directions, radial suspension force generation, and torque generation were explained. Built upon the proposed structure, the BELSM offers the advantages of simple structure, cost-effectiveness flux bias generation, enhanced passive stiffness, PM demagnetization prevention, and angle-independent magnetic suspension.

Based on the previous research, the target of passive stiffness and rotational torque were determined with a rotor diameter of 50 mm. After building the numerical simulation model, the rotor support stiffness, current-force coefficient, and rotational torque were calculated by the FEM simulation. The passive stiffness in the axial and tilt directions were 18.5 N/mm and 5.9 Nm/rad, respectively, far exceeding the target value. The average rotational torque of 0.068 Nm meets the requirement. The angle-independent passive stiffness and suspension force were also verified.

“Chapter 3 Prototype fabrication”

In this chapter, to evaluate the proposed CBP performance, the prototype of the CBP utilizing the proposed BELSM was fabricated, consisting of the proposed BELSM, disposable pump head, electrical system, and controller system.

The BELSM is machined and assembled based on the numerical simulation model. The disposable pump head comprises top and bottom housing made of polyetherimide, along with an integrated waterproof impeller/rotor. The initial priming volume of the pump head is 20 mL.

The radial displacements in the X- and Y-directions were measured by the three ECD sensors mounted at the rotor’s inner side. The rotational speed and rotor angle were measured by the low-sensitivity HE to reduce the signal distortion caused by the large motor current. The linear power and PWM amplifiers were attempted to deliver the command current. However, the noise of the high-voltage PWM causes the HE to measure the rotor angle inaccurately. Therefore, we chose the linear amplifier, but due to heat dissipation problems, it cannot provide a large supply voltage of ±60 V, which results in a lower current-loop bandwidth of 780 Hz.

In the suspension control system, the PID controller was utilized to establish the displacement feedback control and the synchronous disturbance elimination method to suppress the unbalanced vibration. In the rotational control system, the PI controller was used

to achieve speed feedback control, and a rotation signal process was designed to improve the rotor angle measurement.

“Chapter 4 Performance evaluation”

In this chapter, a mock circulatory loop filled with 40wt% aqueous glycerol solution was built to simulate the natural working environment to evaluate the BELSM and CBP performance. The mock circulatory loop consists of the fabricated prototype of the CBP, two pressure gauges, a flowmeter, a reservoir tank, and a clamp.

The suspension performance evaluation was conducted with the outlet fully clamped. The impeller/rotor can achieve magnetic levitation startup and maintain a stable suspended state at the origin. The positioning accuracy at 0 rpm was 14.5 μm and 10.5 μm in the X- and Y-directions, respectively. The bandwidth of the closed-loop feedback system is 61 Hz.

In the rotation performance evaluation, the effect of the motor current on the raw output voltage of HE was reduced by using low-sensitivity HE and designing the rotation signal process. At a speed of 2400 rpm, the maximum accumulated mechanical angle error within one electrical period was approximately 1.1°. Stable rotation from 0 rpm to 2300 rpm 40wt% aqueous glycerol solution was successfully achieved. Based on the synchronous disturbance elimination method, the maximum vibration amplitudes of the impeller/rotor were less than 100μm, which was within 50% of the fluid gap.

In the pump performance evaluation, the maximum head pressure and flow rate achieved were 214.5 mmHg and 4.59 L/min at 2400 rpm and 2300 rpm, respectively. The power consumption of the proposed BELSM was measured with different rotational speeds and flow rates. The maximum pump efficiency reached 5.3% at a speed of 2300 rpm with a flow rate of 4.48 L/min.

The inability to achieve the targeted hydraulic performance is attributed to the rotational speed limitation, resulting from the lower current-loop bandwidth of 780 Hz that hinders the actual current from following the reference current. The main reason for the lower current-loop bandwidth is insufficient output voltage ±60 V from the linear power amplifiers due to temperature limitations.

“ Chapter 5 Radial displacement measurement using ECD sensors below the rotor”

This chapter proposes a new radial displacement measurement by installing the ECD sensors under the inner edge of the rotor bottom to remove the ECD sensor from the inner side

of the rotor bottom. This proposed sensor placement can avoid increasing the rotor's height and simplify the secondary flow within the pump head to improve the CBP performance.

However, ECD sensors at that location make obtaining highly accurate radial displacement challenging due to interference from multiple-DOF displacement and nonlinear effects on the ECD sensor output. Therefore, a seven-ECD sensor arrangement is proposed to solve this problem, and two methods are proposed to realize the multiple-DOF seven sensors calibration: (1) polynomial fitting method and (2) NN method.

However, the polynomial fitting method leads to large measurement errors of 44 μm. To further improve the accuracy, the feedforward NN based on a backpropagation algorithm was used to establish the relationship between the output voltages of the seven ECD sensors and the radial displacement of the rotor. The measured linearity based on the NN method demonstrated maximum errors of 13.6 μm and 17.1 μm in the X- and Y-directions, respectively, within the range of ±150 μm. A measured bandwidth of 200 Hz was achieved. Furthermore, successful radial displacement feedback control was implemented during magnetic suspension startup and rotation, resulting in an RMSE within 16 μm.

The influence of the dataset and the number of ECD sensors on the measurement accuracy were discussed. Increasing the diversity and size of the dataset for NN training holds the potential to improve measurement accuracy. Moreover, a seven-ECD sensor configuration provides superior measurement accuracy and sensitivity compared to a five-ECD sensor configuration.

## 6.2 Future plan

6.2.1 Improvement of the rotational speed to achieve targeted performance

(1) Improvement of current-loop bandwidth

In the pump performance evaluation outlined in Chapter 4, challenges are encountered in achieving the required hydraulic performance due to the rotational speed limitation. This limitation results from the relatively lower current-loop bandwidth. As detailed in Chapter 4, two methods are proposed to improve the current-loop bandwidth: (1) Reduction in power dissipation by using the positive-negative phase current commutation method to improve the input voltage of the linear power amplifier; (2) Reduction in coil inductance by decreasing the number of the turns of the coil to enhance current response.

(2) Improvement of rotor angle measurement

Chapter 4 presented a maximum accumulated mechanical error of 1.1° within one electrical period. However, the measured rotor angle by the HE is not compared with the reference value measured by the encoder to evaluate the measurement accuracy. The measurement accuracy and compensation method need to be discussed for rotational torque improvement in the future.

Furthermore, at higher rotational speeds, the large motor current will cause more severe distortion to the output of the HE. Therefore, alternative methods for rotor angle measurement, such as introducing a groove from the bottom of the rotor and measuring the rotor angle from the rotor bottom or employing a sensorless measurement method, should be explored to either measure or compensate for errors.

### 6.2.2 Improvement of the displacement estimation based on the NN method

(1) Reduction of the number of the ECD sensors

The five-ECD sensors configuration is preferred, considering the cost. The influence of the number of ECD sensors on measurement accuracy was discussed in Chapter 5. The measurement accuracy of NN can be increased by increasing the number of NN neurons. However, the complex NN structure will occupy many computing hardware resources when implemented in real-time. Therefore, simplifying the NN structure as much as possible while ensuring measurement accuracy must be considered.

The relationship between multiple sensor outputs and two radial displacements in the NN fitting process was established. In principle, the multiple sensors should be divided into two channels, one for measuring axial displacement and the tilt angle for interference compensation. The other is used to measure radial displacement directly. In the future, the convolutional NN structure and design of the kernel to capture information in two channels will be considered, thereby simplifying the structure of the hidden layer.

(2) Robustness of the NN in the actual VAD use cases

In Chapter 5, a discussion of the impact of datasets on NN was conducted. The diversity and size of the dataset is very important for the fitting accuracy of the NN. In actual VAD use cases, the rotor may be impacted and disturbed, potentially exceeding the motion range covered by the dataset, resulting in unknown NN outputs.

Thus, further experimental investigations are necessary to evaluate the robustness of the NN in such cases. Furthermore, the relationship between the dataset for NN training and the robustness of the NN needs to be investigated.

### 6.2.3 Other improvements of the CBP utilizing the BELSM

(1) Reduction of the number of the amplifiers

In the prototype CBP, the combined windings were used, that flow through the suspension current and the rotation current, causing the requirements of twelve power amplifiers to implement energy transmission. In the future, separate windings consisting of suspension windings and rotation windings will be considered to reduce the number of power amplifiers.

(2) Displacement sensorless measurement

Although the new radial displacement measurement method of installing the ECD sensors under the rotor enables the BELSM to achieve a central hollow design, it increases the number of eddy current sensors used and increases the cost. In the future, sensorless displacement control will be considered.

(3) BELSM miniaturization

Compared with the CentriMag depicted in Figu. 1.5, the CBP prototype utilizing the proposed BELSM exhibits a slightly larger size. To enhance portability, future optimizations can be made to the BELSM's structure, and parameters, aiming to further reduce its overall dimensions.

(4) Biocompatibile improvement

After removing the internal sensor system, the smoother secondary flow path will be redesigned to reduce hemolysis and thrombus formation. At the same time, the geometrical structure of the impeller will be optimized to minimize the area of turbulence. Finally, biocompatible coatings will be used to further reduce platelet adhesion and thrombus formation.

# References


[1] Our World in Data, Key insights on causes of death, https://ourworldindata.org/causes-of-death.

[2] Specified report of vital statistics in 2022 from the Ministry of Heart, Labour and Welfare, https://www.mhlw.go.jp/toukei/saikin/hw/jinkou/kakutei22/dl/11_h7.pdf.

[3] A. Sadik, M. Yousif, and J. C. McElnay, "Pharmaceutical care of patients with heart failure," *British Journal of Clinical Pharmacology*, vol. 60, no. 2, pp. 183-193, 2005.

[4] G. M. S. da Silva, M. C. Chambela, A.S. Sousa *et al*., "Impact of pharmaceutical care on the quality of life of patients with Chagas disease and heart failure: randomized clinical trial," *Trials*, vol. 13, no. 1, pp. 1-7, 2012.

[5] E. B. Friedrich and M. Böhm, "Management of end stage heart failure," *Heart*, vol. 93, no. 5, pp. 626-631, 2007.

[6] H. Parissis, V. Graham, S. Lampridis, *et al*., "IABP: history-evolution-pathophysiology-indications: what we need to know," *Journal of Cardiothoracic Surgery*, vol. 11, no. 1, pp. 1-13, 2016.

[7] J. D. Dedhia, K. R. N. Chakravarthy, and A.B. Ahmed, "Intra aortic balloon pump (IABP): past, present and future," *Indian Journal of Anaesthesia*, vol. 52, no. 4, pp. 387-396, 2008.

[8] R. P. Barbaro, G. MacLaren, P. S. Boonstra, *et al*., "Extracorporeal membrane oxygenation for COVID-19: evolving outcomes from the international Extracorporeal Life Support Organization Registry," *The Lancet*, vol. 398, no. 10307, pp. 1230-1238, 2021.

[9] K. Ramanathan, D. Antognini, A. Combes *et al*., "Planning and provision of ECMO services for severe ARDS during the COVID-19 pandemic and other outbreaks of emerging infectious diseases," *The Lancet Respiratory Medicine*, vol. 8, no. 5, 2020.

[10] J. A. Cook , K. B. Shah, M. A. Quader *et al*., "The total artificial heart," *Journal of Thoracic Disease*, vol. 7, no. 12, pp. 2172-2180, 2015.

[11] N. A.Gray Jr and C. H. Selzman, "Current status of the total artificial heart," *American Heart Journal*, vol. 152, no. 1, pp. 4-10, 2006.

[12] T. C. Hanff and E. Y. Birati, "Left ventricular assist device as destination therapy: a state of the science and art of long-term mechanical circulatory support," *Current Heart Failure Reports*, vol. 16, pp. 168-179, 2019.

[13] H. Tunuguntla, J. Conway, C. Villa *et al*., "Destination-therapy ventricular assist device in children: "the future is now"," *Canadian Journal of Cardiology*, vol. 36, no. 2, pp. 216-222, 2020.

[14] E. Tayama, K. Takagi, T. Shojima *et al*., "Review of Implantable Left Ventricular Assist Devices," *The Kurume Medical Journal*, vol. 68, no. 3.4, pp. 171-181, 2021.

[15] P. Kurtyka, R. Kustosz, M. Kaczmarek *et al*., "Surface modifications for inflow cannulas of ventricular assist devices–comparison of latest solutions," *Engineering of Biomaterials*, vol. 22, no. 151, pp. 17-23, 2019.

[16] S. Kadakia, R. Moore, V. Ambur, *et al*., "Current status of the implantable LVAD," *General Thoracic and Cardiovascular Surgery*, vol. 64, pp. 501-508, 2016.

[17] S. G. Drakos, A. G. Kfoury, J. Stehlik *et al*., "Bridge to recovery: understanding the disconnect between clinical and biological outcomes," *Circulation*, vol. 126, no. 2, pp. 230-241, 2012.

[18] E. A. Ziemba and R. John, "Mechanical circulatory support for bridge to decision: which device and when to decide," *Journal of Cardiac Surgery*, vol. 25, no. 4, pp. 425-433, 2010.

[19] F. De Robertis, P. Rogers, M. Amrani, *et al*., "Bridge to decision using the Levitronix CentriMag short-term ventricular assist device," *The Journal of Heart and Lung Transplantation*, vol. 27, no. 5, pp. 474-478, 2008.

[20] A. L. Zhou, E. W. Etchill, K. A. Giuliano, *et al*., "Bridge to transplantation from mechanical circulatory support: a narrative review," *Journal of Thoracic Disease*, vol. 13, no. 12, pp. 6911-6923, 2021.

[21] P. M. Portner, P. E. Oyer, D. G. Pennington, *et al*., "Implantable electrical left ventricular assist systems: Bridge to transplantation and future," *The Annals of Thoracic Surgery*, vol. 47, no. 1, pp. 142-150, 1989.

[22] F. L. Delmonic, "The implications of Istanbul Declaration on organ trafficking and transplant tourism," *Current Opinion in Organ Transplantation*, vol. 14, no. 2, pp. 116-119, 2009.

[23] G. M. Danovitch and M. Al-Mousawi, "The Declaration of Istanbul—early impact and future potential," *Nature Reviews Nephrology*, vol. 8, no. 6, pp. 358-361, 2012.

[24] A. Akabayashi, E. Nakazawa, R. Ozeki-Hayashi *et al*., "Twenty years after enactment of the organ transplant law in Japan: why are there still so few deceased donors?" *Transplantation Proceeding*, vol. 50, no. 5, pp. 1209-1219, 2018.

[25] 社団法人日本臓器移植ネットワーク, 臓器提供数/移植数, 移植希望登録者数, https://www.jotnw.or.jp/

[26] A. P. W. M. Maat, R. J. van Thie, M. Dalinghaus *et al*., "Connecting the Centrimag Levitronix pump to Berlin Heart Excor cannulae; a new approach to bridge to bridge," *The Journal of Heart and Lung Transplantation*, vol. 27, no. 1, pp. 112-115, 2008.

[27] I. D. Gregoric, L. P. Jacob, S. La Francesca *et al*., "The TandemHeart as a bridge to a long-term axial-flow left ventricular assist device (bridge to bridge)," *Texas Heart Institute Journal*, vol. 35, no. 2, p. 125, 2008.

[28] M. Nishida, R. Kosaka, O. Maruyama *et al*., "Long-term durability test of axial-flow ventricular assist device under pulsatile flow," *Journal of Artificial Organs*, vol. 20, pp. 26-33, 2017.

[29] E. J. Molina and S. W. Boyce, "Current status of left ventricular assist device technology," *Seminars in Thoracic and Cardiovascular Surgery*, vol. 25, no. 1, pp. 56-63, 2013.

[30] C. A. Papanastasiou, K. G. Kyriakoulis, C. A. Theochari *et al*., "Comprehensive review of hemolysis in ventricular assist devices," *World Journal of Cardiology*, vol. 12, no. 7, p. 334, 2020.

[31] A. M. Gouskov, V. O. Lomakin, E. P. Banin E *et al*., "Assessment of hemolysis in a ventricular assist axial flow blood pump," *Biomedical Engineering*, vol. 50, pp. 233-236, 2016.

[32] P. M. Eckman and R. John, "Bleeding and thrombosis in patients with continuous-flow ventricular assist devices," *Circulation*, vol. 125, no. 24, pp. 3038-3047, 2012.

[33] P. M. Portner, P. G. M. Jansen, P. E. Oyer *et al*., "Improved outcomes with an implantable left ventricular assist system: a multicenter study," *The Annals of Thoracic Surgery*, vol. 71, no. 1, pp. 205-209, 2001.

[34] B. H. Chong, "Heparin-induced thrombocytopenia," *Journal of Thrombosis and Haemostasis*, vol. 1, no. 7, pp. 1471-1478, 2003.

[35] N. Morici, M. Varrenti, D. Brunelli *et al*., "Antithrombotic therapy in ventricular assist device (VAD) management: From ancient beliefs to updated evidence. A narrative review," *IJC Heart & Vasculature*, vol. 20, pp. 20-26, 2018.

[36] H. W. Chang, J. Nam, J. H. Cho *et al*., "Five-year experience with mini-volume priming in infants≤ 5 kg: safety of significantly smaller transfusion volumes," *Artificial Organs*, vol. 38, no. 1, pp. 78-87, 2014.

[37] V. Gournay and Q. Hauet, “Mechanical circulatory support for infants and small children,” *Archives of Cardiovascular Diseases*, vol. 107, no.6-7, pp. 398-405, 2014.

[38] K. Kido, H. Hoshi, N. Watanabe *et al*., “Computational fluid dynamics analysis of the pediatric tiny centrifugal blood pump (TinyPump),” *Artificial Organs*, vol. 30, no. 5, pp. 392-399, 2006.

[39] J. W. Stokes, W. D. Gannon, Y. Tipograf *et al*., “Disposable component selection in extracorporeal life support: a cost analysis,” *ASAIO Journal*, vol. 67, no. 9, pp. 995-999, 2021.

[40] J. J. Curtis, J. T. Walls, C. C. Wagner-Mann *et al*., “Centrifugal pumps: description of devices and surgical techniques,” *The Annals of Thoracic Surgery*, vol. 68, no. 2, pp. 666-671, 1999.

[41] C. A. Thunberg, B. D. Gaitan, F. A. Arabia *et al*., “Ventricular assist devices today and tomorrow,” *Journal of Cardiothoracic and Vascular Anesthesia*, vol. 24, no. 4, pp. 656-680, 2010.

[42] H. Hoshi, T. Shinshi and S. Takatani, “Third-generation blood pumps with mechanical noncontact magnetic bearings,” *Artificial Organs*, vol. 30, no. 5, pp. 324-338, 2006.

[43] I. Köhne, “Review and reflections about pulsatile ventricular assist devices from history to future: concerning safety and low haemolysis—still needed,” *Journal of Artificial Organs*, vol. 23, pp. 303-314, 2020.

[44] S. D. Moulopoulos, S. Topaz and W. J. Kolff, “Diastolic balloon pumping (with carbon dioxide) in the aorta—a mechanical assistance to the failing circulation,” *American Heart Journal*, vol. 63, no. 5, pp. 669-675, 1962.

[45] M. E. DeBakey, “Development of mechanical heart devices,” *The Annals of Thoracic Surgery*, vol. 79, no. 6, pp. S2228-S2231, 2005.

[46] H. Takano H and T. Nakatani, “Ventricular assist systems: experience in Japan with Toyobo pump and Zeon pump,” *The Annals of Thoracic Surgery*, vol. 61, no. 1, pp. 317-322, 1996.

[47] K. Kashiwa, T. Nishimura, A. Nakahata *et al*., “Survey of blood pump diaphragm damage in the NIPRO-ventricular assist device,” *Journal of Artificial Organs*, vol. 15, pp. 341-346, 2012.

[48] S. Whittaker and C. Glanville, “The Thoratec® ventricular assist device system,” *Perfusion*, vol. 15, no. 4, pp. 363-368, 2000.

[49] G. K. Jett, “ABIOMED BVS 5000: experience and potential advantages,” *The Annals of Thoracic Surgery*, vol. 61, no. 1, pp. 301-304, 1996.

[50] W. J. Weiss, “Pulsatile pediatric ventricular assist devices,” *ASAIO Journal*, vol. 51, no. 5, pp. 540-545, 2005.

[51] D. R. Wheeldon, P. G. M. Jansen, and P. M. Portner, “The Novacor electrical implantable left ventricular assist system,” *Perfusion*, vol. 15. No. 4, pp. 355-361, 2000.

[52] J. Cowger, F. D. Pagani, J. W. Haft *et al*., “The development of aortic insufficiency in left ventricular assist device-supported patients,” *Circulation: Heart Failure*, vol. 3, no. 6, pp. 668-674, 2010.

[53] S. W. Pak, N. Uriel, H. Takayama *et al*., “Prevalence of de novo aortic insufficiency during long-term support with left ventricular assist devices,” *The Journal of Heart and Lung Transplantation*, vol. 29, no. 10, pp. 1172-1176, 2010.

[54] S. Crow S, R. John R, A. Boyle *et al*., “Gastrointestinal bleeding rates in recipients of nonpulsatile and pulsatile left ventricular assist devices,” *The Journal of Thoracic and Cardiovascular Surgery*, vol. 137, no. 1, pp. 208-215, 2009.

[55] O. H. Frazier, E. A. Rose, Q. Macmanus *et al*., “Multicenter clinical evaluation of the HeartMate 1000 IP left ventricular assist device,” *The Annals of Thoracic Surgery*, vol. 53, no. 6, pp. 1080-1090, 1992.

[56] E. V. Potapov, Y. Weng, T. Drews *et al*., “Longest time of support by the Novacor left ventricular assist device without pump exchange,” *The Annals of Thoracic Surgery*, vol. 80, no. 6, p. 2421, 2005.

[57] G. Faggian, F. Santini, G. Franchi *et al*., “Insights from continued use of a novacor left ventricular assist system for a period of 6 years,” *The Journal of Heart and Lung Transplantation*, vol. 24, no. 9, pp.1444.e17-1444.e19, 2005.

[58] G. P. Noon, J. W. Ball Jr, and H. T. Papaconstantinou, “Clinical experience with BioMedicus centrifugal ventricular support in 172 patients,” *Artificial Organs*, vol. 19, no. 7, pp. 756-760, 1995.

[59] Y. Guan, X. Su, R. McCoach R *et al*., “Mechanical performance comparison between RotaFlow and CentriMag centrifugal blood pumps in an adult ECLS model,” *Perfusion*, vol. 25, no. 2, pp. 71-76, 2010.

[60] T. Yamane, R. Kosaka, M. Nishida *et al*., "Enhancement of hemocompatibility of the MERA monopivot centrifugal pump: toward medium-term use," *Artificial Organs*, vol. 37, no. 2, pp. 217-221, 2013.

[61] X. Song, A. L. Throckmorton, H. G. Wood *et al*., "Quantitative evaluation of blood damage in a centrifugal VAD by computational fluid dynamics," *The Journal of Fluids Engineering*, vol. 126, no. 3, pp. 410-418, 2004.

[62] M. Hosseinipour, R. Gupta, M. Bonnell *et al*., "Rotary mechanical circulatory support systems," *Journal of Rehabilitation and Assistive Technologies Engineering*, vol. 4, 2055668317725994, 2017.

[63] M. V. Denisov, D. V. Telyshev, S. V. Selishchev *et al*., "Investigation of hemocompatibility of rotary blood pumps: The case of the sputnik ventricular assist device," *Biomedical Engineering*, vol. 53, pp. 181-184, 2019.

[64] H. Heshmat, A. Z. Hunsberger, S. Jahanmir *et al*., "Prediction of hydrodynamic bearing performance for cardiac assist devices," *ASAIO Journal*, vol. 52, no. 2, 51A, 2006.

[65] H. Sumikura, K. Fukunaga, A. Funakubo *et al*., "Development of an axial flow blood pump with hydrodynamic conical bearings," *ASAIO Journal*, vol. 51, no. 2, 34A, 2005.

[66] P. Khanwilkar, D. Olsen, G. Bearnson *et al*., "Using hybrid magnetic bearings to completely suspend the impeller of a ventricular assist device," *Artificial Organs*, vol. 20, no. 5, pp. 597-604, 1996.

[67] W. Hijikata, T. Shinshi, J. Asama *et al*., "A magnetically levitated centrifugal blood pump with a simple-structured disposable pump head," *Artificial Organs*, vol. 32, no. 7, pp. 531-540, 2008.

[68] A. Chatterjee, C. Feldmann, G. Dogan *et al*., "Clinical overview of the HVAD: a centrifugal continuous-flow ventricular assist device with magnetic and hydrodynamic bearings including lateral implantation strategies," *Journal of Thoracic Disease*, vol. 10(Suppl 15), p. S1785, 2018.

[69] R. Wampler, D. Lancisi, V. Indravudh *et al*., "A sealless centrifugal blood pump with passive magnetic and hydrodynamic bearings," *Artificial Organs*, vol. 23, no. 8, pp. 780-784, 1999.

[70] D. B. Olsen, G. Bramm and P. Novak, "Magnetically suspended and rotated impellor pump apparatus and method," U.S. Patent 4688998, Aug. 25, 1987.

[71] J. C. Moise, “Magnetically suspended rotor axial flow blood pump,” U.S. Patent 4779614, Oct. 25, 1988.

[72] T. Akamatsu, T. Nakazeki and H. Itoh, “Centrifugal blood pump with a magnetically suspended impeller,” *Artificial Organs*, vol. 16, no. 3, pp. 305-308, 1992.

[73] R. Schoeb, J. Hugel and N. Mendler, “Rotary machine with an electromagnetic rotary drive,” U.S. Patent 6100618, Aug. 8, 2000.

[74] O. Borisenko, G. Wylie, J. Payne *et al*., “Thoratec CentriMag for temporary treatment of refractory cardiogenic shock or severe cardiopulmonary insufficiency: a systematic literature review and meta-analysis of observational studies,” *Asaio Journal*, vol. 60, no. 5, p. 487, 2014.

[75] A. Tschirkov, D. Nikolov and V. Papantchev, “New technique for implantation of the inflow canula of Berlin Heart INCOR system,” *European Journal of Cardio-thoracic Surgery*, vol. 30, no. 4, pp. 678-679, 2006.

[76] H. M. Loree, K. Bourque, D. B. Gernes *et al*., “The Heartmate III: design and in vivo studies of a maglev centrifugal left ventricular assist device,” *Artificial Organs*, vol. 25, no. 5, pp. 386-391, 2001.

[77] T. Someya, M. Kobayashi, S. Waguri *et al*., “Development of a disposable maglev centrifugal blood pump intended for one-month support in bridge-to-bridge applications: in vitro and initial in vivo evaluation,” *Artificial Organs*, vol. 33, no. 9, pp. 704-713, 2009.

[78] R. Schoeb and N. Barletta, “Principle and application of a bearingless slice motor,” *JSME International Journal Series C Mechanical Systems, Machine Elements and Manufacturing*, vol. 40, no. 4, pp. 593-598, 1997.

[79] R. Schöb, N. Barletta, and J. Hahn, “The Bearingless centrifugal pump-A perfect example of a mechatronics system,” *IFAC Proceedings Volumes*, vol. 33, no. 26, pp. 443-448, 2000.

[80] B. S. Weinreb, M. Noh, D. C. Fyler *et al*., “Design and implementation of a novel interior permanent magnet bearingless slice motor,” *IEEE Transactions on Industry Applications*, vol. 57, no. 6, pp. 6774-6782, 2021.

[81] C. H. H. Chan, I. L. Pieper, R. Hambly *et al*., “The CentriMag centrifugal blood pump as a benchmark for in vitro testing of hemocompatibility in implantable ventricular assist devices,” *Artificial Organs*, vol. 39, no. 2, pp. 93-101, 2015.

[82] O. Borisenko, G. Wylie, J. Payne *et al*., “The cost impact of short-term ventricular assist devices and extracorporeal life support systems therapies on the National Health Service in the UK,” *Interactive Cardiovascular and Thoracic Surgery*, vol. 19, no. 1, pp. 41-48, 2014.

[83] I. Bouchareb, A. Bentounsi and A. Lebaroud, “A comparative study of synchronous reluctance and switched reluctance motors for high-performance fault-tolerant applications,” *International Journal of Applied Electromagnetics and Mechanics*, vol. 39, no.1-4, pp. 793-799, 2012.

[84] D. A. Staton, W. L. Soong and T. J. E. Miller, “Unified theory of torque production in switched reluctance and synchronous reluctance motors,” *IEEE Transactions on Industry Applications*, vol. 31, no. 2, pp. 329-337, 1995.

[85] W. Gruber and K. Radman, “Modeling and realization of a bearingless flux-switching slice motor,” *Actuators*, vol. 6, no. 2, p. 12, 2017.

[86] W. Gruber, M. Rothböck and R. T. Schöb, “Design of a novel homopolar bearingless slice motor with reluctance rotor,” *IEEE Transactions on Industry Applications*, vol. 51, no. 2, pp. 1456-1464, 2014.

[87] M. Noh and D. L. Trumper, “Homopolar bearingless slice motor with flux-biasing halbach arrays,” *IEEE Transactions on Industrial Electronics*, vol. 67, no. 9, pp. 7757-7766, 2019.

[88] T. Holenstein T, M, Schuck and J. W. Kolar, “Performance benchmarking of a novel magnet-free bearingless synchronous reluctance slice motor,” *IEEE Open Journal of the Industrial Electronics Society*, vol. 1, pp. 184-193, 2020.

[89] J. Rao, W. Hijikata, and Shinshi T, “A bearingless motor utilizing a permanent magnet free structure for disposable centrifugal blood pumps,” *Journal of Advanced Mechanical Design, Systems, and Manufacturing*, vol . 9, no. 3, JAMDSM0046-JAMDSM0046, 2015.

[90] K. Raggl, T. Nussbaumer and J. W. Kolar, “Comparison of separated and combined winding concepts for bearingless centrifugal pumps,” *Journal of Power Electronics*, vol. 9, no. 2, pp. 243-258, 2009.

[91] H. Hofer, M. Nikowitz and M. Schrödl, “Comparative analysis of salient pole and flux barrier rotor for synchronous reluctance machines including flux weakening range,” *The Journal of Engineering*, no. 17, pp. 4055-4059, 2019.

[92] R. Constancias, I. Rasoanarivo, N. Takorabet *et al*., “Design and optimization of a synchronous reluctance machine with salient poles and flux barriers,” *IEEE Energy Conversion Congress and Exposition*, Atlanta, GA, USA, 2010, pp. 2672-2678.

[93] A. Seshadri and N. C. Lenin, “Review based on losses, torque ripple, vibration and noise in switched reluctance motor,” *IET Electric Power Applications*, vol. 14, no. 8, pp. 1311-1326, 2020.

[94] W. Gruber, W. Bauer and K. Radman, “Comparison of homopolar and heteropolar bearingless reluctance slice motor prototypes,” *Proceedings of the Institution of Mechanical Engineers, Part I: Journal of Systems and Control Engineering*, vol. 231, no. 5, pp. 339-347, 2017.

[95] T. Yamane, “Mechanism of artificial heart,” Japan: Springer, 2016.

[96] W. Hijikata, T. Shinshi, A. Shimokohbe *et al*., “Disposable MagLev centrifugal blood pump utilizing cone-shaped impeller,” *IEEE/ASME International Conference on Advanced Intelligent Mechatronics*, Xi’an, Shanxi, China, 2008, pp. 570-575.

[97] K. Lehle, A. Philipp, T. Müller *et al*., “Flow dynamics of different adult ECMO systems: a clinical evaluation,” *Artificial Organs*, vol. 38, no. 5, pp. 391-398, 2014.

[98] J. Asama, T. Fukao, A. Chiba *et al*., “A design consideration of a novel bearingless disk motor for artificial hearts,” *IEEE Energy Conversion Congress and Exposition*, San Jose, CA, USA, 2009, pp. 1693-1699.

[99] T. Fujiwara, E. Nagaoka, T. Watanabe *et al*., “New Generation Extracorporeal Membrane Oxygenation With Med Tech Mag-Lev, a Single-Use, Magnetically Levitated, Centrifugal Blood Pump: Preclinical Evaluation in Calves,” *Artificial Organs*, vol. 37, no. 5, pp. 447-456, 2013.

[100] Y. Takami, T. Nakazawa, K. Makinouchi, *et al*., “Hemolytic effect of surface roughness of an impeller in a centrifugal blood pump,” *Artificial Organs*, vol. 21, no. 7, pp. 686-690, 1997.

[101] M. Nishida, K. Nakayama, D. Sakota *et al*., “Effect of Impeller Geometry on Lift-Off Characteristics and Rotational Attitude in a Monopivot Centrifugal Blood Pump,” *Artificial Organs*, vol. 40, no. 6, pp. E89-E101, 2016.

[102] M. Nishida, T. Yamane, T. Orita *et al*., “Quantitative visualization of flow through a centrifugal blood pump: Effect of washout holes,” *Artificial Organs*, vol. 21, no. 7, pp. 720-729, 1997.

[103] Y. Wakisaka, Y. Taenaka, E. Tatsumi *et al*., “Improvement in antithrombogenicity in a centrifugal pump with self washout structure for long-term use,” *ASAIO Journal*, vol. 41, no. 3, pp. M350-M355, 1995.

[104] H. Granberg, “Linear amplifiers for mobile operations. Motorola RF, Motorola, Phoenix, Arizona, Data Manual, AN-762, 1980, 2: 40-48.

[105] S. Boumaiza and F. M. Ghannouchi, “Thermal memory effects modeling and compensation in RF power amplifiers and predistortion linearizers,” IEEE *Transactions on Microwave Theory and Techniques*, vol. 51, no. 12, pp. 2427-2433, 2003.

[106] E. Gaalaas, “Class d audio amplifiers: What, why, and how,” *Analog Dialogue*, vol. 40, no. 6, pp. 1-7, 2006.

[107] A. Chiba, T. Fukao, O. Ichikawa *et al*., “Magnetic bearings and bearingless drives,” Elsevier, 2005.

[108] X. Zhang, T. Shinshi, L. Li *et al*., “A combined repetitive control for precision rotation of magnetic bearing,” *Precision Engineering*, vol. 27, no. 3, pp. 273-282, 2003.

[109] R. Y. S. Lai and L. Cheng-Ming, “Added mass of a spheriod oscillating in a linearly stratified fluid,” *International Journal of Engineering Science*, vol. 19, no. 11, pp. 1411-1420, 1981.

# Acknowledgement

I would like to personally thank the following people who supported me with my sincere gratitude.

First, I want to express my sincere gratitude to my supervisor: Prof. Tadahiko Shinshi of Future Interdisciplinary Research of Science and Technology (FIRST), Tokyo Institute of Technology (Tokyo Tech), for allowing me to enter his laboratory six years ago. Throughout these six years, he not only instructed me on how to publish papers but also illuminated the path to becoming a proficient researcher and engineer, imparting valuable skills in problem analysis and resolution. Prof. Shinshi spent a lot of effort to guide my research and often taught me how to overcome problems. One of his statements that resonated deeply with me was: "A good researcher needs to be trusted. Trust is easy to lose, but difficult to accumulate." This wisdom made me reflect on the responsibility I bear towards myself and others in both academic pursuits and life. The Shinshi Laboratory has been a witness to my growth, and I am sincerely thankful to Prof. Shinshi for his patient mentorship. I will also keep these important points in mind in my future work and life.

In addition to Prof. Shinshi, I express my sincere gratitude to the other esteemed members of the jury: Prof. Kazuhiro Yoshida, Prof. Yusuke Sugahara, Prof. Takashi Nishisako, and Prof. Wataru Hijikata from the Department of Mechanical Engineering, Tokyo Tech, for their thorough evaluation of this work.

Moreover, within the laboratory, my gratitude extends toAssistant Professor Dr. Naohiro Sugita of FIRST, Dr. Shingo Tajima of FIRST, Dr. Zhong Jianpeng (currently a researcher at the Zhongfa Institute of Aeronautics and Astronautics, Beihang University), and Dr. Han (currently a doctoral supervisor at Zhejiang University). They provided valuable help in research, employment, and life, but also gave me a lot of encouragement. Special appreciation goes to Dr. Sugita for his assistance in article revisions and unwavering encouragement during moments of confusion. Additionally, Dr. Han, even after returning to China, continued to care about my research progress and graduation status via the phone, offering valuable guidance. Besides, I would also like to express my gratitude to the laboratory secretary, Ms. Naoko Muryobayashi, for her substantial assistance in laboratory operations, procurement, organizing business trips, and more.

A heartfelt appreciation goes to the senior members of the laboratory for their invaluable assistance: Dr. WataruTsunoda, Dr. Tadashi Hama, Dr. Mohd Nazmin Maslan, Mr. Noriei

Azuma, Mr. Yoshiki Nagira, Mr Liren Xu, Mr. Daisuke Tabata, Mr. Daiki Sakai and Mr. Yudai Suzuki. Dr. Tunoda gave me research guidance and helped me a lot when I first entered the Shinshi laboratory and aided in my assimilation into both the laboratory and life in Japan. I admire his attitude towards life and research. Dr. Hama joked with me and left me a lot of books to study. Mr. Nagira held parties on the weekend to relax and taught me how to play snowboard. Mr. Akeno is a very serious and rigorous person and helped me a lot with my coursework. Mr. Yamamoto not only helped me with my research but also discussed related hobbies with me, such as soccer and animation.

Additionally, I extend my sincere gratitude to the junior members of the laboratory for their valuable assistance: Dr. Rina Nishida, Dr. Chao Qi, Mr. Keita Nagai, Mr. Zeqiang He, Mr. Makoto KINE, Mr. Tim BIEREWIRTZ, Mr. Junsyo Kanashima, Mr. Bo Yuan, Mr. Taichi Oshino, Mr. Shinya Yamamoto, Mr. Nasaya Sato, Mr. Ziteng Wang, Mr. Junseok An, Mr. Ryo Watabe, Mr. Riku Fukazawa, Ms. Rinka Matsui, Mr. Yasukawa Kimura, Mr. Yohei Hamaoka, Mr. Keita Tomioka, Mr. Minoru Tomioka, Mr. Ryoshi MATSUI, Mr. Yusuke Yamasaki, Mr. Takahiro Ito, Mr. Alif and exchange student Mr. Baptiste MOISAN, who made me spend a happy life in the lab. Dr. Nishida is very enthusiastic to help me solve many research or presentation problems. Dr. Qi is a very rigorous and careful researcher, and I can get a lot of opinions on research and arrangements from him. Mr. He and I are in the same research group, and he is a very talented researcher who was able to give me a lot of technical advice. Mr. Kanashima helped me solve a lot of problems with making phone appointments for medical appointments. Mr. Nagai gave me a lot of reminders on the final submission of graduation materials.

I thank Dr. Siyu Zhou, Ms. Zhiyi Zhou, Ms. Xinyue YU, Mr. Yipeng Cheng, Mr. Ruofei YANG, Ms. Aichiroude Yu and Mr. Jianbo Sun for their support. They provided me with the necessary support and companionship to help me get out of my current predicament and ultimately be able to complete my studies. They have provided me with valuable moral support throughout my life journey. I am very grateful to No Party For Cao Dong for giving me strength musically and letting me know that I am not useless.

I would like to thank my parents who supported me mentally and financially to enable me to achieve what I am today. I am also grateful that I can break out of my mental prison, and hope that I can start over in my future life and work.

Last, I am grateful to the IIR Research Fellow Project and Tsubeme Scholarship project for providing me with living expenses for my life in Japan.